

3.4 Cooperative Phenomena in Complex Macroscopic Systems

Tensor Network Study of Frustrated Quantum Spin Systems*

Naoki KAWASHIMA

Institute for Solid State Physics,

The University of Tokyo, Kashiwa-no-ha, Kashiwa, Chiba 277-8581

Tensor network states (TNS) are quantum wave function whose matrix elements are represented by partially contracted tensor products of many tensors. They are used as variational ansatz and turned out to be useful. The resulting optimized wave function is very accurate when the entanglement is not very strong. Even when it is strong, as is the case with the state near the quantum criticality, it still is competitive with other conventional numerical methods. One of the advantages of the tensor network method is that it is free from the negative sign problem inherent to the quantum Monte Carlo simulation. As a result, it may be possible, at least in principle, to compute frustrated quantum spin systems or fermionic systems within computation time that depends on the system size only polynomially. In our project using the ISSP supercomputer, we planned to (i) optimize and parallelize the tensor network based renormalization group (RG) method, and (ii) carry out computation on the kagome lattice antiferromagnet and related models.

As for the optimization and development of the RG method based on the TNS representation, we examined the simplest framework, i.e., the tensor RG proposed by Levin and Nave [1]. While this

framework is generally taken as the $O(D^6)$ method for the square lattice, we discovered that, by introducing the partial singular value decomposition (SVD), we can squeeze it down to $O(D^5)$ keeping the result unchanged. Our benchmark calculation showed the expected scaling up to the parallelization with 10,000 cores.

We also carried out tensor network computation based on the corner transfer matrix framework for kagome antiferromagnet and generalized Kitaev-Heisenberg model. As for the kagome antiferromagnet, we obtained very small or vanishing gap at zero field, consistent with the spin liquid nature of the ground state, and identified the nature of the $1/3$ magnetization plateau. As for the generalized Kitaev-Heisenberg model, we clarified the phase diagram that is supposed to represent Na_2IrO_3 . [2]

References

[*] This work has been done in collaboration with T. Okubo and S. Morita

[1] Michael Levin, Cody P. Nave: Phys. Rev. Lett. 99, 120601 (2007).

[2] Tsuyoshi Okubo, Kazuya Shinjo, Youhei Yamaji, Naoki Kawashima, Shigetoshi Sota, Takami Tohyama, and Masatoshi Imada: arXiv:1611.03614.

Nonuniqueness of local stress tensor of multibody potentials in molecular simulations

Koh M. NAKAGAWA and Hiroshi NOGUCHI

Institute for Solid State Physics, University of Tokyo, Kashiwa, Chiba 277-8581

Microscopic stress fields are widely used in molecular simulations to connect discrete molecular systems and continuum mechanics. The calculation method of local stress for pairwise potentials are well established but that for multibody potentials are still under debate. Recently, decomposition methods of multibody forces to central force pairs between the interacting particles have been proposed (called central force decomposition, CFD) [see Fig. 1(b)] [1, 2]. Their method satisfies the local conservation of translational and angular momentum and yields symmetry stress tensor $\sigma_{\alpha,\beta} = \sigma_{\beta,\alpha}$.

We introduced a force center of a three-body potential and proposed two alternative force decompositions that also satisfy the conservation of translational and angular momentum [3]. For three-body forces, three lines drawn along the force vectors \mathbf{f}_i from the particle positions \mathbf{r}_i ($i \in 1, 2, 3$) always meet at one position owing to the angular-momentum conservation. We call this position the force center, \mathbf{r}_c . Then the three-body forces are decomposed to three central force pairs between the particle positions and the force center (called force center decomposition, FCD) [see Fig. 1(c)]. By combining CFD and FCD, the force center is set at arbitrary positions (called hybrid decomposition, HD) [see Fig. 1(d)]. For four-body or more-body potentials, the forces can be decomposed by HD.

We compared the force decomposition by stress-distribution magnitude and discuss their difference in the stress profile of a bilayer membrane using coarse-grained (dissipative particle dynamics) and atomistic molecular dynamics simulations. For the atomistic model, DOPC lipids was simulated using CHARMM36 force

field and GROMACS 5.1. The lateral stress profile across the lipid bilayers is strongly dependent on the choice of the decomposition methods while the normal stress is constant and independent of the decompositions.

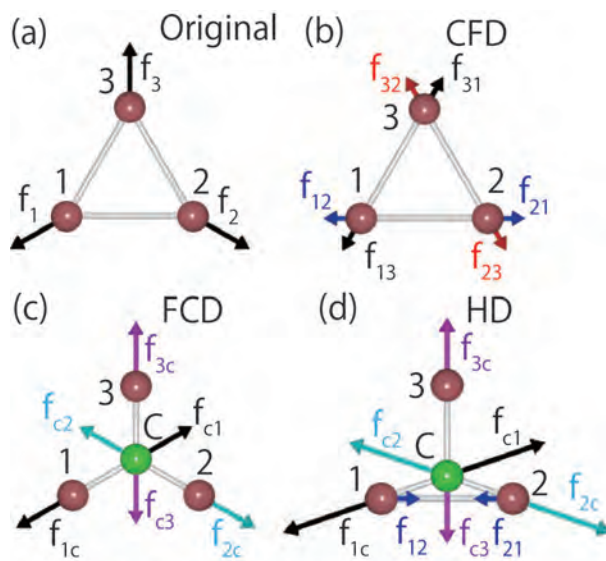


Figure 1: Force decomposition for area expansion forces. (a) Original forces. (b) CFD. (c) FCD. (d) HD. The green gray sphere represents the force center, \mathbf{r}_c .

References

- [1] N. C. Admal and E. B. Tadmor, *J. Elast.* **100**, 63 (2010).
- [2] J. M. Vanegas, A. Torres-Sánchez, and M. Arroyo, *J. Chem. Theory Comput.* **10**, 691 (2014).
- [3] K. M. Nakagawa and H. Noguchi: *Phys. Rev. E* **94**, 053304 (2016).

Morphology of high-genus fluid vesicles

Hiroshi NOGUCHI

Institute for Solid State Physics, University of Tokyo, Kashiwa, Chiba 277-8581

The nucleus of a eukaryotic cell is surrounded by a nuclear envelope. The nuclear envelope consists of two bilayer membranes connected by many lipidic pores, which are supported by a protein complex called nuclear pore complex (NPC). Nuclear pores have an approximately uniform distribution in the nuclear envelope. Hence, the nuclear envelope is a spherical stomatocyte with a high genus. In order to clarify the formation mechanism of the nuclear envelope, we simulated the morphology of high-genus vesicles by dynamically triangulated membrane methods.

First, we investigated the vesicle morphology of genus $0 \leq g \leq 8$ in the absence of NPCs [see Fig. 1(a)–(f)] [1]. For $g \geq 3$, bending-energy minimization without volume or other constraints produces a circular-cage stomatocyte, where the pores are aligned in a circular line on an oblate bud [see Fig. 1(a)]. As osmotic pressure is imposed to reduce the vesicle (perinuclear) volume, the vesicle transforms to the spherical stomatocyte (nuclear envelope shape) [see Fig. 1(d)]. In the lipid vesicles, the area difference ΔA of two monolayers of the bilayer is different from the preferred value ΔA_0 determined by the lipid number of both monolayers. This effect is taken into account by the area-difference elasticity (ADE) energy: $K_{\text{ade}}(\Delta A - \Delta A_0)^2/2$. With increasing ΔA_0 , the vesicle transforms from the circular-cage stomatocyte into discocyte continuously via pore opening [see Fig. 1(b)] at the large volume as seen in genus-0 vesicles. Surprisingly, however, at the small volume, the vesicle exhibits a discrete transition from polyhedron to discocyte [see Figs. 1(e) and (f)].

Next, we modeled the pore size constraint by the NPC as a ring which the membrane cannot penetrate [2]. When the pore is restricted as a small size, the aligned pores move to the

end of the vesicle under the bending-energy minimization as shown in Fig. 1(g). Interestingly, the pore-constraint itself rather presents the formation of the spherical stomatocyte. We found that the spherical stomatocyte is formed by a small perinuclear volume, osmotic pressure within nucleoplasm, and/or repulsion between the pores. When the ADE energy is accounted, the endoplasmic-reticulum-like tubules can grow from the spherical stomatocyte [see Fig. 1(i)].

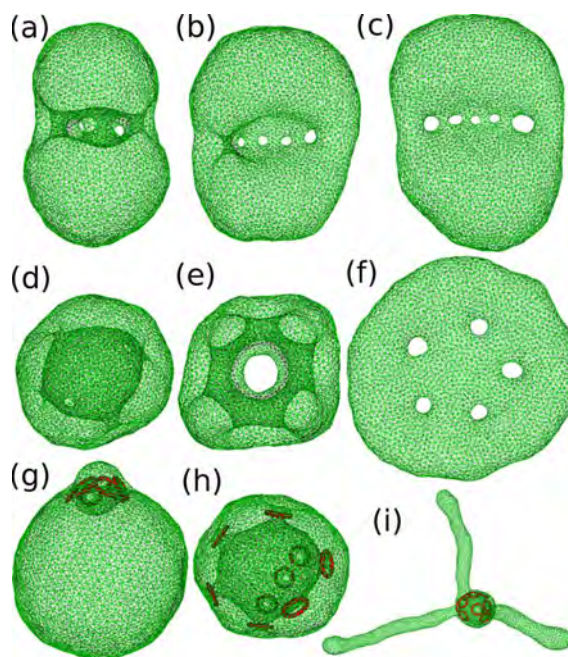


Figure 1: Snapshots of high-genus vesicles (a–f) with no pore-size constraint and (g–h) with pore-size constraint. (a–g) $g = 5$. (h,i) $g = 8$.

References

- [1] H. Noguchi: EPL **112**, 58004 (2015).
- [2] H. Noguchi: Biophys. J. **111**, 824 (2016).

Thermal properties of spin-S Heisenberg-Kitaev models on a honeycomb lattice

Takafumi SUZUKI

Graduate School of Engineering,

University of Hyogo, Shosha, Himeji, Hyogo 670-0083

In this project, we have studied thermal properties of spin-S Heisenberg-Kitaev (HK) models on a honeycomb lattice. It has been shown for the $S=1/2$ case that a spin liquid state, namely Kitaev's spin liquid (KSL), is stabilized when the Heisenberg interaction is weak enough [1]. The low-energy excitations of this KSL are characterized by Majorana fermions resulting from fractionalization of quantum spins. In the Kitaev model, where the Heisenberg interaction is absent, this fractionalization is observed as a two-peak structure in the temperature dependence of the specific heat $C(T)$ [2]. We reported that the two-peak structure of $C(T)$ survives in the magnetic ordered phase, if the system is located in the vicinity of the KSL phase, and this offers criteria for measuring the closeness to the KSL phase [3]. Similarly, it has been indicated that $C(T)$ of the HK model in the large S limit (HK model written by classical spins) also shows a two-peak structure [4].

In this study, we have calculated $C(T)$ for spin-S HK models and found that the origin of two peaks is quite different between the quantum and classical limits. The difference is evident in the higher temperature peaks in $C(T)$. For the quantum spin $S=1/2$, the higher

temperature peak is well developed. As the spin S increases, the high temperature peak shrinks and the prominent two-peak structure disappears for $3/2 < S$. In the classical limit, the high temperature peak remains as a shoulder structure. In order to discuss the details of the spin-S dependence for $C(T)$, we have applied the Jordan-Wigner transformation to the spin-S Kitaev model. The obtained results show that the model can be composed by kinetic terms of itinerant Majorana fermions and coupling terms of local gauge field with the itinerant Majorana fermions. The difference from the $S=1/2$ case is the number of colors for Majorana fermions. As S increases, the number of interactions between different-colored fermions increases. This can suppress the development of the higher temperature peak in $C(T)$.

References

- [1] A. Kitaev, *Ann. Phys.* **321**, 2 (2006).
- [2] J. Nasu, M. Udagawa and Y. Motome, *Phys. Rev Lett.* **113**, 197205 (2014).
- [3] Y. Yamaji, et al., *Phys. Rev B* **93**, 174425 (2016).
- [4] C. Price and N. Perkins, *Phys. Rev Lett.* **109**, 187201 (2012).

Multiscale Simulation of Polymer Melts

Takahiro MURASHIMA

Department of Physics,

Tohoku University, Aoba-Ward, Sendai, Miyagi 980-8578

We have been developing a multiscale simulation method to solve flow dynamics of entangled polymer melt [1]. This simulation consists of macroscopic fluid particle simulation and microscopic polymer dynamics simulation. Each fluid element at the macroscopic simulation has a microscopic simulator describing the internal degrees of freedom of the fluid element. The momentum and energy transfers among the fluid elements are considered through the macroscopic fluid dynamics simulation. Therefore, massively parallel computing are available for updating the microscopic degrees of freedom.

This year, the macroscopic simulation part are updated. In order to treat a large number of fluid elements, the macroscopic fluid simulation part must be parallelized. Using

FDPS [2], the parallelization of macroscopic fluid particle simulation part is succeeded in a short period of time. The code has been tested on system-B and system-C at ISSP, and then the production run has been done on K Computer. We have obtained a good parallel efficiency for the multiscale simulation. The details are summarized in Ref. [3].

References

- [1] T. Murashima, T. Taniguchi: EPL **96** (2011) 18002.
- [2] M. Iwasawa et al.: Publ. Astron. Soc. Jpn. **68** (2016) 54.
- [2] T. Murashima: Microsyst. Technol. (2017).
Doi:10.1007/s00542-017-3414-x.

Development of a parallel quantum Monte Carlo Method and Study of novel quantum phenomena in quantum lattice models

Akiko Masaki-Kato

Riken, Hirosawa, Wako, Saitama, 351-0198

We have developed parallelizable quantum Monte Carlo algorithm with nonlocal update[1] based on worldline algorithm and have studied quantum spin and lattice boson systems using massive parallel computer simulations.

This year, we especially focused on development of finite size scaling form for the parallelizable multi-worm algorithm (PMWA) what we proposed in Ref. [1]. In PMWA, a term corresponding to the transverse magnetic field is artificially introduced in the target Hamiltonian as the source field Γ of worms, and finally Γ is extrapolated to 0 limit after finishing the simulation. Unfortunately extrapolation rules are nontrivial and have to be considered about each case. In addition, there is a problem when we try to apply PMWA to critical phenomena because the correlation length is cut off by worms which are discontinuities of worldlines. In the critical region, the correlation length grows rapidly as it is close to the critical point. Consequently, usual FSS for critical phenomena does not work. We firstly solved this problem in the off-critical region by inventing a form of scaling

formula based on the idea of finite size scaling (FSS) derived from renormalization group theory instead of the extrapolation process. Secondly, in the critical region, we found FSS formula that can be used in PMWA by incorporating Γ as a scaling field (e.g. Γ works as a relevant field when the transition in case of XY universality, while treating Γ as irrelevant field in the case of Ising universality). I demonstrated to apply this finite worm+size scaling having two variables, Γ and T , to the finite temperature transition of superfluid using the Bayesian scaling tool [2]. The accuracy becomes higher than conventional worm algorithm when we use large system sizes with nontrivial parallelization.[3]

References

- [1] A. Masaki-Kato et al., *Phys. Rev. Lett.* **112**, 140603 (2014).
- [2] Kenji Harada, *Phys. Rev. E* **92**, 012106 (2015).
- [3] A. Masaki-Kato and N. Kawashima, unpublished.

The effect of bond-randomness on the quantum magnetisms in low dimension

Tokuro SHIMOKAWA and Hikaru KAWAMURA

Faculty of Science, Osaka University Machikane-yama, Toyonaka Osaka 560-0043

$S=1/2$ antiferromagnetic Heisenberg model on the kagome lattice with nearest-neighbor interaction are well known as a candidate of the possible realization of a quantum spin liquid (QSL) state. In spite of the tremendous efforts, the true natures still remain unclear.

In this study, we investigated the thermal properties of the $S=1/2$ kagome antiferromagnet by means of Hams-de Raedt (thermal pure quantum state) method [1-3]. This method enables us to compute exact finite-temperature physical quantities for larger lattice sizes (up to about 40 spins) than those treated by the conventional exact diagonalization method and the negative sign problem does not occur.

We identified the additional 3rd and 4th peaks in the low-temperature specific heat and found that the 3rd peak is associated with a crossover phenomenon occurring between the QSL states with distinct magnetic short-ranged orders (SROs). The static spin structure showed that

the low-temperature state is associated with $q=0$ SRO, while the high-temperature one with the $\sqrt{3} \times \sqrt{3}$ SRO[4].

Our specific heat we obtained here seems to be not comparable to the recent experimental results in herbertsmithite. This fact may imply that some additional ingredients such as bond-randomness [5] or a symmetry reduction [6] are needed.

Our numerical calculations have been performed by using CPU and FAT nodes of system B. The parallel computing technique with OpenMP has been employed.

References

- [1] M. Imada and M. Takahashi, J. Phys. Soc. Jpn. **55**, 3354 (1986).
- [2] A. Hams and H. De Raedt, Phys. Rev. E **62**, 4365 (2000).
- [3] S. Sugiura and A. Shimizu, Phys. Rev. Lett. **111**, 010401 (2013).
- [4] T. S and H. Kawamura, J. Phys. Soc. Jpn. **85**, 113702 (2016).
- [5] T. S., *et al*, Phys. Rev. B **92**, 134407 (2015).
- [6] A. Zorko, *et al*, Phys. Rev. Lett. **118**, 012720 (2017).

Critical behavior of the classical Heisenberg antiferromagnet on the stacked-triangular lattice

Hikaru Kawamura, and Yoshihiro Nagano

Graduate School of Science, Osaka University, Toyonaka 560-0043

The notion of universality is now standard in statistical physics of phase transition. Namely, it has been well established that critical behaviors of various continuous transitions can be classified into small number of universality classes determined by the basic properties of the system such as the spatial dimensionality and the symmetry of the system. In standard bulk magnets in three dimensions (3D), the number of spin components n dictates the underlying symmetry of the system, i.e., $O(n)$ symmetry, where $n=1,2,3$ correspond to the Ising, XY and Heisenberg universality classes.

It was suggested by one of the present authors in as early as mid-80's that there might exist new universality classes different from the standard $O(n)$ classes in certain frustrated magnets, i.e., $O(n) \times O(2)$ *chiral universality classes* [1,2]. While this theoretical proposal was met by the supports from some experiments [3], numerical simulations [4-6] and analytical calculations including the renormalization-group (RG) calculations [7] and the conformal bootstrap method [8], a counter view that the transition might actually be weakly first order has also been presented

[9,10], and the situation still remains not entirely clear.

In this year's project, we undertake a new set of large-scale Monte Carlo simulations on the antiferromagnetic classical Heisenberg on the 3D stacked-triangular lattice, a typical model expected to belong to the $n=3$ chiral universality class. We can go over to lattice sizes much larger than the previous works on the same model, i.e., up to 384^3 versus $60^3 \sim 90^3$.

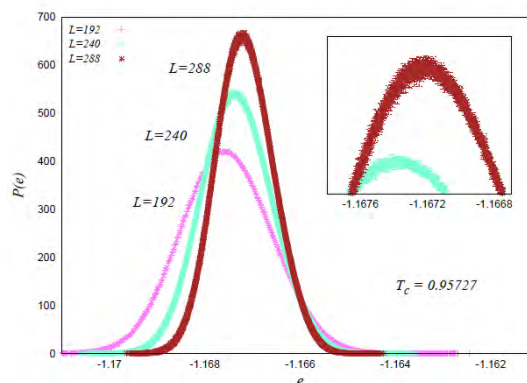


Fig1: The energy histogram at the transition point $T_c=0.95727$ for the sizes $L=192, 240$ and 288 .

In Fig.1, we show the energy distribution function at the transition temperature estimated to be $T_c=0.95727$, which persists to exhibit a single-peak structure characteristic of a continuous transition. Double-peak structure characteristic of a first-order transition has

never been observed, in sharp contrast to the previous work on the same model for smaller sizes [9]. Thus, we conclude that the transition is continuous.

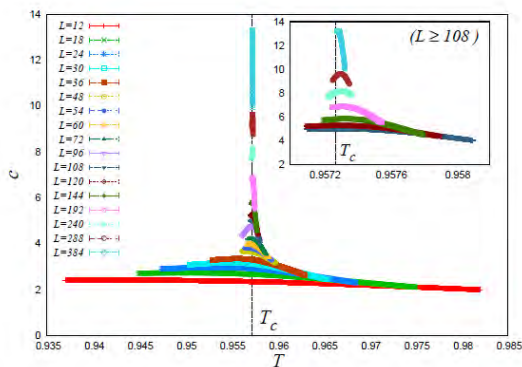


Fig.2: The temperature and size dependence of the specific heat.

In Fig.2, we show the temperature and size dependence of the specific heat. A sharp peak characteristic of a phase transition is observed. In fact, the analysis of the dimensionless quantities such as the correlation-length ratio has revealed the existence of a rather large correction to leading scaling in this model, described by a small correction-to-scaling exponent ω . Indeed, we find that the two correction-to-scaling exponents ω_1 and ω_2 provide satisfactory fits to all the data taken by our simulations, with $\omega_1=0.02$ and $\omega_2=0.05$.

Then, other spin exponents are estimated to be $\alpha=0.35(1)$, $\beta=0.29(6)$, $\gamma=1.1(1)$, $\nu=0.551(4)$, $\eta=0.07(23)$ whereas the chirality exponents to be $\beta_\kappa=0.37(3)$, $\gamma_\kappa=0.91(6)$ and $\eta_\kappa=0.35(10)$. Among various previous estimates claiming a continuous transition, our presents estimates are

best compared with the 6th order massive RG calculation by A. Pelissetto et al. [7], $\alpha=0.35(9)$, $\beta=0.30(2)$, $\gamma=1.06(5)$, $\nu=0.55(3)$, $\eta=0.073(94)$ whereas the chirality exponents to be $\beta_\kappa=0.38(10)$, $\gamma_\kappa=0.89(10)$ and $\eta_\kappa=0.38(20)$. Our new computation then strongly supports the view that the stacked-triangular-lattice Heisenberg antiferromagnet lies in the new $O(3) \times O(2)$ chiral universality class.

- [1] H. Kawamura, J.Phys.: Condens. Matter **10** (1998) 4707.
- [2] H. Kawamura, J.Phys.Soc.Japan **54** (1985) 3220; **61** (1992) 1299.
- [3] D. Beckmann, J. Wosnitza, H. v. Lohneysen, and D.Visser, Phys. Rev. Lett **71** (1993) 2829.
- [4] T. Bhattacharya, A. Billoire, R. Lacaze and Th.Jolicœur, J.Physique I **4** (1994) 181.
- [5] A. Mailhot, M.L. Plumer and A. Caille, Phys. Rev. B **50** (1994) 6854.
- [6] D. Loison and H.T. Diep, Phys. Rev. B **50** (1994) 16453.
- [7] A. Pelissetto, P.Rossi, and E.Vicari, Phys. Rev. B **63** (2001) 140414.
- [8] Y. Nakayama, and T. Ohtsuki, Phys. Rev. D **91** (2015) 021901.
- [9] V.Thanh Ngo, and H.T. Diep, Phys. Rev. E **78** (2008) 031119.
- [10] M. Tissier, B. Delamotte, and D. Mouhanna, Phys. Rev. Lett. **84** (2000) 520.

Seismic properties of the inhomogeneous one-dimensional Burridge-Knopoff model mimicking the subduction zone

Hikaru Kawamura and Maho Yamamoto

Graduate School of Science, Osaka University, Toyonaka, Osaka 560-0043

An earthquake is a stick-slip dynamical instability of a pre-existing fault driven by the motion of a tectonic plate. Numerical simulations of earthquakes based on a simplified statistical model, the so-called Burridge-Knopoff (BK) model, has been popular in statistical physics and provided much information about statistical properties of earthquakes. Some of the properties of the BK model was reviewed in Ref.[1].

In recent years, on the basis of the BK model combined with the rate-and-state dependent friction (RSF) law now standard in seismology, our group has studied slow-slip phenomena, including afterslips and silent (slow) earthquakes where the sliding velocity is several orders of magnitude smaller than that of the high-speed rupture of main shocks. Indeed, the simple BK model combined with the RSF law has turned out to be capable of describing rich seismic phenomena including such slow slips within a single unified framework, only with a few fundamental frictional and elastic parameters, the relative magnitude of the frictional parameters a and b appearing in the RSF law, in particular. When the velocity-strengthening parameter a is comparable or

moderately greater than the frictional weakening parameter b , main shocks accompany slow afterslips, while, when a is considerably greater than b , silent earthquakes occur without any high-speed rupture.

In the subduction zone, it has been known that the high-speed rupture of main shocks occurs in the shallower part while aseismic slips dominate in the deeper part, slow slips occurring in between. Such inhomogeneous occurrence is likely to be caused by the spatial change of the frictional parameter a/b . In this year's project, we studied the seismic properties of the inhomogeneous 1D BK model where the frictional parameters a/b are set non-uniform, i.e., $a \gg b$ in the deeper part but $a \ll b$ in the shallower part. We find that, in certain parameter range, main shocks in the shallower part are almost always preceded by slow slips in the deeper part. This observation gives some hope of the possible forecast of earthquakes by monitoring slow slips in the deeper region.

References

- [1] For review, see, H. Kawamura, T. Hatano, N. Kato, S. Biswas and B.K. Chakrabarti, *Rev. Mod. Phys.* 84, 839-884 (2012).

Numerical Diagonalization Study on the Quantum Spin Liquid in Frustrated System

Tôru SAKAI^{1,2,3}, Hiroki NAKANO^{1,2}, Tokuro SHIMOKAWA⁴, and Alisa Shimada⁵

¹*Graduate School of Material Science, University of Hyogo,
Kouto, Kamigori, Hyogo 678-1297, Japan*

²*Research Center for New Functional Materials, University of Hyogo,
Kouto, Kamigori, Hyogo 678-1297, Japan*

³*Synchrotron Radiation Research Center, Kansai Photon Science Institute,
Quantum Beam Science Research Directorate,*

*National Institute for Quantum and Radiological Science and Technology (QST)
SPring-8, Kouto, Sayo, Hyogo 679-5148, Japan*

⁴*Okinawa Institute of Science and Technology Graduate University, Okinawa 904-0495, Japan*

⁵*Graduate School of Science, Kyoto University, Kyoto 606-8502, Japan*

The $S=1/2$ kagome-lattice antiferromagnet is one of interesting frustrated quantum spin systems. The systems exhibit the quantum spin liquid behavior, which was proposed as an origin of the high- T_c superconductivity. The spin gap is an important physical quantity to characterize the spin liquid behavior. Whether the $S=1/2$ kagome-lattice antiferromagnet is gapless or has a finite spin gap, is still unsolved issue. Because any recently developed numerical calculation methods are not enough to determine it in the thermodynamic limit. Our large-scale numerical diagonalization up to 42-spin clusters and a finite-size scaling analysis indicated that the $S=1/2$ kagome-lattice antiferromagnet is gapless in the thermodynamic limit[1]. It is consistent with the $U(1)$ Dirac spin liquid theory of the kagome-lattice antiferromagnet[2, 3]. On the other hand, some density matrix renormalization group (DMRG) calculations supported the gapped Z_2 topological spin liquid theory[4, 5]. Our recent numerical diagonalization analysis on the magnetization process of a distorted kagome-lattice antiferromagnet indicated that the perfect kagome-lattice system is just on a quan-

tum critical point[6]. It would be a possible reason why it is difficult to determine whether the perfect kagome-lattice antiferromagnet is gapless or gapped. The magnetization process will be also discussed[7, 8, 9].

References

- [1] H. Nakano and T. Sakai: J. Phys. Soc. Jpn., 2011, 80, 053704.
- [2] Y. Ran, M. Hermele, P. A. Lee and X. -G. Wen: Phys. Rev. Lett., 2007, 98, 117205.
- [3] Y. Iqbal, F. Becca, S. Sorella and D. Poilblanc: Phys. Rev. B, 2013, 87, 060405(R).
- [4] S. Yan, D. A. Huse and S. R. White: Science, 2011, 332, 1173.
- [5] S. Nishimoto, N. Shibata and C. Hotta: Nature Commun., 2013, 4, 2287.
- [6] H. Nakano and T. Sakai: J. Phys. Soc. Jpn., 2014, 83, 04710.
- [7] H. Nakano and T. Sakai: J. Phys. Soc. Jpn., 2015, 84, 063705.

- [8] T. Sakai and H. Nakano: Phys. Rev. B,
2011, 83, 100405(R).
- [9] T. Sakai and H. Nakano: POLYHEDRON
126 (2017) 42.

Novel Field Induced Transitions in Low-Dimensional Quantum Spin Systems

Tôru SAKAI^{1,2,3}, Hiroki NAKANO^{1,2}, Tokuro SHIMOKAWA⁴, and Alisa Shimada⁵

¹*Graduate School of Material Science, University of Hyogo,
Kouto, Kamigori, Hyogo 678-1297, Japan*

²*Research Center for New Functional Materials, University of Hyogo,
Kouto, Kamigori, Hyogo 678-1297, Japan*

³*Synchrotron Radiation Research Center, Kansai Photon Science Institute,
Quantum Beam Science Research Directorate,*

*National Institute for Quantum and Radiological Science and Technology (QST)
SPring-8, Kouto, Sayo, Hyogo 679-5148, Japan*

⁴*Okinawa Institute of Science and Technology Graduate University, Okinawa 904-0495, Japan*

⁵*Graduate School of Science, Kyoto University, Kyoto 606-8502, Japan*

The $S=1/2$ distorted diamond chain is one of interesting frustrated low-dimensional quantum spin systems. The candidate material azurite $\text{Cu}_3(\text{CO}_3)_2(\text{OH})_2$ was revealed to exhibit a field-induced spin gap at $1/3$ of the saturation magnetization in the high-field magnetization measurement[1]. In the present study we take the additional monomer-monomer interaction into account in the distorted diamond spin chain. The numerical exact diagonalization and the level spectroscopy analysis indicated that the monomer-monomer interaction makes the $1/3$ magnetization plateau appear in wider parameter regions[2].

Using the same analysis we also investigated the effect of the monomer-monomer interaction on the $S=1/2$ distorted diamond spin chain. The obtained ground state phase diagram is much more consistent with the experimental result of the azurite, rather than the previous phase diagram[3].

References

[1] H. Kikuchi, Y. Fujii, M. Chiba, S. Mitsudo, T. Idehara, T. Tonegawa, K.

Okamoto, T. Sakai, T. Kuwai and H. Ohta: Phys. Rev. Lett. 94 (2005) 227201.

[2] K. Okamoto, T. Tonegawa and T. Sakai: J. Phys. Soc. Jpn. (Letters) 85 (2016) 063704.

[3] K. Okamoto, T. Tonegawa, Y. Takahashi and M. Kaburagi: J. Phys.: Cond. Mat. 11 (1999) 10485.

Applicability of scaling law in the magnetic refrigeration

Ryo TAMURA

*International Center for Materials Nanoarchitectonics,
National Institute for Materials Science
1-1 Namiki, Tsukuba, Ibaraki, 305-0044*

Cooling phenomena are widely used in everyday, such as food storage and medical treatment, and also in technology for next-generation electronics, such as hydrogen-fuel cells and quantum information processing. Thus, high-performance cooling technology has been actively developed for many fields. The magnetic refrigeration is a promising candidate for a next-generation cooling technology[1, 2, 3, 4, 5], which can solve environmental and noise problems.

In magnetic materials, the change of magnetic entropy is induced by applying magnetic field. In the magnetic refrigeration, the magnetic entropy change at the phase transition point is mainly used. Because the magnetic entropy density in the magnetic materials is higher than that of gas refrigeration, it is possible that higher refrigeration efficiency is obtained by the magnetic refrigeration than the gas refrigeration. Then, searching for high-performance magnetic refrigeration materials which exhibit a large magnetic entropy change has been done exhaustively.

For the magnetic refrigeration materials where the second-order phase transition occurs, the magnetic entropy change ΔS_M can be predicted by using the scaling law which is given by

$$\Delta S_M \propto |H|^n, \quad (1)$$

where H is the magnetic field. Furthermore, n

is obtained by

$$n = 1 + \frac{\beta - 1}{\beta\delta}, \quad (2)$$

where β and δ are the critical exponents of each magnetic material. However, this scaling law is not guaranteed for larger magnetic fields. Thus, it is necessary to quantify the limits where the scaling laws would remain applicable for researches on magnetic refrigeration. For this purpose, we investigated the magnetic field dependence of the magnetic entropy of (a) a mean-field model with Curie temperatures ranging from 46 to 336 K, (b) experimental data for Gd, and (c) a 3D-Ising model which is beyond the mean-field approximation.

From the results, we found that the scaling law remains applicable up to the magnetic field which is obtained by $\mu_0 H_{\text{mag}} \times 8\%$ T. Here, H_{mag} is defined by $k_B T_c / gJ\mu_B$ where k_B, T_c, g, J , and μ_B are the Boltzmann constant, the Curie temperature, the g -factor, the magnetic quantum number, and the Bohr magneton, which are the characteristic values of each magnetic material. In this range, the predictions of magnetic entropy change by the scaling law remain within errors of 5 %, which is smaller than the experimental error margin. Thus, for magnetic refrigeration materials whose Curie temperature is close to room temperature, scaling laws at the Curie temperature would be applicable for the magnetic field range available at conventional laboratories, that is, smaller than 10 T[6]. From the

results, it was shown that the scaling law is sufficiently practical for development of the high performance magnetic refrigeration materials.

This work is the collaboration work with Carlos Romero-Muñiz (Universidad Autónoma de Madrid), Shu Tanaka (Waseda University), and Victorino Franco (Universidad de Sevilla).

References

- [1] A. M. Tishin and Y. I. Spichkin: *The Magnetocaloric Effect and its Applications* (Taylor & Francis, London, 2003).
- [2] K. A. Gschneidner and V. K. Pecharsky: *Annu. Rev. Mater. Sci.* **30** (2000) 387.
- [3] R. Tamura, T. Ohno, and H. Kitazawa: *Appl. Phys. Lett.* **104** (2014) 052415.
- [4] R. Tamura, S. Tanaka, T. Ohno, and H. Kitazawa: *J. Appl. Phys.* **116** (2014) 053908.
- [5] S. Toyozumi, H. Kitazawa, Y. Kawamura, H. Mamiya, N. Terada, R. Tamura, A. Dönni, K. Morita, and A. Tamaki: *J. Appl. Phys.* **117** (2015) 17D101.
- [6] C. Romero-Muñiz, R. Tamura, S. Tanaka, and V. Franco: *Phys. Rev. B* **94** (2016) 134401.

2D Scattering Pattern Analysis on Coarse Grained MD Model of Filled Hydrogel

Katsumi HAGITA

Department of Applied Physics,

National Defense Academy, 1-10-20, Hashirimizu, Yokosuka, Kanagawa 239-8686

Recently, small angle scattering experiments to observe 2D scattering patterns of filler filled polymer materials are widely performed. For systems with anisotropic axis, 2D scattering patterns analysis is a powerful tool to obtain information of nm-scale structures. When anisotropic axis is x , reasonable approximations of 2D scattering patterns $I(q_x, q_{\parallel})$ can be calculated by circular average $I(\mathbf{q})$ for q_y - q_z , where $q_{\parallel}^2 = q_y^2 + q_z^2$ and $I(\mathbf{q})$ is a square of 3d Fourier transformation of densities.

It is considered that coarse grained (cg) MD simulations with bead spring model based on Kremer-Grest model [1] are effective tools to simulate nm-structures in systems with sub-micron meter dimensions. Recently, we examined changes of 2D scattering patterns of spherical nanoparticles in rubbers by the cgMD with uniaxial elongation [2]. We considered the cgMD is effective for fillers in hydrogels.

Shibayama and co-workers had been reported 2D scattering patterns of clays in clay-filled hydrogels under uniaxial elongation [3,4]. We developed cgMD model for this system. In our model, a disc-like clay filler consists of 177 particles, polymer chains are modeled by

Kremer-Grest model, and explicit solvent are not considered. For simulations of hydrogels, density of polymers and fillers are much smaller than those for simulations of rubbers. During pseudo-reaction process, ends of polymer chains are bonded to other ends or particles of clays. After the pseudo-reaction, we elongated the PBC box with constant volume condition.

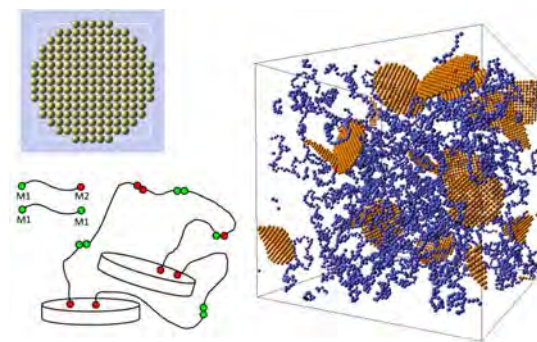


Fig. 1: Cartoon of cgMD model of clay-filled hydrogels.

We performed cgMD simulations for various densities of clays and polymers. We used LAMMPS package [5] as MD solver. Almost calculations planned in our D-class proposal are performed by using supercomputers under the JHPCN proposals in

FY2015 and 2016 in order to save computing resources for Solid State Physics.

Figure 2 shows one of results of our cgMD simulations. Here, clay-density dependence on stress-strain relation is in good agreement with those measured by tensile experiments. The obtained 2D scattering patterns are consistent with those reported by Shibayama group [3, 4]. As results, we confirmed relationship between structure and mechanical function. Detail calculations and analyses are in progress.

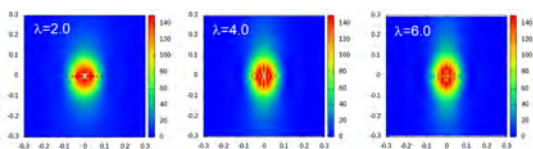


Fig. 2: 2D scattering patterns of clay-filled hydrogels by cgMD simulations of uniaxial elongation.

We also considered 2D scattering patterns of spherical nano-particles in hydrogels. In cgMD simulations, spherical aggregations of particles are used instead of disc-like clay. Examples of obtained 2D scattering patterns are presented in Fig. 3. In Fig. 3, system size dependence is examined. Here, number of fillers are 512, 4096, and 32768. We considered 4096 fillers are required to observe 2D scattering patterns. Detail calculations and analyses are in progress.

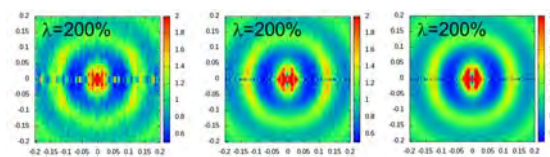


Fig. 3: Dependence of system size on 2D scattering patterns of spherical-filler filled hydrogels by cgMD simulations of uniaxial elongation.

In addition, 2D scattering pattern can be used as an indicator of nanovoids in filler-filled polymer nanocomposites. Recently, we had reported creation and growth of nanovoids in elongated rubbers [6]. In our preliminary calculations, peaks corresponding to nanovoids can be observed in 2D scattering patterns. Detail calculations and analyses are in progress.

References

- [1] K. Kremer, G. S. Grest: *J. Chem. Phys.* **92** (1990) 5057.
- [2] K. Hagita, H. Morita, M. Doi, H. Takano: *Macromolecules* **49** (2016) 1972-1983.
- [3] S. Miyazaki, T. Karino, H. Endo, K. Haraguchi, M. Shibayama: *Macromolecules* **39** (2006) 8112–8120.
- [4] T. Nishida, H. Endo, N. Osaka, H.-J. Li, K. Haraguchi, M. Shibayama: *Phys. Rev. E* **80** (2009) 030801.
- [5] S. Plimpton: *J. Comp. Phys.* **117** (1995) 1.
- [6] K. Hagita, H. Morita, H. Takano, *Polymer*, **99** (2016) 368-375.

Efficient Sampling Simulation of the Soft Modes Significantly Contribute to Protein Properties

Duy TRAN, Kazuhiro TAKEMURA, Hisham DOKAINISH, Jacob SWADLING,
Hiroaki HATA, Kenichiro TAKABA, Chika SATO, and Akio KITAO
Institute of Molecular and Cellular Biosciences, University of Tokyo

Here we report dissociation and association simulation of a protein-protein complex using Parallel Cascade Selection Molecular Dynamics (PaCS-MD¹).

Simulating dissociation and association processes of protein-protein complexes using classical molecular dynamics simulation remains highly challenging. Typically, biased forces are used to accelerate these processes. However, biased forces sometimes mislead protein complexes to unnatural metastable states. Moreover, changes in environments, e.g., ionic or electrostatic interactions lead to changes in the free energy landscape of the substrate². Therefore, unbiased and slow-growth simulation methods for association and dissociation might yield better structures of the protein-protein complexes. Here we present a method based on PaCS-MD for generating the dissociation and association pathways without using any biased forces. PaCS-MD conducts cycles of multiple short MD simulations in parallel, which allows us to explore local conformational states. Snapshots closest to target configurations are chosen as the inputs for the next cycle. Our flexible docking method based on PaCS-MD can take advantage of highly distributed computing.

We have applied our method to the complex of the transactivation domain of p53 (TAD-p53) protein and MDM2 protein. We simultaneously performed association and dissociation simulations using the

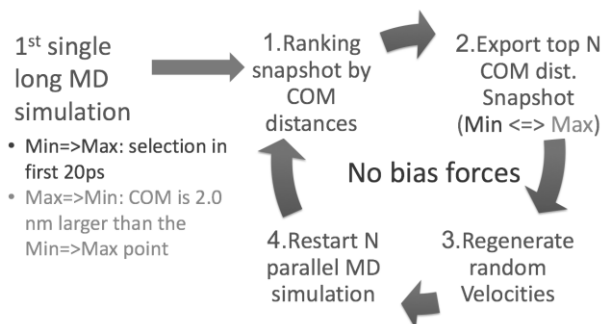


Fig 1. Workflow of flexible-body docking method based on PaCS-MD

center of mass distance (d) as a selection parameter to enhance the motion toward the bound structure of the TAD-p53/MDM2 (Fig. 1). We used the switching condition between dissociation and association and vice versa as follows: if association did not progress for 20 ps, association will switch to dissociation. When d reaches at the point 2.0 nm longer than the last switching point, association simulation will start. A time step of 1fs was used with velocity Verlet integration in all of our simulations together with the MTTK barostat³ and Nosé-Hoover thermostat^{4,5}.

After performing 274 cycles, we examined all the conformations of TAD-p53 and MDM2 if structures similar to the crystal complex structure were generated. Figure 2 shows the all-atom RMSD of TAD-p53 from the crystal structure (PDB id 1YCQ). The RMSD minimum that we achieved was 0.429 nm. Although not using the biased force, TAD-p53 found the correct binding cavity. We clustered all the bound conformation to check the variation of

the structures. We identified 4 representative structures among all the bound conformations as shown in Figure 3a. Figure 3b shows the lowest RMSD structure of TAD-p53. Although the two key π - π stacking interactions were not formed, their contacts are in agreement with the crystal structure. The binding interface RMSD of TAD-p53 between the best structure and the crystal structure is 0.243 nm.

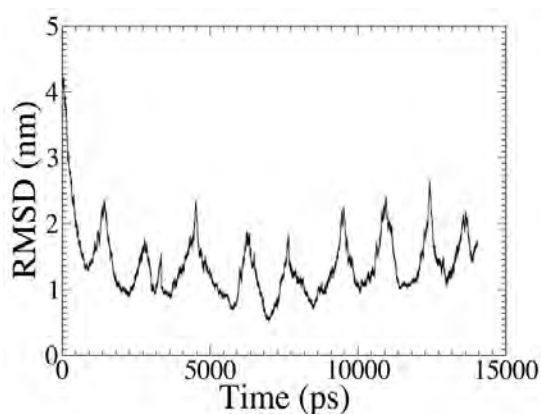


Fig 2. RMSD of TAD-p53 from the crystal structure in concatenated trajectory

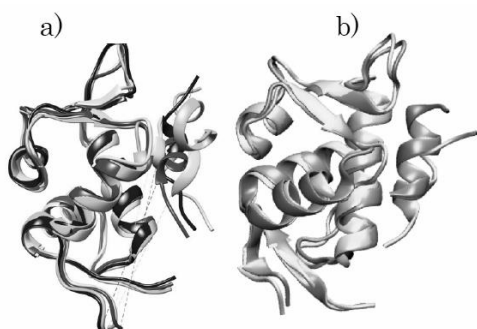


Fig 3. Conformations of the bound structure. a) Representative structure. b) Lowest RMSD structure of TAD-p53 after least square fitting of MDM2 to the x-ray structure

Next, we constructed the Markov State Model to predict the lowest binding free energy structure. We used the distance RMSD (dRMSD) of simulated TAD-p53 from the initial TAD-p53 of the simulation. We found that the lowest energy minimum is situated at dRMSD = 4.21 nm as

shown in Fig 4. Interestingly, among the structures at around dRMSD = 4.21 nm, we found that the lowest RMSD structure is identical to the one previously mentioned.

Our proposed method is a promising flexible-body docking method that considers solvation changes during association and flexibility of protein substrate. We would continue to develop our method to reduce the total simulation time needed to reach the structure in agreement with experiment.

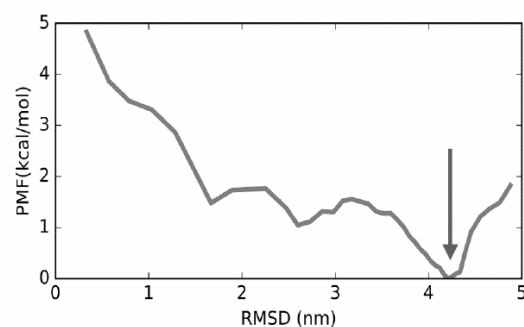


Fig 4. Evolution of PMF with distance RMSD of TAD-p53 after least square fitting with MDM2

References

- (1) Harada, R.; Kitao, A. Parallel Cascade Selection Molecular Dynamics (PaCS-MD) to Generate Conformational Transition Pathway. *J. Chem. Phys.* **2013**, *139* (3).
- (2) Kitao, A.; Takemura, K. High Anisotropy and Frustration: The Keys to Regulating Protein Function Efficiently in Crowded Environments. *Curr. Opin. Struct. Biol.* **2017**, *42*, 50–58.
- (3) Martyna, G. J.; Tuckerman, M. E.; Tobias, D. J.; Klein, M. L. Explicit Reversible Integrators for Extended Systems Dynamics. *Mol. Phys.* **1996**, *87* (5), 1117–1157.
- (4) Hoover, W. G. Canonical Dynamics: Equilibrium Phase-Space Distributions. *Phys. Rev. A* **1985**, *31* (3), 1695–1697.
- (5) Nosé, S. A Unified Formulation of the Constant Temperature Molecular Dynamics Methods. *J. Chem. Phys.* **1984**, *81* (1), 511–519.

Magnetization process modified by quantum phonons

Hidemaro SUWA

Department of Physics, The University of Tokyo
7-3-1 Hongo, Bunkyo, Tokyo 113-0033

Under magnetic field, magnetization shows a characteristic curve as a result of interaction. A magnetization curve offers great opportunity for finding the spin energy scale, gaped ground states with magnetization plateaus, magnon interaction, etc. By fitting to model calculation, spin interaction of a material can be well inferred.

Meanwhile, spin-phonon interaction can produce complicated effective spin interaction and non-trivial phenomena [1]. For example, CuGeO_3 , which is considered as a quasi one-dimensional spin system, has significant spin-phonon interaction because of the edge-sharing CuO_6 octahedra. Its magnetization process [2] with magnetic field shows the complex curve that is not fitted well by a simple spin model. For understanding the nature of the material, it is necessary to study a physical model that has phonon degrees of freedom explicitly.

We studied the magnetization curve of a one-dimensional spin-phonon model by using the worldline quantum Monte Carlo method without any approximation [3]. We found a non-trivial magnetization process that is significantly different from calculation of simple spin models and close to the experimental data. In addition, a new Monte Carlo technique was developed for energy-level and magnetization-curve calculation. We use the projector Monte Carlo approach, preparing various trial states with different quantum numbers. The energy level of each quantum number, e.g., total S^z , is precisely estimated tuning magnetic field in a plausible way. The whole magnetization curve is precisely calcu-

lated using this projector technique.

We also calculated the magnon interaction around saturation field. At a magnetic field stronger than the saturation field, the excitation of the spin chain is a magnon. While the magnon interaction of the Heisenberg chain is repulsive, it can be attractive, which leads to a nematic phase. The spin chain with a ferromagnetic J_1 and an antiferromagnetic J_2 interaction has indeed the nematic phase.

We calculated the energy level of several magnon states for the spin-phonon model and found that magnons can attractively interact with each other as a result of the quantum nature of phonons. Our result indicates the existence of the non-trivial nematic phase. Nevertheless, more careful study of the finite-size effect and the thermodynamic limit is needed for a future problem.

As for the computation, we used the system B as the class C (project ID:H28-Cb-0052). Independent worldline quantum Monte Carlo simulations with the worm (directed-loop) algorithm and the geometric optimization were efficiently run by the MPI parallelization.

References

- [1] H. Suwa *et al.*: Phys. Rev. Lett. 115 (2015) 080601.
- [2] H. Nojiri *et al.*: Phys. Rev. B 52 (1995) 12749.
- [3] H. Suwa: Springer Theses (2014).

Monte Carlo Spectral Analysis of Quantum Spin Systems with Emergent Excitation

Hidemaro SUWA

*Department of Physics, The University of Tokyo
7-3-1 Hongo, Bunkyo, Tokyo 113-0033*

Conventional quantum phase transitions between different ground states of quantum many-body systems can be understood within the Landau-Ginzburg-Wilson (LGW) paradigm, according to which a critical point is described by an order parameter whose fluctuation diverges. Following intriguing numerical results pointing to violations of LGW predictions, the deconfined quantum critical (DQC) point was proposed as a scenario beyond the standard paradigm. Here the low-energy physics is not described directly by order parameters, but by fractional degrees of freedom that emerge (deconfine) on long length scales close to the DQC point. These fractional objects should have prominent signatures in excitation spectra and experimentally accessible spectral functions.

The existence of the DQC point has been addressed in numerous studies of the J - Q model, 3D close-packed loop and dimer models (which provide effective descriptions of quantum spins), and lattice versions of the proposed non-compact CP^1 DQC field theory. Dynamical properties of DQC systems have not been addressed in direct numerical calculations. The J - Q model offers unique opportunities to study deconfined excitations and the quantum dynamics of confinement. The deconfined excitations should be spinons carrying spin $S = 1/2$.

We investigated the level spectrum of the J - Q model at its DQC point [1]. We analyzed gaps extracted from correlation functions, thus characterizing the level spectrum of spinons and scaling behaviors as bound states (magnons) form in the ordered phases. Our study reveals gapless critical $S = 0$ and $S = 1$ excitations at

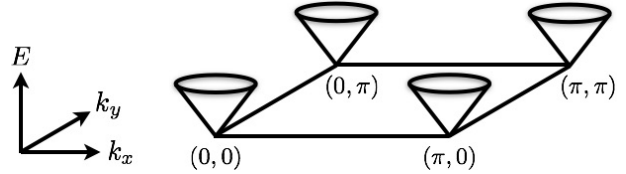


Figure 1: Schematic illustration of the low-lying energy spectrum at the deconfined quantum-critical point. There are four gapless points for both $S = 0$ and 1 excitations, at $\mathbf{k} = (0,0), (\pi,0), (0,\pi),$ and (π,π) . Close to these points the modes disperse linearly with the same velocity. The dispersion relation marks the lower edge of a continuum of excitations arising from two essentially deconfined spinons, with the single-spinon dispersion also being the same as the lower edge of the two-spinon continuum. This figure was taken from Ref. [1].

$\mathbf{k} = (0,0), (\pi,0), (0,\pi),$ and (π,π) , and all these points are characterized by linear dispersion with a common velocity, thus lending strong support to elementary $S = 1/2$ spinons with dispersion minimum at the above four \mathbf{k} -points. Moreover, the scaling of singlet and triplet gaps in the ordered phases exhibits a duality consistent with emergent $SO(5)$ symmetry.

As for the computation, we used the system B as the class C (project ID:H28-Ca-0099). Independent worldline quantum Monte Carlo simulations with the single loop update were efficiently run by the MPI parallelization.

References

- [1] H. Suwa, A. Sen, and A. W. Sandvik: Phys. Rev. B **94** (2016) 144416

Screening for Thermal Functional Materials using Materials Informatics

Junichiro SHIOMI

Department of Mechanical Engineering, The University of Tokyo

7-3-1 Hongo, Bunkyo, 113-8656

Informatics, as the fourth paradigm of science in addition to theory, simulation, and experiment, is gaining great attention in general and interdisciplinary fields of physics which is a powerful approach to search for optimal models, structures, and materials. This year, we focused on designing nanostructures for phonon transport via informatics. We have developed a new materials-informatics (MI) method combining atomistic Green's function approach and Bayesian optimization that realizes highly efficient design of nanostructures with optimal thermal transport, as shown in Fig. 1.

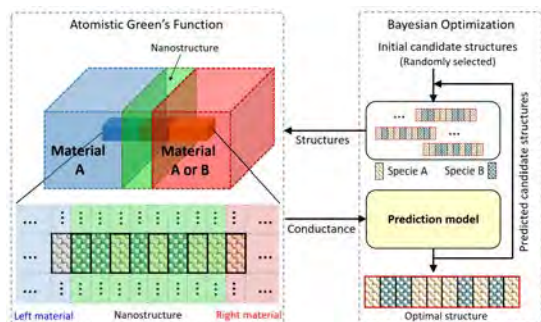


Figure 1: Schematics of the materials informatics method combining Atomistic Green's function (AGF) and Bayesian optimization.

As a case study, we have applied the developed method to design the Si/Ge-composite nanostructures that minimize or maximize interfacial thermal conductance (ITC) across Si-Si and Si-Ge interfaces

which are important and realistic for instance in thermoelectrics. We formulate two optimization problems: the first part is optimization of relatively small interfacial region accounting for full degrees of freedom (as shown in Fig. 2) to demonstrate the validity and capability of the current method, and the second part move on to the optimization of larger interfacial region with layered superlattice structures, which is possible to do experiment measurement.

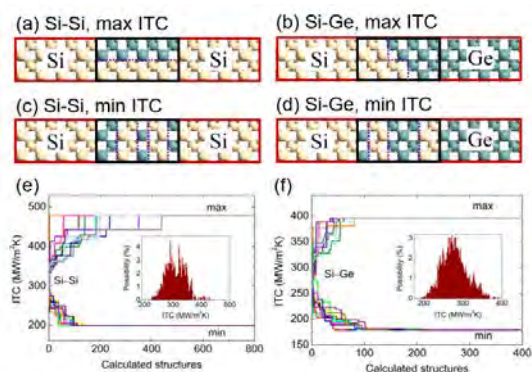


Figure 2: Interfacial Si/Ge alloy structure optimization. (a)-(d) Optimal structures with the maximum and minimum interfacial thermal conductance. (e), (f) The 10 optimization runs with different initial choices of candidates, where the insets show the probability distributions of ITC obtained from calculations of all the candidates.

The optimal structures were obtained by calculating only a few percent of the total candidate structures, considerably saving the computational resources. In addition, the obtained structures are non-intuitive and impacting. The validity and capability of the method are demonstrated by identifying the thin interfacial structures with the optimal Si/Ge configurations among all the possible candidates. Based on the finding that the interfacial structures with minimum ITC take a form of aperiodic superlattice, we extended the search to thicker structures (up to 8.69 nm), and identified non-intuitive structures whose ITCs are significantly smaller than those of the optimal periodic superlattices.

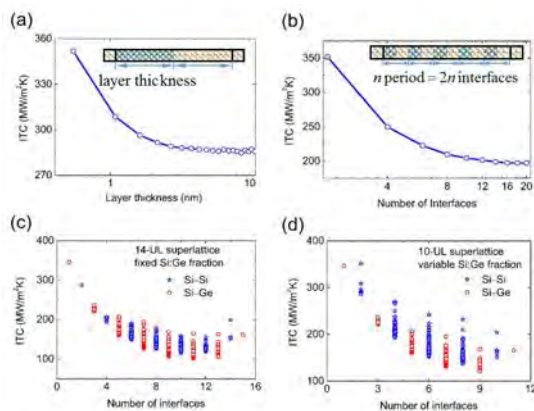


Figure 3: (a), (b) Interfacial thermal conductance versus the layer thickness and number of interfaces. (c), (d) Interfacial thermal conductance versus number of interfaces for cases of 14-unit layer (UL) superlattice with equal Si/Ge layer number and 10-UL superlattice with variable Si/Ge fraction.

Another merit of MI lies in possibility to explore new physics in the course of

understanding its output. By performing further systematic analyses, we identified that the small thermal conductance in the aperiodic superlattices originates from their degrees of freedom to mutual-adoptively balance the two competing effects (as shown in Fig. 3): as the layer thickness in superlattice increases, the impact of Fabry–Pérot interference increases, and the rate of reflection at the layer-interfaces decreases. Aperiodic superlattice with spatial variation in the layer thickness has a degree of freedom to realize optimal balance between the above two competing mechanism. Furthermore, the spatial variation enables weakening the impact of constructive phonon interference in relative to that of destructive interference.

In conclusion, we have developed a framework combining atomistic Green's function and Bayesian optimization to design the nanostructure for phonon transport with high efficiency. The present work shows the effectiveness and advantage of material informatics in designing nanostructures to control heat conduction. We believe that the developed novel method, which can be applied to nanostructure design of any materials in principle, would have a broad and impacting appeal to the general scientific and engineering communities, as well as to the general public.

References

S. Ju, T. Shiga, L. Feng, Z. Hou, K. Tsuda, J. Shiomi: Physical Review X, in press (arXiv:1609.04972).

Control of phonon and electron transport properties using mechanical strain

Junichiro SHIOMI

Department of Mechanical Engineering, University of Tokyo,

Hongo 7-3-1, Bunkyo-ku, Tokyo 113-8656

Carbon nanotubes (CNTs) have recently attracted attention as materials for flexible thermoelectric devices. To provide theoretical guideline of how defects influence the thermoelectric performance of CNTs, we have theoretically studied the effects of defects (vacancies and Stone-Wales defects as shown in Fig. 1) on its thermoelectric properties; thermal conductance, electrical conductance, and Seebeck coefficient.

We used a nonequilibrium molecular dynamics simulation and Green's function method to obtain thermal and electrical properties, respectively. We revealed that the defects mostly strongly suppress the electron conductance, and deteriorate the thermoelectric performance of a CNT. By plugging in the results for single CNTs and the intertube-junction properties into the network model, we further show that the figure of merit (ZT) increases with decreasing the CNT length regardless of the presence of defects (Fig. 2(a)) and that the defects with realistic concentrations can significantly degrade the thermoelectric performance of CNT-based networks (Fig. 2(b)). Our findings indicate the importance of the improvement of crystallinity of CNTs for improving CNT-based thermoelectrics.

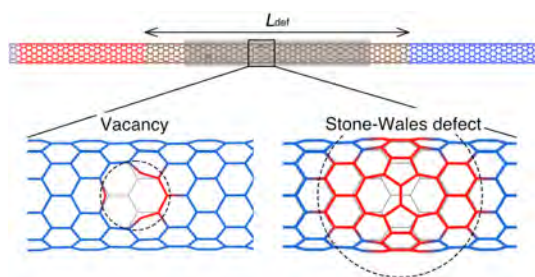


Fig. 1: Analysis model for CNTs with vacancies and Stone-Wales defects.

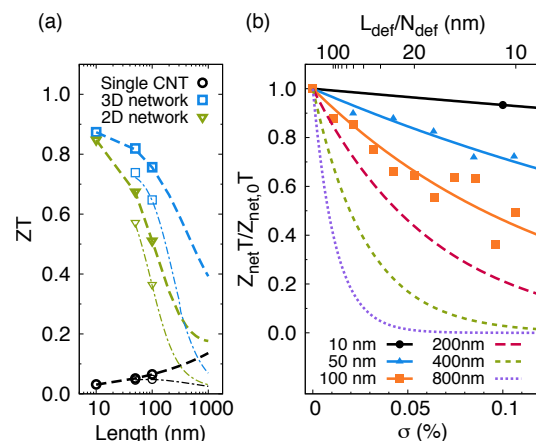


Fig. 2: Figure of merit (ZT) of CNT networks. Dependence of (a) the CNT length and (b) defect concentration.

References

- [1] M. Ohnishi, T. Shiga, and J. Shiomi: *Phys. Rev. B* **95**, 155405 (2017).

Numerical study on low-energy states of quantum spin systems

Hiroki NAKANO

*Graduate School of Material Science, University of Hyogo
3-2-1 Kouto, Kamigori-cho, Ako-gun, Hyogo 678-1297, Japan*

Numerical approaches become more and more important in condensed matter physics because it is generally difficult to estimate physical quantities precisely in systems of many-body problems. From such a motivation, a lot of computational studies have been carried out and contributed much to our deeper understanding of such quantum systems. However, numerical studies are particularly difficult when quantum spin systems in spatial dimensions larger than one include frustrations. The reason for this difficulty comes from the situation that effectively applicable algorithms are limited. It is well known that such systems cannot be treated by the density matrix renormalization group calculations and the quantum Monte Carlo simulations. Only the numerical diagonalization method based on the Lanczos algorithm is generally applicable for such frustrated quantum spin systems in dimensions larger than one. This method also has a weak point at the same time. This method can treat only very small system sizes. To overcome this disadvantage, we succeeded in developing a hybrid-type parallelized code of Lanczos diagonalization[1]. We examine quantum spin systems using this Lanczos-diagonalization code that we developed as a primary approach.

The primary study of this year in the present project examines the ground state of the $S = 1/2$ Heisenberg antiferromagnet on the triangular lattice with a distortion[2]. The distortion is controlled between the undistorted triangular lattice and the dice lattice[3]. The dice-lattice antiferromagnet does not include frustrations in it; this lattice satisfies the Lieb-Mattis theorem[4]. Therefore, the ground state

of the Heisenberg antiferromagnet on the dice lattice shows ferrimagnetism with the spontaneous magnetization whose magnitude is one third height of the saturation. In the undistorted triangular lattice, on the other hand, it is widely believed that the ground state shows 120-degree spin structure, which does not show a nonzero spontaneous magnetization. We examine the intermediate region between the two limiting cases by the numerical-diagonalization method. Our diagonalization results suggest that the ground state in an intermediate region between the two limiting cases shows spontaneous magnetizations. The magnitude gradually increases as the distortion is controlled from the undistorted case to the case when there appears the ferrimagnetic state based on the Lieb-Mattis theorem. A similar intermediate state with nonzero spontaneous magnetization is known in the case of a distorted-kagome-lattice antiferromagnet[5], in which an incommensurate modulation appears in this intermediate state. In the present model between the triangular and dice lattices, on the other hand, such an incommensurate modulation is not observed. The spin structure of this nontrivial intermediate state with nonzero spontaneous magnetizations should be examined in future studies. Such studies will contribute to our understandings of this phenomenon and the nontrivial effect of frustration in magnetic materials.

References

- [1] H. Nakano and A. Terai: J. Phys. Soc. Jpn. **78** (2009) 014003.

- [2] H. Nakano and T. Sakai: to be published
in J. Phys. Soc. Jpn.
- [3] A. Jagannathan and A. Szallas: Eur.
Phys. J. B **86** (2013) 76.
- [4] E. Lieb and D. Mattis: J. Math. Phys.
(N.Y.) **3** (1962) 749.
- [5] H. Nakano, T. Shimokawa, and T. Sakai:
J. Phys. Soc. Jpn. **80** (2011) 043703.

Study on Statistical Physics Toward High-Performance Quantum Information Processing

Shu TANAKA

*Waseda Institute for Advanced Study, Waseda University
Nishi-waseda, Shinjuku, Tokyo 169-8050*

(I) Topological phase diagram and sweep dynamics of a generalized cluster-Ising model

Topological properties and their related dynamical phenomena are interesting topics in statistical physics, condensed matter physics, and quantum information science. To investigate the robustness of cluster phase which is a candidate for measurement-based quantum computation, we proposed a generalized cluster-Ising model [1]. The Hamiltonian of our model in one dimension is described by

$$\mathcal{H}_{\text{GCI}} = \sum_{i=1}^N (-J^{XZX} \sigma_i^x \sigma_{i+1}^z \sigma_{i+2}^x + J^{YY} \sigma_i^y \sigma_{i+1}^y + J^{YZY} \sigma_i^y \sigma_{i+1}^z \sigma_{i+2}^y).$$

We completed the ground-state phase diagram of our model, and the topological number of each topological phase is confirmed by numerical calculations [1, 2]. In addition, we considered dynamical properties of our model during interaction sweeps through the critical points of topological phase transition. We observed the topological blocking (or the so-called parity blocking) when we change the interaction so that the topological number changes.

This work was done in collaboration with Takumi Ohta (YITP, Kyoto University), Ippei Danshita (YITP, Kyoto University), and Keisuke Totsuka (YITP, Kyoto University).

(II) Quantum annealing for principal component analysis

Quantum annealing is a promising method

for finding the best solution of optimization problems [3, 4]. To investigate novel applications of quantum annealing is a significant topic. We proposed a method to perform the principal component analysis by quantum annealing. We implemented our method to data matrices with hierarchical structure and found that the choice of initial Hamiltonian affects the performance of quantum annealing.

This work was done in collaboration with Yoichiro Hashizume (Tokyo University of Science) and Ryo Tamura (National Institute for Materials Science).

References

- [1] T. Ohta, S. Tanaka, I. Danshita, and K. Totsuka: *J. Phys. Soc. Jpn.* **84** (2015) 063001.
- [2] T. Ohta, S. Tanaka, I. Danshita, and K. Totsuka: *Phys. Rev. B* **93** (2016) 165423.
- [3] T. Kadowaki and H. Nishimori, *Phys. Rev. E* **58** (1998) 5355.
- [4] S. Tanaka, R. Tamura, and B. K. Chakrabarti, “Quantum Spin Glasses, Annealing and Computation”, Cambridge University Press (2017).

Dynamical DMRG study of spin dynamics in spin-1/2 Inequilateral diamond-chain systems

Takami TOHYAMA

Department of Applied Physics, Tokyo University of Science, Tokyo 125-8585

Frustrated quantum magnets provide various exotic ground states such as gapless spin-liquid and gapped singlet dimer phases. The typical constituent of frustrated magnets is a triangular unit of spin with antiferromagnetic (AFM) interaction for each bond. The spin-1/2 diamond chain, where the triangular unit is connected linearly, is thus regarded as a typical frustrated system in one dimension. The azurite was originally suggested to be such a system, but a recent consensus is that it less frustrated.

Recently, a new highly one-dimensional (1D) diamond chain compound $K_3Cu_3AlO_2(SO_4)_4$ was reported [1]. In this compound, the magnetic susceptibility exhibits a double-peak structure similar to the azurite, but the temperatures of the peaks (50 K and 200 K) are one order of magnitude higher than those in the azurite. In spite of such high characteristic temperatures, there is no magnetic order down to 0.5 K, indicating a possible spin-liquid ground state. It is, thus, important to clarify common features characterizing the distorted diamond-chain compounds in both the azurite and the new compound.

We analyzed the temperature dependence of the magnetic susceptibility in $K_3Cu_3AlO_2(SO_4)_4$ by using the finite-temperature Lanczos and the exact diagonalization methods [2]. The estimated magnetic exchange interactions are found to form strong dimer bond and monomer-monomer chains. The interactions in a diamond Heisenberg model are shown in Fig. ???. The dimer-bond

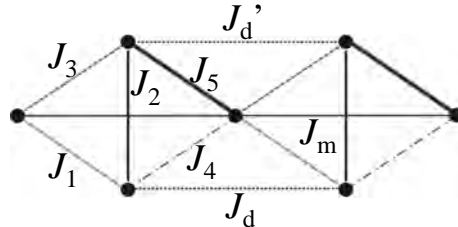


Figure 1: Effective spin model of $K_3Cu_3AlO_2(SO_4)_4$. The circles represent Cu^{2+} ions with spin 1/2. $J_1 = J_3 = J_4 = -30$ K, $J_2 = -300$ K, $J_5 = 510$ K, and $J_m = J_d = J'_d = 75$ K.

position as well as their energy scale is different. The frustration is less effective in $K_3Cu_3AlO_2(SO_4)_4$ than in the azurite and the spin-liquid behavior at low temperatures is attributed to an effective spin-1/2 Heisenberg chain.

Based on the estimated exchange interactions in $K_3Cu_3AlO_2(SO_4)_4$, we calculate the dynamical spin structure factor $S(q, \omega)$ defined by

$$S(q, \omega) = -\frac{1}{\pi N} \text{Im} \langle 0 | S_{-q}^z \frac{1}{\omega - H + E_0 + i\eta} S_q^z | 0 \rangle,$$

where q is the momentum for the triangular unit cell, $|0\rangle$ is the ground state of the diamond Heisenberg Hamiltonian H with energy E_0 , η is a broadening factor, N is the number of sites, and $S_q^z = N^{-1/2} \sum_i e^{iqR_i} S_i^z$ with R_i being the position of spin i and S_i^z being the z component of \mathbf{S}_i .

We use the dynamical density matrix renor-

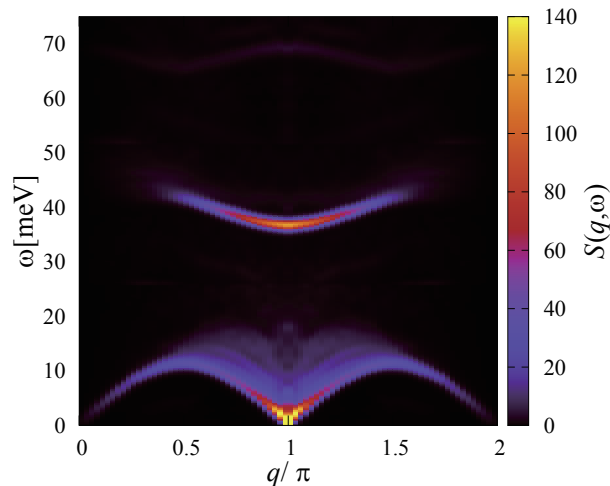


Figure 2: Dynamical spin structure factor $S(q, \omega)$ obtained by DDMRG for a 240-site periodic chain for $\text{K}_3\text{Cu}_3\text{AlO}_2(\text{SO}_4)_4$.

malization group (DDMRG) for a $N=240$ -site periodic chain (80 triangular cells). We use a multitarget scheme and one of the targets, $(\omega - H + E_0 + i\eta)^{-1} S_q^z |0\rangle$, is evaluated by using a kernel-polynomial expansion method [3]. In our kernel-polynomial expansion method, the Lorentzian broadening given by η is replaced by a Gaussian broadening with half width at half maximum 0.65 meV. In our numerical calculations, dividing the energy interval $[0, 60]$ meV by 186-mesh points and $[60, 75]$ meV by 46-mesh points, we targeted all of the points for each interval at once.

The truncation number $m = 400$ and the truncation error is less than 7×10^{-3} . The value of η is taken to be 0.65 meV.

Figure 2 shows the contour plot of $S(q, \omega)$. At the low-energy region below 10 meV, we find a clear dispersive behavior fitted quite well by $(\pi/2)J|\sin q|$ with $J = J_d$. This indicates that the lowest-energy branch comes from the 1D Heisenberg chain connected by the J_d bond. At high energy region around 40 meV, there is a dispersive structure having a minimum at $q = \pi$. This is nothing but the dispersion of a dimer predominantly formed on the J_5 bond. The dispersion relation is well re-

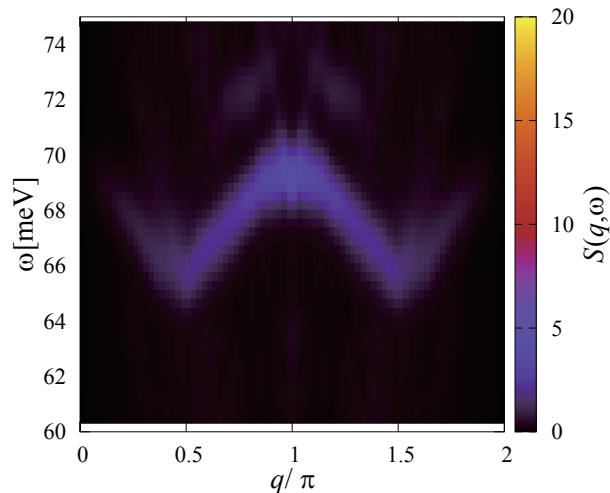


Figure 3: The same as Fig. 2, but higher energy region.

produced by $\omega_q = J_5 + J_m \cos q + \frac{1}{4} J_m^2 / J_5 (3 - \cos 2q)$. Both the low-energy and high-energy structures have been confirmed for the powder sample of $\text{K}_3\text{Cu}_3\text{AlO}_2(\text{SO}_4)_4$ [4].

There are small but dispersive spectral weights around 65 meV. Figure 3 exhibits this energy region. Judging from the energy scale, we assign these structures to be double dimer excitations. These have not yet been observed experimentally and thus detecting them remains to be a challenging problem.

References

- [1] M. Fujihala *et al.*: J. Phys. Soc. Jpn. **84** (2015) 073702.
- [2] K. Morita *et al.*: Phys. Rev. B, in press.
- [3] S. Sota and T. Tohyama, Phys. Rev. B **82** (2010) 195130.
- [4] M. Fujihala *et al.*: to be published.

Dynamical scaling analysis for the antiferromagnetic triangular Heisenberg model

Y. Ozeki and R. Tobise

Graduate School of Informatics and Engineering, The University of Electro-Communications

We investigate the topological phase transition expected to appear in the antiferromagnetic (AF) triangular Heisenberg model by the use of the dynamical scaling analysis [1]. In 2D continuous spin systems, while it has been well-known that there is no long-range order with continuous symmetry-breaking, there might be phase transitions for a discrete symmetry-breaking or for a topological phase with no long-range order. In the nonequilibrium relaxation (NER) analysis for the AF triangular XY case [2], two dynamical order parameters are analyzed from a so-called 120° structure. The one is the orientational order parameter defined by the projection of spin vector to the direction of the initial state, $\cos(\theta_i - \theta_{i0})$, and the other is the chiral order parameter defined by the vector product of nearest neighboring spin pair, $\sin(\theta_i - \theta_j)$. It has been found that the chiral order parameter shows a second order transition with a discrete symmetry-breaking (the chiral phase) and the orientational order parameter shows a topological phase transition, the Kosterlitz-Thouless (KT) one.

Similar transitions have been explored in the Heisenberg case, and discussed for a long time [3]. In the present study for the Heisenberg case, we will estimate the transition temperature precisely using the NER method [2] with recently improved dynamical scaling analysis [1]. The chiral order parameter forms a vector, $\vec{m} = \frac{1}{N} \sum_{i \rightarrow j} \vec{S}_i \times \vec{S}_j$, where summation is taken over all nearest-neighboring pairs with fixed direction. We simulate the relaxation from a 120° structure in the XY -plane, and measure the z -component and the square of $\vec{m}(t)$.

Calculations are carried out for 2000×2001 triangular lattice with skew boundary condition up to an observation time of 10^5 MCSs. For each temperature, 864 samples are taken for statistical averaging. In the dynamical scaling analysis for the NER method, a general scaling form is examined;

$$m(t, T) = \tau^{-\lambda} \Psi(t/\tau),$$

where $\tau(T)$ is the relaxation time, which is expected to diverge as $\tau(T) = a \exp(b/\sqrt{T - T_{KT}})$ for the KT transition. The resulting scaling plot is

shown in Fig. 2 with $T_{KT} = 0.280$ and $\lambda = 0.109$.

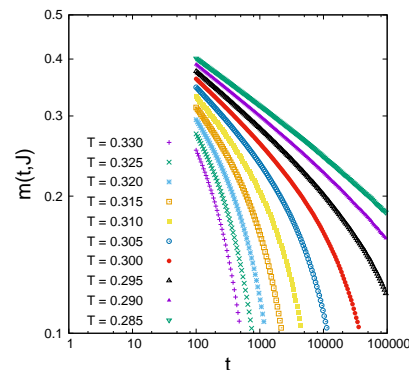


Figure 1: Relaxation of the z -component.

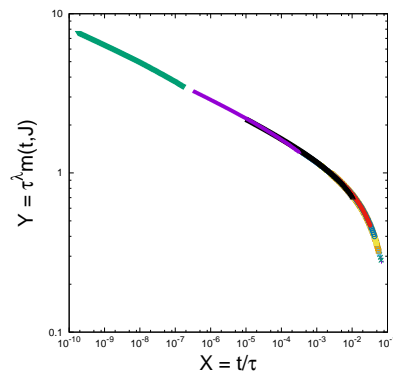


Figure 2: Scaling plot

References

- [1] Y. Echinaka and Y. Ozeki, Phys. Rev. E **94** 043312 (2016).
- [2] Y. Ozeki and N. Ito, Phys. Rev. B **68** 054414 (2003); Y. Ozeki and N. Ito, J. Phys. A: Math. Theor. **40** R149 (2007).
- [3] H. Kawamura and S. Miyashita, J. Phys. Soc. Jpn. **53** 4138 (1984); H. Kawamura, et. al., J. Phys. Soc. Jpn. **79** 023701 (2010).

Development of direct method for quantum response from microscopic Hamiltonian

Seiji MIYASHITA

*Department of Physics, University of Tokyo
Hongo, Bunkyo-ku, Tokyo 113-0033*

Quantum response and Quantum dynamics

We have studied the following topics related to quantum response and quantum dynamics.

1. Size- and temperature- dependences of ESR line-shape of the one-dimensional XXZ chain

We introduced a method to decompose the spectrum into contributions specified by the magnetizations of the resonating states, and applied the so-called moment method for each contribution. By making use of it, the size and temperature dependences of the ESR spectrum of the 1DXXZ spin model have been obtained [1].

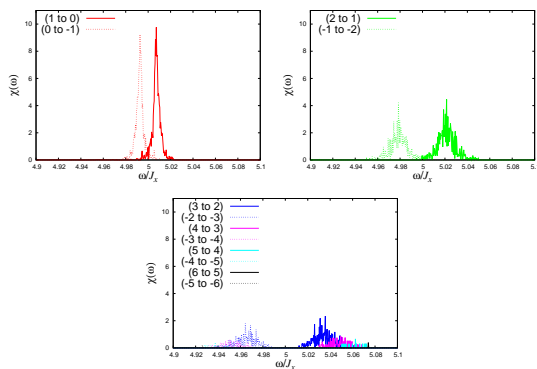


Figure 1: Spectra for classified by the magnetizations ($M = 1, 2$ and others) of transitions at $\beta^{-1} = 100\text{K}$.

2. Synergistic effects of the spin-orbit interaction and the external field on the

optical conductivity

Synergistic effects of the spin-orbit interaction and the external field on the optical conductivity of the Hubbard model were studied. In one-dimensional noninteracting case ($U = 0$: the tight-binding model), we obtained exact result of the effect as a function of the angle between the directions of the spin-orbit interaction and the external field. For the interacting case, we studied the model numerically and found the angle dependent properties.[2]

3. Population dynamics of the quantum Storer-Wohlfarth model

We have studied the relaxation of metastable state of magnetization under sweeping field in a uniaxial magnetic systems. In the fiscal year, we studied the spin size S dependence of the population dynamics over the adiabatic eigenstates after the Storer-Wohlfarth point, and found some universal aspects of the distribution which survives in the classical limit. We also studied the effect of thermal decoherence on the quantum beating which was found in the previous paper.

4. Thermal distribution of stationary state of periodically driven quantum systems

Properties of periodically driven systems are characterized by the Floquet state, and the quasi-eigenenergy state of Floquet state has been studied from the view point of development of new states under periodic external

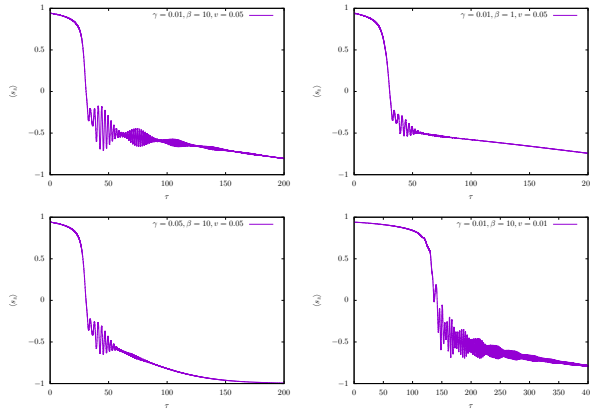


Figure 2: Relaxation of the quantum beating of the quantum Stoner-Wohlfarth model.

field. We have studied the thermal distribution over the quasi-eigenenergy levels, and examined the conditions for the realization of the distribution [3].

5. Thermalization of isolated quantum systems

We formulate this problem as a general problem of the ensemble equivalence [4]. We showed that the system thermalizes when the effective dimension of the initial state is sufficiently large but may be exponentially smaller than the dimension of the Hilbert space.

We also consider the problem of the second law of thermodynamics from the viewpoint of the ensemble equivalence. We proved that the amount of increase of the entropy of the system must be extensively large, i.e. proportional to the system size, by using the large deviation property of the equilibrium state of a macroscopic quantum system [5].

6. Related topics

We also studied cooperative systems, such as the frustrated systems, microscopic mechanisms of the coercive force of permanent magnets, spin-crossover systems, etc. [6, 7, 8, 9].

We also studied fundamental properties of the quantum master equation (QME). Usually QME is perturbatively derived by tracing

out the degree of freedom of the thermal bath. We demonstrated this procedure in a spin system. We found that properties obtained by the QME derived by the perturbation method qualitatively agree with the numerical results, but quantitatively they differ each other [10].

References

- [1] Hiroki Ikeuchi, Hans De Raedt, Sylvain Bertaina, and Seiji Miyashita, Phys. Rev. B **95**, 024402 (2017).
- [2] Adrien Bolens, Hosho Katsura, Masao Ogata, Seiji Miyashita, ArXiv:1704.03153.
- [3] Tatsuhiko Shirai, Juzar Thingna, Takashi Mori, Sergey Denisov, Peter Hanggi and Seiji Miyashita, New J. Phys. **18**, 053008 (2016).
- [4] Takashi Mori, Phys. Rev. E **94**, 020101(R) (2016).
- [5] Takashi Mori, J. Phys. A **49**, 44403 (2016).
- [6] Masamichi Nishino, Yuta Toga, Seiji Miyashita, Hisazumi Akai, Akimasa Sakuma and Satoshi Hirokawa, Phys. Rev. B **95**, 094429 (2017).
- [7] Masamichi Nishino and Seiji Miyashita, Phys. Rev. B **94**, 184434 (2016).
- [8] Yuta Toga, Munehisa Matsumoto, Seiji Miyashita, Hisazumi Akai, Shotaro Doi, Takashi Miyake, and Akimasa Sakuma, Phys. Rev. B **94**, 174433 (2016).
- [9] Sasmita Mohakud, Sergio Andraus, Masamichi Nishino, Akimasa Sakuma, and Seiji Miyashita, Phys. Rev. B **94**, 054430 (2016).
- [10] P. Zhao, H. De Raedt, S. Miyashita, F. Jin, and K. Michielsen, Phys. Rev. E **94**, 022126 (2016).

Numerical studies of bulk-edge correspondence

Y. Hatsugai

*Division of Physics, University of Tsukuba
1-1-1 Tennodai, Tsukuba 305-8571, Ibaraki, Japan*

Recent intense studies of topological phases have revealed that variety of materials, that are characteristic but can not be well described by a conventional classification based on a symmetry, is quite wide. They are topological in a sense that topological quantities such as the Chern number or the Berry phase are non trivial for the bulk. However these bulk quantities are mostly hidden and can not be easily observed experimentally. Topological implies hidden. Then experimental tools to identify the phase as non trivial are edge states such as the surface Dirac cones of the topological insulators where the angle resolved photoemission spectroscopy (ARPES) directly measures them. Topologically non trivial bulk induces localized modes when the system has boundaries or geometrical defects. This is the bulk-edge correspondence. We have demonstrated this bulk-edge correspondence in many of quantum systems[1, 2, 3, 4].

One of the recent important developments is that the concept of the topological phase can be extended beyond quantum world into classical systems such as photonic crystals governed by the Maxwell equation and even for the classical mechanics obeying the Newton equation.

We have numerically demonstrate this bulk-edge correspondence without quantum mechanics in two classical systems. One is a three dimensional photonic crystal[5]. The section Chern number defined for a propagating mode with fixed direction can be non zero when the three dimensional system breaks spatial inversion. Then the topological change of the section Chern number implies the existence of the Weyl point that is also reflected by the boundary modes as an example of the bulk-edge correspondence (See Figure 1).

The other one is a classical mechanics. This is just a simple spring mass model arrayed in a diamond lattice. The bulk frequency spectrum has a singular behavior known as a line node protected by the chiral symmetry. These line nodes in the three dimensional Brillouin zone is shown in Figure 2. Topological change of the line nodes induced by the tension change are clearly demonstrated. The symmetry protecting the line nodes of the bulk spectrum also guarantees quantization of the Berry phase of the multibands of the classical system, which directly reflected by momentum dependent boundary modes[6].

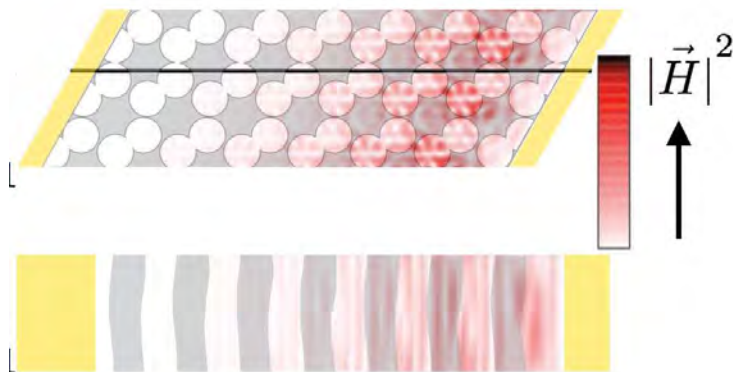


Figure 1: Edge states of a three dimensional photonic crystal without spatial inversion symmetry[5].

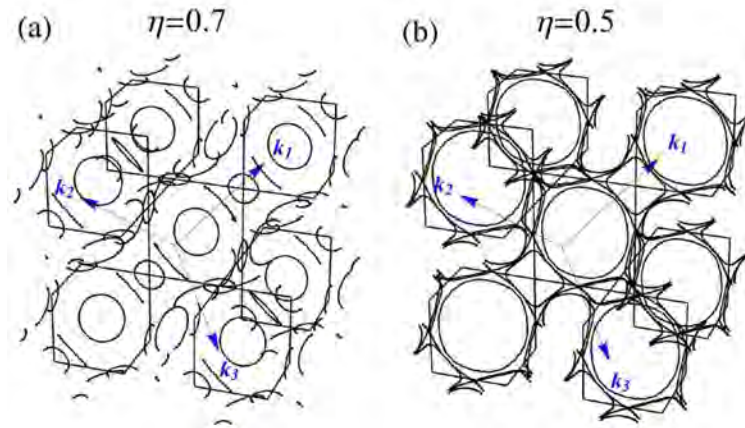


Figure 2: Line nodes of the mechanical diamonds[6] with different tension. Topological phase transition between the phases is clearly demonstrated.

References

- [1] Y. Hatsugai, T. Fukui, Phys. Rev. B 94, 041102(R) (2016), DOI: 10.1103/PhysRevB.94.041102
- [2] T. Fukui, Y. Hatsugai, J. Phys. Soc. Jpn 85, 083703 (2016), DOI: 10.7566/JPSJ.85.083703
- [3] A. Hattori, S. Tanaya, K. Yada, M. Araidai, M. Sato, Y. Hatsugai, K. Shiraishi, Y. Tanaka, J. Phys. Cond. Mat. 29, 115302 (2017), DOI: 10.1088/1361-648X/aa57e0
- [4] T. Kawarabayashi, H. Aoki, Y. Hatsugai, Phys. Rev. B94, 235307 (2016), DOI: 10.1103/PhysRevB.94.235307
- [5] S. Oono, T. Kariyado, Y. Hatsugai, Phys. Rev. B94, 125125 (2016), DOI: 10.1103/PhysRevB.94.125125 (selected as editors's suggestion)
- [6] Y. Takahashi, T. Kariyado, Y. Hatsugai, New J. Phys. 19, 035003 (2017), DOI:10.1088/1367-2630/aa5edb

Role of dimensionality on the glassy fluctuation

Hayato SHIBA

*Institute for Materials Research, Tohoku University
Katahira, Aoba-ku, Sendai 980-8577*

Dimensionality plays a key role in the physics of solids and liquids. Fluctuation shows up differently in different spatial dimensions, as typically observed in phase transitions. Two-dimensional (2D) crystalline solids often exhibit enhanced fluctuations that span an infinite length that induces long-wavelength structural correlations. A glassy system, on the other hand, lacks the crystalline order and endows the random liquid-like structure. As a consequence, structural (static) correlations cannot represent the dimensionality dependence. We need to look into dynamical aspects to clarify the dimensionality dependence of such systems.

With the use of ISSP supercomputer, we have shown that fluctuation is dependent on the spatial dimensions, but the modality of inherent structural relaxation is similar between 2D and 3D [1]. Extensive simulations are performed for both a 2D binary mixture of 12th-core repulsive potential and a 3D binary mixture of Kob-Andersen-type Lennard-Jones potential, with up to 256,000 and 10,240,000 particles, respectively. We clarified enhancement of 2D fluctuation taking place due to a mechanism similar to Mermin-Wagner theorem for a 2D crystal, by direct calculation of the Debye-asymptote of the vibrational density of states, which also accounts for enhanced fluctuation recently observed in 2D systems [2]. It leads to system-size dependent behavior of the estimated relaxation time and dynamic correlation length in the 2D system in terms of the density-based correlation functions. However, such size dependence is eliminated by intro-

duction of an alternative correlator that characterizes relative rearrangement motions of the particles.

We also treated the glassy dynamics at low-temperature near the jamming and glass transitions. Based on the extensive normal mode analysis of 2D and 3D particle assemblies with large system sizes. In 2D, we have found that the vibrational modes are divided into two groups below the boson peak. One group of the modes converge to the phonons following the Debye law $g_{\text{ex}}(\omega) = A_0\omega^2$, and the other to the soft localized modes following another universal non-Debye scaling $g(\omega) \sim \omega^4$. Strikingly, all the non-phonon contributions to the vDOSs at different pressures can be expressed as a universal function of the frequency. In contrast, completely different behaviors are observed in 3D; vibrational modes smoothly converge to phonons without appearance of the group of the soft localized modes [3].

References

- [1] H. Shiba, Y. Yamada, T. Kawasaki, and K. Kim, Phys. Rev. Lett. **117**, 245701 (2016).
- [2] H. Shiba, T. Kawasaki, and A. Onuki, Phys. Rev. E **86**, 041504 (2012).
- [3] H. Mizuno, H. Shiba, and A. Ikeda, submitted.

Metastability and Hysteresis in Chiral Helimagnet

Misako SHINOZAKI and Yusuke KATO

*Department of Basic Science, The University of Tokyo
Komaba, Meguro-ku, Tokyo, 153-8902, Japan*

The competition between the Heisenberg exchange and the uni-axial Dzyaloshinskii-Moriya (DM) interactions gives rise to a long-period helical magnetic texture called a chiral helimagnetic state. We investigate the thermodynamic properties of the three-dimensional chiral helimagnets under the external field perpendicular to the helical axis using a mean-field method. The winding number, or number of chiral solitons, is essential factor when the finite-size helical systems are considered, and it makes the numerical calculation difficult. To solve the mean-field equations efficiently, we prepare many initial states and solve the equations for each state using a parallel programming.

First, we analyze a phase diagram of the chiral helimagnets particularly paying attention to the order of the phase transition and the crossover phenomena. We found two critical points which separate the first-order and second-order transitions. We evaluate the height of the energy barrier which creates the double minimum structure in the free-energy profile in the first-order transition region. By comparing the height of the energy barrier with thermal energy (i.e. $k_B T$), we elucidate the condition in which the first-order transition signature is observable. Around the transition temperature at very low field, the magnitude of the local spin moments becomes small, so that a new spin structure called chiral-fan structure is stabilized. We show that the chiral-fan region is related to the crossover line defined on the basis of the susceptibility.

We also analyze a finite-size effect on the

physical properties of the chiral helimagnets. The specific heat and susceptibility respectively show the small delta peaks and step-like behavior caused by the discrete change of the winding number at low temperature. Recently, experimental studies have shown hystereses in the magnetization [1, 2] and magneto-resistance [3] using small CrNb_3S_6 samples, which often involve step-like behavior. Although these hystereses can be related to the finite-size effect, the relation between the finite-size effect and hysteresis has not been investigated theoretically so far. Using various boundary conditions, we show that many local minima appear in the free-energy profile as the magnetic field increases. By simulating the decreasing external field process numerically, we clarify the relations between these local minima and hystereses.

References

- [1] T. Moriya and T. Miyadai, *Solid State Commun.* **42**, 209 (1982).
- [2] K. Tsuruta, M. Mito, Y. Kousaka, J. Akimitsu, J. Kishine, Y. Togawa, H. Ohsumi, and K. Inoue, *J. Phys. Soc. Jpn.* **85**, 013707 (2016).
- [3] Y. Togawa, T. Koyama, Y. Nishimori, Y. Matsumoto, S. McVitie, D. McGrouther, R. L. Stamps, Y. Kousaka, J. Akimitsu, S. Nishihara, K. Inoue, I. G. Bostrem, Vl. E. Sinitsyn, A. S. Ovchinnikov, and J. Kishine, *Phys. Rev. B* **92**, 220412 (2015).

Predicting a melting curve and structure of melt

Kazuhiro Fuchizaki, Kazuma Okamoto, and Takahiro Sakagami
Department of Physics, Ehime University, Matsuyama 790-8577

Yuta Asano

The Institute for Solid State Physics, The University of Tokyo, Kashiwa 277-8581

We have investigated an effective way with which to predict the accurate location of a phase boundary of a particle system, and arrived at a method that applies nonequilibrium relaxation (NER) [1], which has been established for determining the phase-transition point of a spin system. The method was devised to determine the equilibrium melting curve of the modified Lennard-Jones (mLJ) system [2]. The method, reported first, was further improved, and could predict the location of not only the solid–liquid but also the liquid–gas and solid–gas phase boundaries of the mLJ system. This improved method was then mentioned. Finally, we report our recent important findings, regarding orientational order in liquid SnI_4 and GeI_4 , achieved by using the system B of the facility.

A new way for determining a melting curve

To locate the transition point for a particle system, an orthodox way to employ is to compare the free energies of the relevant phases, which are usually evaluated using a thermodynamic integration. The evaluation of free energy consists of multiple stages of computation, and the orthodox way requires much processing cost to identify a single transition point of a particle system. The NER method [1] has been used also as an effective tool with which to locate the equilibrium phase transition point of a system from an equilibrating stage, which is usually discarded from the calculation of equilibrium quantities. It is therefore worth trying to apply the NER method to a particle system to address the high cost of

processing.

We first tried to determine a melting curve. To this end, we employed the mLJ system because the accurate melting points are known as a function of pressure [2]. The key for the NER to work properly in determining a transition point is a choice of an appropriate initial state. We prepared a combined system consisting of a solid system (13500 particles were located on the face-centered cubic lattice points in a cube with the density $\rho = 1.0$) and a liquid system (14196 particles in a rectangular parallelepiped brought into a well disordered state at the temperature $T = 10$, a sufficiently high temperature for the mLJ system) as a trial initial state, from which the isothermal–isobaric time evolution was traced conducting a molecular dynamics (MD) simulation to measure ρ of the whole system as a function of time. If a chosen T is higher (lower) than the transition temperature under the pressure p , the whole system would become a liquid (solid) state so that ρ would decrease (increase). The melting point could thus be found with a desired accuracy by choosing such T as ρ hardly relaxes.

The result was satisfactory [3]; the NER method could reproduce the previous melting points [2]. However, a slight discrepancy is recognizable in a low-pressure region ($p < 1$). This discrepancy was removed by taking a slightly lower initial $\rho = 0.95$ for the solid density. (The setting of the initial $\rho = 1.0$ was rather suitable for investigation of the melting points in a high-pressure region.)

Improvement and extension of the method

The important ingredient of the method is preparation of a coexistence state. In the NER method [3], the coexistence state was prepared by “mechanically” combining equilibrium solid and liquid states under isothermal and isobaric conditions. Extreme care must be taken when joining the two states so as not to cause instability at the interface. This is because the equal pressure of the states to be combined is not necessarily a sufficient condition for the states to come to equilibrium in a rectangular parallelepiped simulation box.

This situation was improved in such a way that a solid–liquid coexistence state was generated by elongating the box containing a solid phase in one direction under isothermal conditions. The system has no free surface because of periodic boundary conditions imposed in all directions. The deformation then allows to produce a solid–liquid interface perpendicular to the direction of elongation in the elongated simulation box. Under the isobaric conditions, the interface moves in the simulation box, which is to be completely filled with a solid or a liquid state depending on the temperature. The melting temperature was defined as the midpoint between the two temperatures. The width between the midpoint and the highest (lowest) temperature then gave the probable error associated with the melting temperature thus defined. The melting points thus obtained are plotted in Fig. 1. The result coincides with the one [2] within statistical errors. The method was further extended so as to be assisted by the Clausius–Clapeyron relationship, thereby predicting the nearby melting points. The present method could be adopted to predict also the liquid–gas and solid–gas phase boundaries of the m LJ system. In particular, the triple point was identified to be $T_t = 0.611(4)$ (which improved the result [2] by an order of magnitude) and $p_t = 0.0013(1)$. Together with the critical point examined based on the renormalization-group approach [4], the phase diagram of the

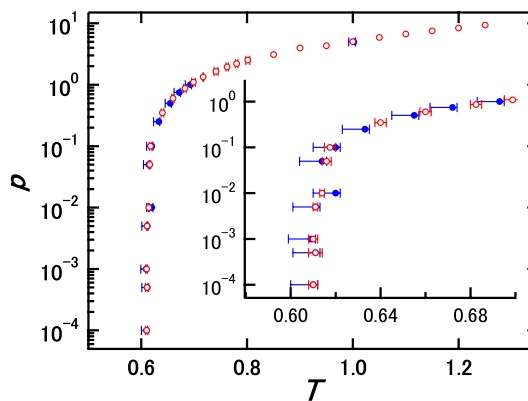


Figure 1: The melting points established from the free-energy balance [2] are designated by blue symbols whereas those obtained through the present method for a 5000-particle m LJ system are designated by red symbols.

m LJ system is said to be established.

Liquid structure of GeI_4 and SnI_4

The structure of these molecular liquids at ambient pressure was closely examined using the reverse Monte Carlo (RMC) method. Liquid structures obtained through the MD simulation [5] as input. We first developed an expedient method [6] for estimating density of liquids from the structure factor as the density is also an important input to the RMC analysis. A possible pressure-induced network formation consisting of molecules with the vertex-to-face orientation was suggested [7].

References

- [1] N. Ito: *Physica A*, **192** (1993) 604; *ibid.* **196** (1993) 591.
- [2] Y. Asano and K. Fuchizaki: *J. Chem. Phys.* **137** (2012) 174502.
- [3] Y. Asano and K. Fuchizaki: *J. Phys. Soc. Jpn.* **86** (2017) 025001.
- [4] K. Okamoto and K. Fuchizaki: *J. Phys. Soc. Jpn.* **86** (2017) 034003.
- [5] K. Fuchizaki and Y. Asano: *J. Phys. Soc. Jpn.* **84** (2015) 064601.
- [6] T. Sakagami, K. Fuchizaki, and K. Ohara: *J. Phys.: Condens. Matter.* **28** (2016) 395101.
- [7] T. Sakagami and K. Fuchizaki: *J. Phys.: Condens. Matter.* **29** (2017) 145102.

A construction of the Markov state model of protein folding using the manifold theory

Takashi YOSHIDOME

Department of Applied Physics,

Tohoku University, 6-6-05, Aoba, Aramaki, Aoba-ku, Sendai 980-8579

Recently, Markov state model (MSM) [1] is a promising model for analyzing long-time behaviors of proteins, which are difficult to investigate using the conventional molecular dynamics (MD) simulations. Its construction consists of the following three steps:

- (i) Classification the protein conformations into the major states obtained using MDs,
- (ii) Calculation the transition matrix between the states, and,
- (ii) Computation physical quantities using the master equation.

Although constructions of a MSM for proteins has been performed for a decade, quantitative performance of the physical quantities was poor at long-time scales [1]. It was considered that an origin of the poor performance is failure of the classification into states (step (i)).

In the present stud, we proposed to use the manifold learning for the classification. To demonstrate its usefulness, we constructed a MSM using MD data to investigate the folding of a protein. First, we performed MD simulations of proteins. Then classifications of

the data were conducted using our custom-made software “EMMA” [2] in which the diffusion map method based on the manifold learning was implemented. All computations were performed using the system B (F4cpu, L4cpu, L36cpu, and L2fat) at the Supercomputer Center in the Institute for Solid State Physics at the University of Tokyo. Finally, we constructed a MSM of a protein using the states obtained with the manifold learning.

By comparing a physical quantity obtained using the MSM with that obtained by the MD, we found that the MSM was a high quantitative performance even at long time scales. This result indicates that MSM using manifold leaning is effective.

References

- [1] V.S. Pande, K. Beauchamp, and G.R. Bowman, *Methods*, **99**, (2010).
- [2] T. Yoshidome, T. Oroguchi, M. Nakasako, and M. Ikeguchi, *Phys. Rev. E*, **92**, 032710 (2015).

Utilizing AVX2 instructions for molecular dynamics simulation of Lennard-Jones potential

Hiroshi Watanabe

*Institute for Solid State Physics, University of Tokyo
Kashiwa-no-ha, Kashiwa, Chiba 277-8581*

Since early 2000s, the increase in the clock rates of computers has stopped. The development of the performance has mainly been achieved by increasing the number of processing cores and the width of SIMD (single instruction, multiple data). The bit length of register is 256 in AVX (Advanced Vector Extensions) and is 512 in AVX-512 instruction sets. It is difficult to generate efficient codes for such architecture automatically, and therefore, a programmer has to write them explicitly. In this report, we describe an algorithm to utilize AVX2 instruction for calculating force of Lennard-Jones potential.

The AVX2 instruction set uses registers with 256-bit width. Each register can contain four 64-bit double-precision floating point numbers like a vector and floating operations can be performed for all elements of the vector simultaneously. The basic idea of utilizing 256-bit registers is as follows, i) unfold a loop by four times, ii) calculate forces of four atom pairs, and iii) store the results. However, a naive implementation of the above procedure is highly inefficient since it involves memory access many times which becomes a performance bottleneck. To address this problem, we change data structure. Figure 1 illustrates how the data are stored in registers. (a) The crucial idea is to prepare four dimensional array for three dimensional system. While we use only three-quarters of memory, we can load three components of coordinate to a register simultaneously. (b) We calculate a relative co-

ordinates by a single subtraction. (c) After calculating relative coordinates of four pairs, we transpose a data. Then taking sum of squares gives for squared distances of for pairs. Then we can calculate forces of four pairs simultaneously.

This optimization gives us 2.23 times speed-up compared to a code without the SIMD optimization. This result shows that the data structure is a key to utilize SIMD instructions effectively. A sample code is available online [1].

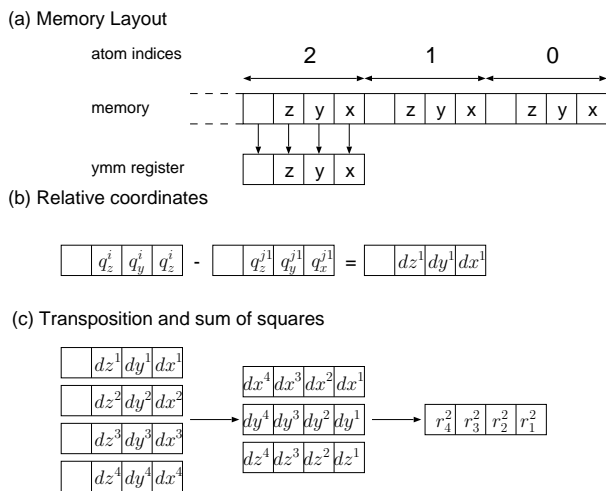


Figure 1: Data layout in registers.

References

[1] https://github.com/kaityo256/lj_simdstep

Dynamical ordering of amyloid fibrils by molecular dynamics simulations

Satoru G. Itoh and Hisashi Okumura

*Research Center for Computational Science,
Institute for Molecular Science, Okazaki, Aichi 444-8585*

The amyloid- β peptide ($A\beta$) is composed of 39–43 amino-acid residues. $A\beta$ tends to form amyloid fibrils, which are associated with the Alzheimer's disease. To understand amyloid fibril formation, we have performed molecular dynamics (MD) simulations of amyloid fibrils [1, 2, 3].

It was reported that formation of amyloids is accelerated at a hydrophilic/hydrophobic interface such as an air/water interface or an interface between sugar-head groups and hydrocarbon chains of glycolipids. It is necessary to clarify the amyloid formation process at the interface in order to find a remedy for Alzheimer's disease.

To investigate amyloid formation process at the hydrophilic/hydrophobic interface, we performed Hamiltonian replica-permutation molecular dynamics (RPMD) simulations for a full-length $A\beta$ molecule, $A\beta_{40}$, in the presence of the interface, as shown in Fig. Hamiltonian

As a snapshot shown in Fig. 1, residues in the $\beta 1$ and $\beta 2$ regions existed at the interface. Furthermore, these residues tended to form helix structures. These results agree well with

experiments.

We will analyze the $A\beta$ conformation at the interface and that in bulk water in more details. We will also discuss effects of the interface on the amyloid formation.

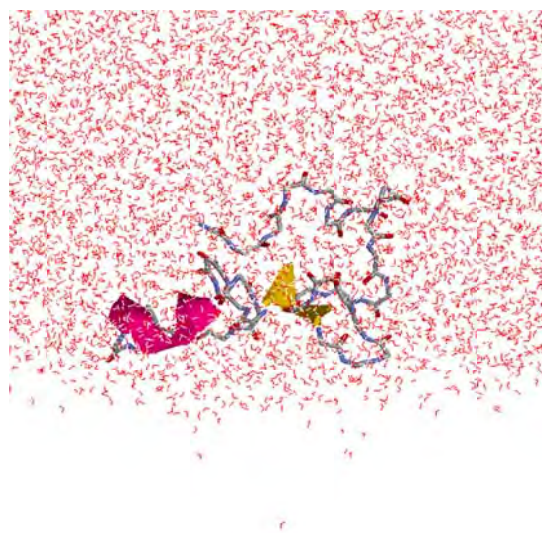


Fig. 1: Snapshot obtained by a Hamiltonian RPMD simulation.

References

- [1] H. Okumura and S. G. Itoh: *J. Am. Chem. Soc.* **136** (2014) 10549.
- [2] S. G. Itoh and H. Okumura: *J. Phys. Chem. B* **118** (2014) 11428.
- [3] S. G. Itoh and H. Okumura: *J. Comput. Chem.* **120** (2016) 6555.

Quantum Monte Carlo study of spin liquids

Yoshi KAMIYA

Condensed Matter Theory Laboratory,

RIKEN, Wako, Saitama 315-0115

As in our proposal, we initially ran world-line Quantum Monte Carlo (QMC) simulations for a toric code in a staggered magnetic field, which corresponds to the anisotropic limit of the honeycomb-lattice Kitaev model in a [001] magnetic field. We obtained the temperature and field dependence of several thermodynamic quantities, such as magnetization. However, later on, we realized that the model can be mapped onto a free fermion model and thus can be solved analytically [1], and we ceased to continue our numerical analysis on this model.

We changed our subject and decided to study an interacting Majorana fermion system to describe Majorana q-bits on the surface of a strong topological insulator that is proximate to an ordinary superconductor with an Abrikosov vortex lattice induced by an external magnetic field; each Majorana degree of freedom corresponds to a zero-mode bound to a vortex [2]. The non-interacting limit at the so-called neutrality point belongs to topological class BDI, in which Majorana fermion bilinear terms are prohibited due to an extra symmetry [3], resulting in a minimal Hamiltonian that comprises only quartic terms. We put such a system on the square lattice (instead of more

normal triangular lattices, by assuming for instance an array of impurities), as originally proposed by Chiu and coworkers [4]. By mapping the fermionic system to a quantum spin system using the Jordan-Wigner transformation, we apply the QMC simulations to study the phase diagram as a function of the temperature and a lattice distortion parameter. According to our preliminary investigation, the system without the lattice distortion undergoes a finite-temperature phase transition that induces a sort of density wave order breaking the translational symmetry spontaneously. We believe that this interesting observation deserves an extra investigation and the results will be reported elsewhere.

References

- [1] Y. Kamiya, J. Yoshitake, Y. Kato, J. Nasu, and Y. Motome: in preparation.
- [2] L. Fu and C. L. Kane: *Phys. Rev. Lett.* **100** (2008) 096407.
- [3] J. C. Y. Teo and C. L. Kane: *Phys. Rev. B* **82** (2010) 115120.
- [4] C.-K. Chiu, D. I. Pikulin, and M. Franz: *Phys. Rev. B* **91** (2015) 165402.
- [5] Y. Kamiya and G.-W. Chern: in preparation.

Stochastic Optimization Approach to Phase Transitions and Structure Search

Syngé Todo

Department of Physics, University of Tokyo, Tokyo 113-0033, Japan
Institute for Solid State Physics, University of Tokyo, Kashiwa, 277-8581, Japan

In this project, we developed several new and powerful techniques based on stochastic optimization and other methods for investigating various exotic critical phenomena in strongly correlated systems and determining crystal structure of materials.

Quantum critical phenomena of systems with strong spatial and temporal anisotropy: we have developed a method for evaluating the dynamical exponent z at the quantum critical point by combining the path-integral quantum Monte Carlo method and the stochastic optimization method [1]. By using our novel method, the coupling constant as well as the aspect ratio between the real-space and imaginary-time system sizes are tuned during the simulation, and the critical point, critical amplitude, spin-wave velocity, etc, can be automatically evaluated in a very accurate way. We extended our method to the one-dimensional random Heisenberg model and demonstrated that we can clearly distinguish the random singlet phase from the quantum Griffith phase as the distribution of strength of random bonds is altered.

Spinon linear dispersion relation at the deconfined quantum critical point: we performed a large scale simulation of the two dimensional J - Q model and elucidated a linear dispersion relation of spinon by using the path-integral quantum Monte Carlo and generalized moment method [2]. We found a non-trivial degeneracy in singlet and triplet excitations,

which suggests the emergence of a higher symmetry than that of the Hamiltonian.

Strange correlator for two-dimensional SPT phase: we developed a new method to calculate the *strange correlator*, which is proposed recently as an order parameter that identifies symmetry protected topological (SPT) phase in one and two dimensional quantum lattice models. It was confirmed that in the $S = 1$ bond-alternating antiferromagnetic Heisenberg chain we can distinguish the Haldane phase from the trivial dimer phase clearly by using the strange correlator. Our method can be applied straightforwardly to the SPT phase in two dimensions.

Critical decay exponent of long-range interacting spin models: using the $O(N)$ cluster algorithm [3], we studied precisely the critical exponents and critical amplitudes of the long-range interacting Ising model on the square lattice. In addition, we have introduced a universal method, the *combined Binder ratio*, by which the leading corrections to scaling can be automatically removed even near the critical decay exponent, and established the phase diagram in which the critical amplitude changes as the effective dimension of the system does according to the changes of decay exponent of the interaction [4]. We also performed a preliminary simulation on the effective dimension at the criticality in the system with spatially correlated random external fields.

Combined optimization method and application to determination of crystal structure: we developed a new method, the combined optimization method (COM), for simultaneously optimizing two cost functions that share the same global minimum point. It was demonstrated that one can reach the global minimum of the sum of multi-valley functions by using the COM with much higher probability than the conventional method, such as the simulated annealing. We have applied our method for the problem of crystal structure determination of the materials. As for the two different cost functions, we introduced the total energy calculated by the simulation (classical force field or the first-principles calculation) and the *crystallinity* that is defined as a difference between the experimental and the calculated X-ray diffraction patterns. We confirmed that we the correct crystal structures can be predicted with much higher probability than the optimization the calculated total energy or the crystallinity alone.

The programs used in the present project have been developed based on the following open-source libraries: ALPS [5, 6], ALPS/looper [7], BCL [8], and worms [9].

References

- [1] S. Yasuda, H. Suwa, and S. Todo: Phys. Rev. B **92** (2015) 104411.
- [2] H. Suwa and S. Todo: Phys. Rev. Lett. **115** (2015) 080601.
- [3] K. Fukui and S. Todo: J. Comp. Phys. **228** (2009) 2629.
- [4] T. Horita, H. Suwa, and S. Todo: Phys. Rev. E **95** (2017) 012143.
- [5] B. Bauer, L. D. Carr, H. G. Evertz, A. Feiguin, J. Freire, S. Fuchs, L. Gamper, J. Gukelberger, E. Gull, S. Guertler, A. Hehn, R. Igarashi, S. V. Isakov, D. Koop, P. N. Ma, P. Mates, H. Matsuo, O. Parcollet, G. Pawłowski, J. D. Picon, L. Pollet, E. Santos, V. W. Scarola, U. Schollwöck, C. Silva, B. Surer, S. Todo, S. Trebst, M. Troyer, M. L. Wall, P. Werner, and S. Wessel: J. Stat. Mech.: Theo. Exp. (2011) P05001.
- [6] <http://alps.comp-phys.org/>.
- [7] <http://wistaria.comp-phys.org/alps-looper/>.
- [8] <http://github.com/cmsi/bcl>.
- [9] <http://github.com/wistaria/worms>.

Sixteen-beam pinhole topographs.

Kouhei OKITSU

*Institute of Engineering Innovation, University of Tokyo
2-11-16 Yayoi, Bunkyo-ku, Tokyo 113-8656*

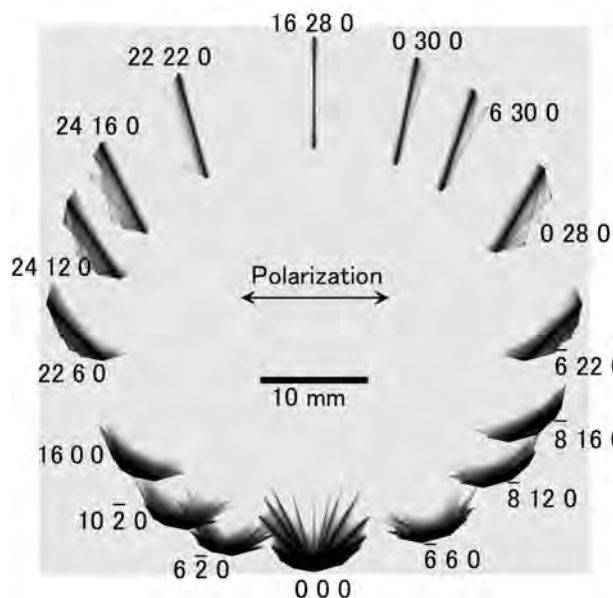


Figure 1: Computer-simulated sixteen-beam pinhole topograph images.

The present author has derived n -beam Takagi-Taupin equation that describes X-ray wavefields when n X-ray beams ($n \in \{3, 4, 5, 6, 8, 12\}$) are simultaneously strong [1, 2] and has verified it by comparing experimentally obtained pinhole topograph images and computer-simulated ones obtained by numerically solving the equation. Excellent agreements were found between them [3, 4, 5]. This equation can be applied for circular (coplanar) n -beam cases in which n reciprocal lattice nodes are on a circle in reciprocal space.

However, the author found sixteen-, eighteen- and twenty-four-beam circular cases. In this report, the author describes computer-simulated results of a sixteen-beam

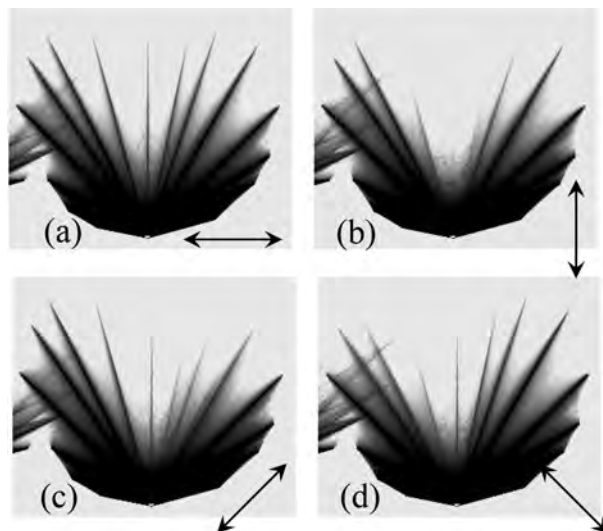


Figure 2: Enlargements of 0 0 0-forward-diffracted images for incident X-rays with (a) vertical, (b) horizontal, (c) $+45^\circ$ -inclined and (d) -45° polarizations.

case.

Figure 1 shows a computer-simulated sixteen-beam pinhole topograph. Horizontally polarized X-rays [a photon energy of 50 keV (wavelength of 0.248 Å)] whose dimension is infinitesimally small (less than 100 μm) were assumed to be incident on a perfect parallel-plate silicon crystal with a thickness of 4.8 mm. An imaging plate (IP) was assumed to be placed 18 mm behind the crystal such that the IP is parallel to the surface of the crystal.

Figure 2 shows 0 0 0-forward-diffracted images with assumptions of the incident X-rays of (a) horizontal (b) vertical (c) $+45^\circ$ -inclined and (d) -45° -inclined linear polarizations. Strong dependence of topograph images

on the polarization state of the incident X-rays is recognized.

It has been found that the Takagi-Taupin n -beam equation the present author has derived and solved [1-5] can be applicable for ‘circular n -beam cases’ of $n \in \{3, 4, 5, 6, 8, 12, 16, 18, 24\}$.

References

- [1] K. Okitsu: Acta Cryst A **59** (2003) 235-244.
- [2] K. Okitsu, Y. Yoda, Y. Imai, Y. Ueji, Y. Urano and X.-W. Zhang: Acta Cryst A **62** (2006) 237-247.
- [3] K. Okitsu, Y. Imai, Y. Ueji and Y. Yoda: Acta Cryst A **59** (2003) 311-316.
- [4] K. Okitsu, Y. Yoda, Y. Imai and Y. Ueji: Acta Cryst A **67** (2011) 557-558.
- [5] K. Okitsu, Y. Imai and Y. Yoda: In-Tech *Recent Advances in Crystallography* (2012) 67-86 [Invited].

Molecular Dynamics Simulation Study of Morphology Control Mechanism of TiO₂ Rutile Crystal by Hydroxy Acid

Hiroki NADA

*National Institute of Advanced Industrial Science and Technology (AIST),
16-1 Onogawa, Tsukuba, Ibaraki 305-8569*

A molecular dynamics simulation was conducted to elucidate the conformation and dynamics of a glycolate ion at the surface of a TiO₂ rutile crystal using massive parallel computer simulations [1]. The simulation was performed for both the {001} and {110} planes of the crystal.

The simulation suggested that the binding of the glycolate ion at the surface is more stable for the {110} system than for the {001} system. The simulation also suggested that the stable conformation of the glycolate ion near the surface was different for the two planes: the COO⁻ group of the ion was preferentially oriented toward the liquid water in the {001} system, whereas it was oriented toward the surface in the {110} system (Fig. 1). This anisotropy in the stable conformation of the glycolate ion was attributed not only to a difference in the interaction of the glycolate ion with the surface but also to a difference in the layered structure of water on the surface.

Suppose that the binding of the glycolate ion to the rutile surface hinders the growth there. Then the present simulation agrees with

the fact that the growth rate at the {001} plane becomes much larger than that at the {110} plane in the presence of glycolic acid [2]. The simulation also suggests that water is a key for elucidating the anisotropy in the conformation and dynamics of the glycolate ion and, hence, the growth shape of real rutile crystals in the presence of glycolic acid.

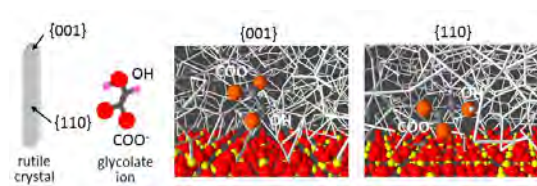


Fig. 1: Snapshots of the glycolate ion, which was stably located near the rutile surface. The white cylinders represent hydrogen bonds between water molecules. Yellow and red spheres represent Ti and O atoms, respectively.

References

- [1] H. Nada, M. Kobayashi, and M. Kakihana: *J. Phys. Chem. C* **120** (2016) 6502.
- [2] M. Kobayashi, H. Kato, and M. Kakihana: *Nanomater. Nanotechnol.* **3** (2013) 1.

Molecular Dynamics Simulation of Ferroelectrics Using a Shell Model II

T. Hashimoto

*Research Center for Computational Design of Advanced Functional Materials (CD-FMat),
National Institute of Advanced Industrial Science and Technology (AIST),
Tsukuba Central 2, 1-1-1 Umezono, Tsukuba, Ibaraki 305-8568, Japan*

BaTiO₃ is an ABO₃ type perovskite whose solid solution with other A site atoms could be a potential candidate for Pb free piezoelectric materials. BaTiO₃ undergoes phase transitions among, listing from high temperature to low temperature, cubic (C), tetragonal (T), orthorhombic (O), and rhombohedral (R) phases.

In this study, we performed molecular dynamics (MD) simulations using the shell model[1, 2]. We used a MD program developed by us. We used the smooth particle mesh Ewald method for computing the Coulomb interactions. We used a MD cell made up with 12×12×12 unit cells. The cutoff length for the nonbonded interactions were 10.0 Å. We used the adiabatic method in which the shells are given a small mass. One MD step (Δt) was 0.1 fs. The Nosé-Hoover chain method and the Parrinello-Rahman method were used for generating constant temperature and constant pressure (NPT) ensembles. The externally applied pressure was set to 0 Pa.

The piezoelectric constants were calculated by[3] $d_{kij} = \frac{1}{k_B T} \langle \Delta M_k \Delta \eta_{ij} \rangle$. Here, $\eta_{ij} = \frac{1}{2} (H_0^{t-1} G H_0^{-1} - 1)$ is the strain tensor, where $G = H^t H$ with $H = \{\mathbf{a}, \mathbf{b}, \mathbf{c}\}$ representing the MD cell, and H_0 is the reference state of H . \mathbf{M} is the total dipole moment of the MD cell. ΔX represents $X - \langle X \rangle$, where X is M_k or η_{ij} .

The temperature dependences of piezoelectric constants were similar to those obtained by the Landau-Ginzburg-Devonshire (LGD)

theory[4]. The shear and some of the longitudinal piezoelectric constants changed dramatically depending on the temperature. This arises from the temperature dependence of the dipole moment and the strain fluctuations. We also calculated the temperature dependences of the longitudinal piezoelectric surface d_{33}^* of BaTiO₃. Due to the large temperature dependence of the piezoelectric constants, the d_{33}^* surface changes significantly with temperatures as observed in the KNbO₃ study[5]. The detailed results will be published elsewhere.

References

- [1] M. Sepiarsky, S. R. Phillpot, D. Wolf, M. G. Stachiotti, and R. L. Migoni, *Appl. Phys. Lett.* **76** (2000) 3986.
- [2] T. Hashimoto and H. Moriwake, *Mol. Simul.* **41** (2015) 1074.
- [3] A. García and D. Vanderbilt, *Appl. Phys. Lett.* **72** (1998) 2981.
- [4] M. Budimir, D. Damjanovic, and N. Setter, *J. Appl. Phys.* **94** (2003) 6753.
- [5] T. Hashimoto and H. Moriwake, *J. Phys. Soc. Jpn.* **85** (2016) 034702.

Development of tensor network algorithms

Kenji HARADA

Graduate School of Informatics, Kyoto University, Kyoto 606-8501, Japan

The real-space renormalization is an important concept to study the macroscopic behavior of classical and quantum systems. Although some schemes were proposed (Ex. Migdal-Kadanoff approximation), it is hard to improve the accuracy systematically. Recently, the new type of real-space renormalization scheme appears. It is based on a singular value decomposition (SVD). In detail, it is a real-space renormalization on a tensor network. The tensor network is a mathematical framework to describe the partition function of many-body systems. For example, by a path-integral representation of the ground state in a quantum system can be regarded as a tensor network. Thus, the new real-space renormalization scheme on a tensor network has a large potential to study quantum and classical many-body problems.

Levin and Nave [1] proposed the first real-space renormalization scheme on a tensor network which is called a tensor renormalization group (TRG). SVD controls the precision in the coarse-graining step of TRG. In detail, large singular values only remain. It means that the large correlation (entanglement) part between tensors is conserved. However, Levin and Nave's scheme goes to a special structure in a coarse-grained tensor at final. It may not be an expected behavior because the structure of a coarse-grained tensor at a critical point does not have the structure of a coarse-grained tensor of TRG.

To resolve this issue of TRG, Gu and Wen [2] proposed the removing a short-scale entanglement in a coarse-grained step. Evenbly and Vidal [3] improved this idea, and they intro-

duced a new scheme which is called a tensor network renormalization (TNR). In particular, TNR numerically shows the correct structure of a tensor even at a critical point. In both algorithms, the treatment of entanglement is a key. SVD can select the important part of entanglement between two tensors. In this study, I propose the splitting of entanglement on the edge of a tensor network. The new operation can introduce flexibility in a tensor network algorithm. For example, we can do a many-body decomposition of a tensor. We can introduce a removing of a short-scale entanglement in a high-order tensor renormalization group scheme (HOTRG). We checked the structure of a coarse-grained tensor of a new HOTRG scheme numerically. It has the same structure of a coarse-grained tensor in TNR. This new operation has a potential to develop a new tensor network algorithm [4].

References

- [1] M. Levin and C. Nave, Phys. Rev. Lett. **99**, 120601 (2007).
- [2] Z. C. Gu and X.-G. Wen, Phys. Rev. B **80**, 155131 (2009).
- [3] G. Evenbly and G. Vidal, Phys. Rev. Lett. **115**, 180405 (2015).
- [4] K. Harada, in preparation.

Development of Parallelized Tensor-Network Library

Satoshi MORITA

Institute for Solid State Physics,

The University of Tokyo, Kashiwa-no-ha, Kashiwa, Chiba 277-8581

Tensor network method is one of numerical methods for quantum and classical many-body systems. To achieve highly accurate simulation for interesting problems, one needs to increase bond dimensions of tensors. However, the computational cost and the amount of memory rapidly increase with bond dimension. Therefore, we are developing parallelized library for tensor calculations [1]. Common operations appearing various tensor network methods are implemented using C++ language with hybrid parallelization (MPI + OpenMP). In our library, a tensor is stored as a matrix on distributed memory and main operations in tensor network methods, “contraction” and “decomposition”, are done by calling routines in ScaLAPACK [2]. We adopted application programming interface similar to NumPy, which is the fundamental Python package with multidimensional array. One can easily translate a Python test code into a parallel C++ code with our library.

References

- [1] <https://github.com/smorita/mptensor>
 [2] <http://www.netlib.org/scalapack/>

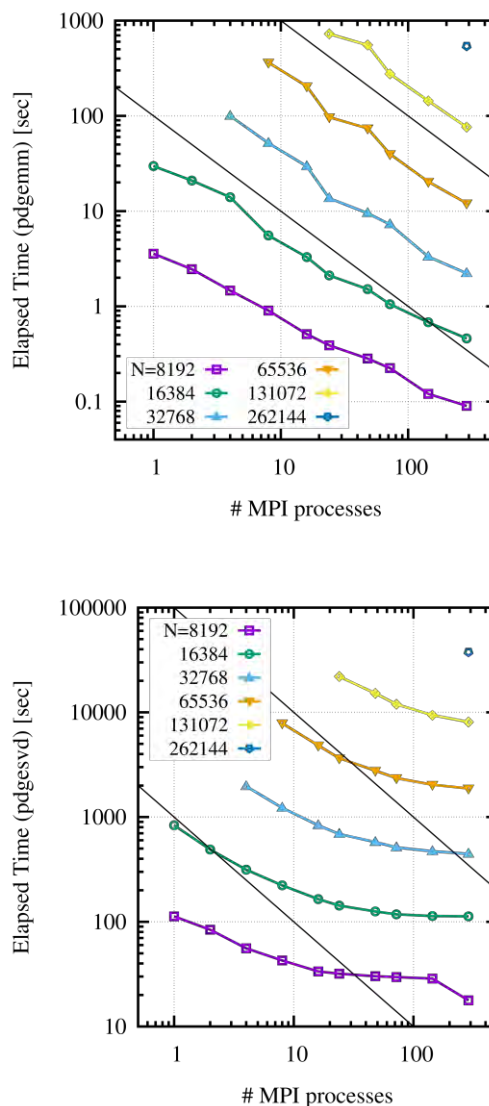


Fig. 1: Benchmark results of matrix-matrix product (top) and singular value decomposition (bottom) on the ISSP System B.

Numerical study of dynamics in Ising spin models with long-range interactions

Yusuke TOMITA

Shibaura Institute of Technology

307 Fukasaku, Minuma-ku, Saitama-City, Saitama 337-8570

Relaxational processes in ordered phases of one-dimensional (1D) Ising models with long-range interactions are investigated by $O(N)$ Monte Carlo simulations [1]. Three types of spin model, the pure ferromagnetic, the diluted ferromagnetic, and the spin glass models, are examined. Through numerical analyses of the 1D Ising model, we examined results derived from the droplet theory[2].

The Hamiltonian of the 1D Ising model with long-range interactions is given by

$$\mathcal{H} = - \sum_{i < j} \frac{J_{ij}}{r_{ij}^\sigma} S_i S_j,$$

where σ is the tuning parameter of long-range interaction. Only the nearest neighbor interactions are relevant in the limit of $\sigma \rightarrow \infty$, while all the interactions become equivalent when $\sigma = 0$. In the case of the diluted ferromagnetic model ($J_{ij} \geq 0$), the universality class depends on σ in the range of $3/2 < \sigma < 2$. In the smaller- σ region ($\sigma \leq 3/2$), the diluted systems belong to the mean-field model. The Kosterlitz-Thouless transition appears at a finite temperature at the critical point ($\sigma = 2$).

Autocorrelation functions obtained by Monte Carlo simulation exhibited the power law decay as the droplet theory declares. The autocorrelations as functions of a wave number of k and time t , $C(k; t)$, are fitted by

$$C(k; t) = C_0 \frac{\exp[-t/\tau_2(k)]}{[1 + t/\tau_1(k)]^{x(k)}} + C_\infty.$$

The parameter $\tau_1(k)$ provides an indication of the waiting time for starting the power-law decay, and the thermal relaxation time $\tau_2(k)$ indicates the relaxation time to reach the thermally equilibrium value C_∞ . Numerical data and fitting results at $\sigma = 0.8$ are shown in Fig. 1.

A marked feature of the autocorrelation functions of the diluted system is that they are placed with roughly equal intervals; the functions are approximately described by

$$C(k; t) \sim k^{-y} C(k = 2\pi/L; t),$$

where y is a constant. This means excited droplets have a fractal-like structure. The fractal-like features does not mean the system is in the Kosterlitz-Thouless phase but the correlation length is smaller than the percolation correlation-length on the diluted lattice. This pseudocritical feature is also observed in disordered ferroelectrics[3].

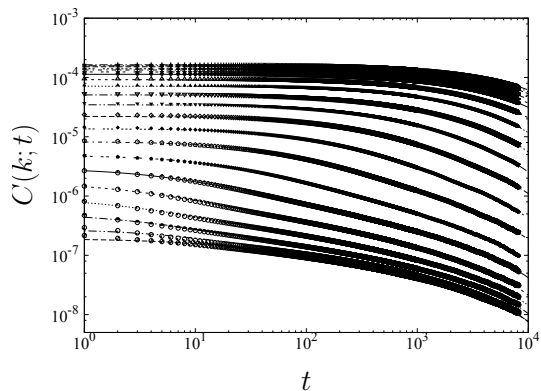


Figure 1: Autocorrelation functions of the diluted ferromagnetic model at $\sigma = 0.8$.

References

- [1] K. Fukui and S. Todo, *J. Comput. Phys.* **228**, 2629 (2009).
- [2] Y. Tomita, *Phys. Rev. E* **94**, 062142 (2016).
- [3] A. Koreeda, *et al.*, *Phys. Rev. Lett.* **109**, 197601 (2012).

Numerical study of random Dirac/Weyl electron systems

TOMI OHTSUKI¹
 TOHRU KAWARABAYASHI²
 KEITH SLEVIN³
 KOJI KOBAYASHI⁴

1) Dept. Phys., Sophia University, Chiyoda-ku, Tokyo 102-8554, Japan

2) Dept. Phys., Toho University, Miyama 2-2-1, Funabashi 274-8510, Japan

3) Dept. Phys., Osaka University, Toyonaka, Osaka 560-0043, Japan

4) IMR, Tohoku University, Sendai 980-8577, Japan

Recent discoveries of two-dimensional quantum spin Hall states and three-dimensional (3D) topological insulators (TIs) have inspired extensive research for these novel topological materials. Here we have studied disordered topological insulators as well as Weyl semimetals (WSM). We stacked N layers of two dimensional Chern insulators, and performed comparative studies of TI and WSM, which subtly depends on N , but robust against certain amount of disorder[1].

Weyl semimetal belongs to the unitary class. We have studied the 3D and 4D unitary classes Anderson transition, and obtained the critical exponents with high precision[2].

Topological insulator is realized not only in fermionic systems, but also in bosonic systems. We have shown that bosonic topological insulators are robust against disorder by analysing quantum magnon Hall effect [3].

In addition to the above works, we have demonstrated that the image recognition based on multilayer convolutional neural network (so called deep learning) works well for drawing the phase diagram of disordered topological insulators and Weyl semimetals [4,5]. See Fig. 1.

References

1. Y. Yoshimura, W. Onishi, K. Kobayashi, T. Ohtsuki, K.-I. Imura: Physical Review B **94**, 235414 (2016)
2. K. Slevin, T. Ohtsuki: Journal of the Physical Society of Japan **85**, 104712 (2016)
3. B. Xu, T. Ohtsuki, R. Shindou: Physical Review B **94**, 220403(R) (2016)

B **94**, 220403(R) (2016)

4. T. Ohtsuki, T. Ohtsuki: Journal of the Physical Society of Japan **85**, 123706 (2016)

5. T. Ohtsuki, T. Ohtsuki: Journal of the Physical Society of Japan **86**, 044708 (2017)

6. S. Liu, T. Ohtsuki, R. Shindou: Physical Review Letters **116**, 066401 (2016)

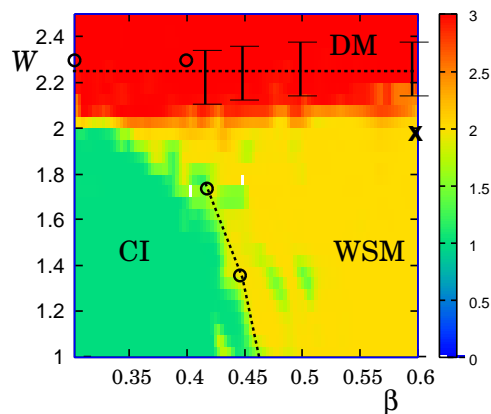


Figure 1: Color map of P_{CI} , P_{WSM} , and P_{DM} , which are probabilities that the eigenfunctions are judged to belong to the Chern insulator, Weyl semimetal and diffusive metal phases, respectively. The intensity $1 \times P_{CI} + 2 \times P_{WSM} + 3 \times P_{DM}$ is plotted. Bars with errors and circles (\circ) indicate the transfer matrix estimate of the critical points[6], and dotted lines are a guide to the eye. The cross (\times) at $(\beta, W) \approx (0.6, 2.0)$ indicates the WSM/DM phase boundary estimated by the scaling of density of states. Taken from [5].

Simulation studies of (i) the significant difference in the dynamics between strong and fragile liquids and (ii) shear thinning in glassy liquids

Akira Furukawa

*Institute of Industrial Science, University of Tokyo
Komaba 4-6-1, Meguro-ku, Tokyo 153-8505*

(i) We revealed a significant difference in the dynamics between these two types of glass formers through molecular dynamics simulations [1]: In strong glass formers, the relaxation dynamics of density fluctuations is nondiffusive, whereas in fragile glass formers it exhibits diffusive behavior. We demonstrate that this distinction is a direct consequence of the fundamental difference in the underlying elementary relaxation process between these two dynamical classes of glass formers. For fragile glass formers, a density-exchange process proceeds the density relaxation, which takes place locally at the particle level in normal states but is increasingly cooperative and nonlocal as the temperature is lowered in supercooled states. On the other hand, in strong glass formers, such an exchange process is not necessary for density relaxation due to the presence of other local relaxation channels. Our finding provides a novel insight into Angell's classification scheme from a hydrodynamic perspective.

(ii) We proposed a simple mechanism for describing the onset of shear thinning in a high-density glassy liquid: In a shear flow, along the compression axis, the overlap between neighboring particles is more enhanced than that at equilibrium, meaning that the effective size is reduced along this axis. On the other hand, along the extension axis perpendicular to the compression axis, the average structural con-

figurations are stretched, but it does not indicate the expansion of the effective size itself. This asymmetric shear flow effect for particles results in a small reduction of the effective density. Because, in glass-forming liquids, the structural relaxation time strongly depends on the density, even a very small reduction of the effective density should lead to a significant decrease of the relaxation time under shear flow. We predict that the crossover shear rate from Newtonian to non-Newtonian flow behaviors is given by $\dot{\gamma}_c = [\rho(\partial\tau_\alpha/\partial\rho)]^{-1}$, which can be much smaller than $1/\tau_\alpha$ near the glass transition point. It is shown that this prediction is consistent with the results of molecular dynamics simulations.

These simulations (i) and (ii) were partially performed at the ISSP Supercomputer Center. The programs are parallelized with a combination of OpenMP and MPI techniques.

References

- [1] A. Furukawa and H. Tanaka, *Phys. Rev. E*, **94**, 052607 (2016).
- [2] A. Furukawa, *Phys. Rev. E*, **95**, 012613 (2017).

Heat Transfer Characteristics of Condensate Film Flow along Vertical Plates with Microscopic Grooves

Takahiro ADACHI

*Department of Mechanical Engineering, Akita University
Tegata-Gakuen 1-1, Akita, Akita 010-8502*

The characteristics of thin, falling liquid films due to condensation along a vertical plate have been of interest to engineers, for example, in plate-type absorber, plate-type condenser and so on. In order to enhance the heat transfer, fluted parts along the streamwise direction have been established on the plate. This is because the liquid film spreads as thinly as possible over the plate surface since strong surface tension aids in the removal of film from the top to bottom of the fluted parts, thereby producing a very thin liquid film. This is called a drainage effect[1].

On the other hand, little research was done on the film flow along a plate with a grooved part setting perpendicular to the streamwise direction due to some mathematical difficulties. Therefore, our objective in this study is to clarify how the grooved part affects the flow patterns and heat transfer.

We consider a liquid film flow along a plate with a rectangular groove setting perpendicular to the stream-wise direction on its surface. Figure 1 shows a geometry of the problem and the coordinate system. The x -axis is taken to be parallel to the vertical direction and the y -axis to be perpendicular to it. Nondimensional parameters to characterize the plate configuration, height h of the groove, width of the groove w_b , inlet length w_i and outlet length w_o are, using δ_0^* at the inlet as a characteristic length, defined as

$$h = \frac{h^*}{\delta_0^*}, \quad w_b = \frac{w_b^*}{\delta_0^*}, \quad w_i = \frac{w_i^*}{\delta_0^*}, \quad w_o = \frac{w_o^*}{\delta_0^*} \quad (1)$$

where we represent physical quantities with their dimensions by attaching a superscript * to them, and the total plate length is $L =$

$w_i + w_b + w_o$. The characteristic length δ_0^* can be derived from Nusselt's film theory such as

$$\delta_0^* = \left(\frac{3\nu_l^* Q^*}{g^*} \right)^{1/3}, \quad (2)$$

where ν_l^* , g^* and Q^* are dynamic viscosity of the fluid, gravitational acceleration and flow rate, respectively.

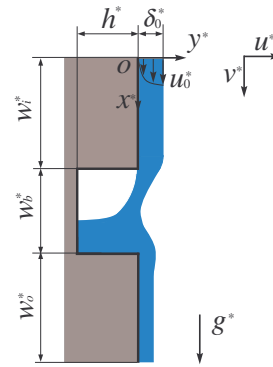


Fig.1 Geometry and coordinates.

We assume that the flow is two-dimensional because the film flow is thin and the depth in the spanwise direction of plate is large enough. Moreover, the fluid is assumed to be incompressible and the shear stress from the gas phase side can be negligible. Then we make non-dimensional the following quantities, by using characteristic length δ_0^* and surface velocity at the reference point as $u_0^* = \rho_l^* g^* \delta_0^{*2} / (2\mu_l^*)$ which is also derive from Nusselt's film theory, as

$$\mathbf{x} = \frac{\mathbf{x}}{\delta_0^*}, \quad \mathbf{u} = \frac{\mathbf{u}}{u_0^*}, \quad t = \frac{t^* u_0^*}{\delta_0^*}, \quad p = \frac{p^*}{\rho_l^* u_0^{*2}},$$

$$\rho = \frac{\rho^*}{\rho_l^*}, \quad \mu = \frac{\mu^*}{\mu_l^*}. \quad (3)$$

This time, we proceed our calculations not only for liquid phase but also for gas phase. Then, the governing equations for the velocities and pressure are written in non-dimensional forms as

$$\nabla \cdot \mathbf{u} = 0, \quad (4)$$

$$\rho \left\{ \frac{\partial \mathbf{u}}{\partial t} + (\mathbf{u} \cdot \nabla) \mathbf{u} \right\} = \rho Fr e_x - \nabla p - \frac{Fr}{Bo} \kappa \nabla H + \frac{1}{Re} \nabla \left[\mu \{ \nabla \cdot \mathbf{u} + (\nabla \cdot \mathbf{u})^T \} \right], \quad (5)$$

Nondimensional parameters in the equations are the Reynolds number, Flude number and Bond number respectively defined as

$$Re = \frac{u_0^* \delta_0^*}{\nu^*}, \quad Fr = \frac{\delta_0^* g^*}{u_0^{*2}}, \quad Bo = \frac{\delta_0^{*2} \rho^* g^*}{\sigma^*}. \quad (6)$$

First, we solve the governing equations Eq. (4) and (5) for velocity and pressure fields numerically by Highly Simplified Marker and Cell (HSMAC) method using staggered grid system. In addition to HSMAC method for the velocity and pressure fields, we have used a Coupled Level-Set and Volume Of Fluid (CLSVOF) method[2,3] to determine the free surface between gas and liquid phases, wehre we have been dealing with a new approach to impose surface tension effect and discontinuous changes of physical quantities between liquid and gas phases. Namely, Ghost Fluid Method(GFM)[4] are examined as well as CLSVOF Mmethod in our program.

Before, we used CSF(Continuum Surface Force) model proposed by Brackbill et al.[5] in order to express the surface tension effect. In such model, a continuous Heaviside function was used. However in this study, we have used a discontinuous Heaviside function in the Ghost Fluid method defined as

$$\begin{aligned} H(\phi) &= 1, & \text{if } \phi \geq 0, \\ &= 0, & \text{if } \phi \leq 0. \end{aligned} \quad (7)$$

Therefore, we can express the discontinuous changes of density and viscosity between the liquid and gas phased as

$$\rho = \frac{\rho_g^*}{\rho_l^*} (1 - H(\phi)) + H(\phi), \quad (8)$$

$$\mu = \frac{\mu_g^*}{\mu_l^*} (1 - H(\phi)) + H(\phi). \quad (9)$$

This leads to the more realistic calculation results in our study.

1 Results

In this year, we try to calculate the evaporation heat transfer. The treatment for evaporation is the same for condensation, because the direction of the heat flux is different. Figure 2 is the result of film evaporation along the vertical smoothe plate. We can see in the figure that the evaporation bulles are separate from the plate as shown in Fig. 2(a), and the temperature distribution in Fig. 2(b). However, the treatment of evaporation and condensation is basically very difficult, because iteration process in HSMAC spends much time of about 80% to total time in our code. So we are now trying to parallelize the part by using MPI.

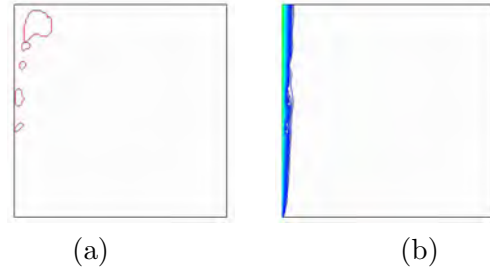


Fig.2 Evaporation bubbles and temperature distribution.

References

- [1] R. Gregorig, Z. Angew. Math. Phys., Vol. 5, (1954) 36.
- [2] M. Sussman, E. G. Puckett. J. Comput. Phys., Vol. 162, (200) 301.
- [3] G. Son, and N, Hur. Numer. Heat Transf., Part B, Vol. 42, (2002) 523.
- [4] G. Son, and V. K. Dhir. Numer. Heat Transf., PArt B, Vol. 52, (2007) 153.
- [5] U. J. Brackbill, D. B. Kothe, and C. Zemach. J. Comput. Phys., Vol. 100, (1992) 335.

Cell Crowding Effects in Collective Cell Migration

Katsuyoshi Matsushita

Department of Biological Science, Osaka University

Machikaneyama-cho, Toyonaka 560-0043

The collective cell migration contributes to various biological phenomena including morphogenesis of organs, wound healing, and immune response. Therefore, the clarification of its mechanism is a key to understandings of these phenomena. To clarify the mechanism, much effort has been devoted. In particular, they have been intensively investigated on the basis of statistical physics models. In spite of a large amount of effort, the understanding of the mechanism is not sufficiently achieved because of the complexity and diversity of biological systems.

A possible mechanism is the mechanism based on collective motions of soft active colloid systems [1]. It is well known that soft active colloids spontaneously exhibit collective motion for a large volume fraction of colloids. This is regarded as a crowding effect of soft active colloids. The crowding mechanism may be a possible mechanism of collective cell migration.

The soft active colloids behave as a self-propelled particle. In contrast, in various collective cell migrations, movement using highly random deformations of cells, so-called amoeboid motion, are frequently observed. Because of this difference in motion, the crowding mechanism of soft active colloids is not simply applied to collective cell migration.

To show the applicability of this crowding mechanism to the collective cell migration associated with amoeboid cells, we utilize a variant of the cellular Potts model in which amoeboid cells repulsively interact with each other and have a motility [2, 3]. We simulate the

migration of amoeboid cells with sweeping the number of cells and calculate the order parameter of cell motility M . Here, when M is close to unity, the cells exhibit a collective motion and otherwise do not exhibit it. The data of M is plotted as a function of volume fraction ϕ in Fig. 1. M rapidly increases with ϕ at a threshold volume fraction $\phi = \phi_C$ and gets close to unity at large volume fractions. Therefore, the crowding mechanism is concluded to be applicable to the collective cell migration of amoeboid cells.

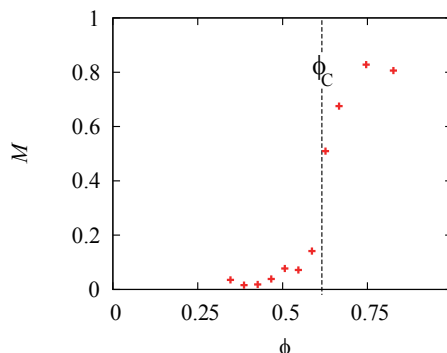


Figure 1: The order parameter of cell motility M as a function of volume fraction.

References

- [1] T. Hanke, C. A. Weber, and E. Frey: *Phys. Rev. E* **88** 570 (2013).
- [2] K. Matsushita, *Phys. Rev. E* **95**, 032415 (2017).
- [3] K. Matsushita, *Proc. Sympo. Simul. Traffic Flow* **21**, 19 (2015).

Ground-State Phase Diagram of a Frustrated $S=1/2$ Two-Leg Ladder with Different Leg Interactions

Takashi Tonegawa

Professor Emeritus, Kobe Univ. and Visiting Professor, Osaka Prefecture Univ.

This report aims at exploring the ground-state phase diagram of an anisotropic $S=1/2$ two-leg ladder with different leg interactions by using mainly numerical methods. We express the Hamiltonian which describes this system as

$$\begin{aligned} \mathcal{H} = & J_{\text{leg},a} \sum_{j=1}^L \vec{S}_{j,a} \cdot \vec{S}_{j+1,a} \\ & + J_{\text{leg},b} \sum_{j=1}^L \vec{S}_{j,b} \cdot \vec{S}_{j+1,b} \\ & + J_{\text{rung}} \sum_{j=1}^L [\vec{S}_{j,a}, \vec{S}_{j,b}]_{\Gamma} \end{aligned} \quad (1)$$

with

$$[\vec{S}_{j,a}, \vec{S}_{j,b}]_{\Gamma} \equiv \Gamma \{ S_{j,a}^x S_{j,b}^x + S_{j,a}^y S_{j,b}^y \} + S_{j,a}^z S_{j,b}^z. \quad (2)$$

Here, $\vec{S}_{j,\ell} = (S_{j,\ell}^x, S_{j,\ell}^y, S_{j,\ell}^z)$ is the $S=1/2$ operator acting at the (j, ℓ) site assigned by rung j and leg ℓ ($= a$ or b); $J_{\text{leg},a}$ and $J_{\text{leg},b}$ denote, respectively, the magnitudes of the isotropic leg a and leg b interactions; J_{rung} denotes that of the anisotropic rung interaction, the XXZ -type anisotropy being controlled by the parameter Γ ; L is the total number of rungs, which is assumed to be even. It should be noted that this system has a frustration when $J_{\text{leg},a} J_{\text{leg},b} < 0$ irrespective of the sign of J_{rung} . Throughout this report, we assume that $J_{\text{rung}} = -1.0$ (the rung interaction is ferromagnetic), choosing $|J_{\text{rung}}|$ as the unit of energy, and also that $J_{\text{leg},a} = 0.2$.

We [1] have already determined numerically the ground-state phase diagram on the $1/\Gamma$ versus $J_{\text{leg},b}$ plane in the case where the anisotropy of the rung interaction is assumed to be of the XY -type ($\Gamma > 1.0$). This phase diagram consists of the Haldane, triplet-dimer, $XY1$ and non-collinear ferrimagnetic (NCFR) [2] phases. In this report, we confine ourselves to the case where the anisotropy of the rung interaction is of the Ising-type ($0.0 \leq \Gamma \leq 1.0$). The motivation of treating this case is as follows. When the ferromagnetic rung interaction with Ising-type anisotropy is much stronger than both of two kinds of leg interactions, a pair of $S=1/2$ spins at each rung forms a bound state of two magnons. This may lead, in the frustrated region, to the nematic Tomonaga-Luttinger

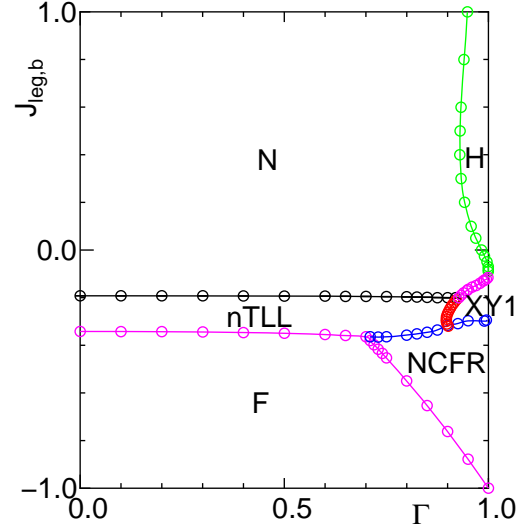


Figure 1: Ground-state phase diagram on the Γ versus $J_{\text{leg},b}$ plane for $J_{\text{rung}} = -1$ and $J_{\text{leg},a} = 0.2$. The regions designated by N, H, nTLL, XY1, F and NCFR are, respectively, those of the Néel, Haldane, nematic TLL, XY1, ferromagnetic and non-collinear ferrimagnetic phases.

liquid (TLL) state, which has been extensively investigated in recent years.

Figure 1 shows our final result for the ground-state phase diagram on the Γ versus $J_{\text{leg},b}$ plane. In this phase diagram six states, that is, the Néel (N), Haldane (H), nematic TLL (nTLL), $XY1$, ferromagnetic (F) and NCFR states, appear as the ground states. It should be emphasized that, as is expected, the nTLL state becomes the ground state in the strong-rung frustrated region.

At this junction, we denote, respectively, by $E_0(L, M; \text{pbc})$ and $E_1(L, M; \text{pbc})$ the lowest and first excited energies within the subspace of the Hamiltonian (1) determined by L and M under periodic boundary conditions, where M is the total magnetization which is a good quantum number with the eigenvalues of $M = 0, \pm 1, \dots, \pm L$. We have numerically calculated these energies for finite-size systems with up to $2L = 28$ spins by means of the exact-diagonalization (ED) method.

The ground-state energy $E_g(L)$ is given by the minimum value among $E_0(L, 0; \text{pbc})$, $E_0(L, \pm 1; \text{pbc})$, \dots , $E_0(L, \pm L; \text{pbc})$, and the ground-state magnetization $M_g(L)$ is the value of M giving $E_g(L)$. It is noted that $M_g(L) = 0$ in the N, H, nTLL and XY1 states, $0 < M_g(L) < L$ in the NCFR state, and $M_g(L) = L$ in the F state. Furthermore, we introduce the following three excitation energies:

$$\Delta_{00}^{(p)}(L) = E_1(L, 0; \text{pbc}) - E_0(L, 0; \text{pbc}), \quad (3)$$

$$\Delta_{10}^{(p)}(L) = E_0(L, 1; \text{pbc}) - E_0(L, 0; \text{pbc}), \quad (4)$$

$$\Delta_{20}^{(p)}(L) = E_0(L, 2; \text{pbc}) - E_0(L, 0; \text{pbc}). \quad (5)$$

Let us now discuss how to numerically determine the phase boundary lines shown in Fig. 1. In the following way, we estimate the finite-size critical values of $J_{\text{leg},b}$ (or Γ) for various values of Γ (or $J_{\text{leg},b}$), for each phase transition. Then, the phase boundary line for the transition is obtained by connecting the results for the $L \rightarrow \infty$ extrapolation of the finite-size critical values.

Firstly, we employ the level spectroscopy method [3] to estimate the phase boundary lines between two of the N, XY1 and nTLL phases. According to this method, the three quantities, $\Delta_{00}^{(p)}(L)$, $\Delta_{10}^{(p)}(L)$ and $\Delta_{20}^{(p)}(L)/2$, should be compared in the $L \rightarrow \infty$ limit; the ground state is the N, XY1 or nTLL state depending upon whether $\Delta_{00}^{(p)}(L)$, $\Delta_{10}^{(p)}(L)$ or $\Delta_{20}^{(p)}(L)/2$ is lowest among them. Thus, the finite-size critical values for the N-XY1, N-nTLL, and XY1-nTLL transitions can be evaluated by solving the equations,

$$\Delta_{00}^{(p)}(L) = \Delta_{10}^{(p)}(L) < \Delta_{20}^{(p)}(L)/2, \quad (6)$$

$$\Delta_{00}^{(p)}(L) = \Delta_{20}^{(p)}(L)/2 < \Delta_{10}^{(p)}(L), \quad (7)$$

$$\Delta_{10}^{(p)}(L) = \Delta_{20}^{(p)}(L)/2 < \Delta_{00}^{(p)}(L). \quad (8)$$

respectively. It is noted that the tricritical point for the N, XY1 and nTLL phases is given by $(\Gamma, J_{\text{leg},b}) = (0.927 \pm 0.001, -0.200 \pm 0.001)$, at which $\Delta_{00}^{(p)}(L) = \Delta_{10}^{(p)}(L) = \Delta_{20}^{(p)}(L)/2$ holds in the limit of $L \rightarrow \infty$.

Secondly, the phase transition between the H and N phase is the 2D Ising-type transition. Therefore, the phase boundary line between these two phases can be estimated by the phenomenological renormalization group (PRG) method [4]. That is to say, we numerically solve the PRG equation,

$$L\Delta_{00}^{(p)}(L) = (L+2)\Delta_{00}^{(p)}(L+2), \quad (9)$$

to calculate the finite-size critical values.

Thirdly, it is apparent that the finite-size critical values of the phase transition between the F and nTLL phases are estimated from the equation,

$$E_0(L, L; \text{pbc}) = E_0(L, 0; \text{pbc}), \quad (10)$$

because $M_g(L) = L$ and $M_g(L) = 0$ in the F and nTLL states, respectively.

Finally, we discuss the phase transition between the F and NCFR phases and that between the NCFR and XY1 (or nTLL) phases. The results of the ED calculation show that the former transition is of the second order, that is, it is the transition between the $M=L$ and $M=L-1$ states. Thus, the finite-size critical values can be estimated from

$$E_0(L, L; \text{pbc}) = E_0(L, L-1; \text{pbc}). \quad (11)$$

The obtained finite-size critical values are naturally independent of L ; as is well known, we can derive the analytic formula for them by analyzing the spin-wave dispersion relation. On the other hand, the latter transition is of the first order, that is, it is the transition between the $M > 1$ and $M = 0$ states. In order to determine the phase transition line of this transition, we have carried out the density-matrix renormalization-group [5] calculations for the system with $2L = 72$ spins to estimate $M_g(L)$ for various values of $J_{\text{leg},b}$ with Γ fixed at several values. We suppose that the phase transition line obtained in the $2L = 72$ system gives good approximate result at the $L \rightarrow \infty$ limit. (See our recent paper [1] for more details.)

This work has been done in collaboration with T. Hikihara, K. Okamoto and T. Sakai.

[1] T. Tonegawa, K. Okamoto, T. Hikihara and T. Sakai: *J. Phys.: Conf. Series* **828** (2017) 012003.

[2] M. Tsukano and M. Takahashi: *J. Phys. Soc. Jpn.* **66** (1997) 1153; S. Yoshikawa and S. Miyashita: *J. Phys. Soc. Jpn.* **74** (2005) Suppl. 71.
[3] K. Okamoto and K. Nomura: *Phys. Lett. A* **169** (1992) 433; K. Nomura and K. Okamoto: *J. Phys. A* **27** (1994) 5773.

[4] M. P. Nightingale: *Physica A* **83** (1976) 561.

[5] S. R. White: *Phys. Rev. Lett.* **69** (1992) 2863; *Phys. Rev. B* **48** (1993) 10345.

Randomness Effects on Quantum Spin Systems Coupled to Lattice Degrees of Freedom

Chitoshi YASUDA and Shouta MIYARA

*Department of Physics and Earth Sciences, Faculty of Science,
University of the Ryukyus, Nishihara, Okinawa 903-0213, Japan*

Since the inorganic compound CuGeO_3 was synthesized, randomness effects of the spin-Peierls (SP) system have attracted considerable attention. When nonmagnetic impurities are doped in the SP compound, an antiferromagnetic long-range order (AFLRO) is induced. The mechanism is understood by magnetic moments induced near the impurities, which are called ‘effective spins’. By substituting nonmagnetic atoms for magnetic atoms, effective spins are induced near the nonmagnetic atoms. Since the effective spins interact through a sea of spin-singlet pairs, the AFLRO is induced [1]. However, an experimental result contradictory to this interpretation was reported: the effective spins are not induced near diluted sites [2]. We need to take lattice degrees of freedom into account in order to investigate positions of the effective spins.

In this project, we investigated the spin-1/2 antiferromagnetic Heisenberg (AFH) model coupled to lattice degrees of freedom. Previous researches on the two-dimensional site-diluted AFH systems have concluded that effective spins are induced near diluted sites at low temperature. However, the experimental result of the SP compound described by the AFH model showed that there is no effective spin near impurities as mentioned above. Thus, in the present work, we examined what kind of situation is the case that the effective spins are not induced near diluted sites, and investigated whether the AFLRO is actually induced or not. The method is the quantum Monte Carlo (QMC) simulation with the continuous-imaginary-time loop algorithm and the program is based

on ‘Looper’ developed by S. Todo *et al* [3]. Since this QMC simulation is suitable to parallel computing, we mainly performed parallel computing with MPI.

At first, assuming two patterns of lattice distortion such that effective spins are induced near diluted sites or not, we compared two ground-state energies. As the result, we found that the effective spins are hard to be induced near diluted sites for the large elastic constant, small interchain interaction, and large concentration of dilution.

Next, we performed self-consistent calculations of lattice-distortion patterns for the one-dimensional finite chains and found that the lattice distortion is described by a hyperbolic tangent function and that soliton-type magnetic moments are induced at the places other than edges. Furthermore, we investigated site-dilution effects in the two-dimensional system consisting of the one-dimensional chains connected by the spin-spin interaction. As the result, the AFLRO was induced. In this calculation, the temperature regarded as zero temperature is lower than that of the site-diluted bond-alternated system. This problem of the large-scale computation becomes serious when the interchain interaction is small.

References

- [1] C. Yasuda, *et al.*: Phys. Rev. B **64**, 092405 (2001); J. Phys. Soc. Jpn. **75**, 124704 (2006).
- [2] J. Kikuchi, *et al.*: Phys. Rev. Lett. **88**, 037603 (2002).
- [3] S. Todo and K. Kato, Phys. Rev. Lett. **87**, 047203 (2001).

Shape Optimization in Conjugate Heat Transfer Problems

Kenichi MORIMOTO

Department of Mechanical Engineering,

The University of Tokyo, 7-3-1 Hongo, Bunkyo-ku, Tokyo 113-8656

We have developed an adjoint-based shape-optimization scheme under the conjugate condition with thermal coupling between the solidified liquid and the solid wall. In order to consider practical applications, we examined the effect of the wall thermal conductivity on the shape optimization, and the regularization effect due to the wall heat conduction. In Ref. [1], in order to develop an adjoint analysis-based shape optimization method for convective boundary-layer flows with complex heat transfer surfaces, as the first step, we have increased the node density of the meshless analyses using parallel computing. A series of numerical simulations of the present shape optimization has been performed using in-house code for broader ranges of the thermo-physical properties. Also, we proposed a new strategy for efficient scheme for dealing with boundary-layer flows.

High-performance turbulent heat exchangers are demanded for energy-saving purposes in various engineering fields such as in automobile industry. Over the past several decades, remarkable advances have been made in the adjoint-based shape optimization methods, but no application to turbulent heat

and fluid flow problems has been reported so far. We previously demonstrated the effectiveness of the adjoint-based analysis on the optimization of convective heat transfer problem in the laminar-flow regime. We established a RANS-based adjoint analysis approach (using OpenFOAM) for shape optimization in turbulent heat transfer problems [2].

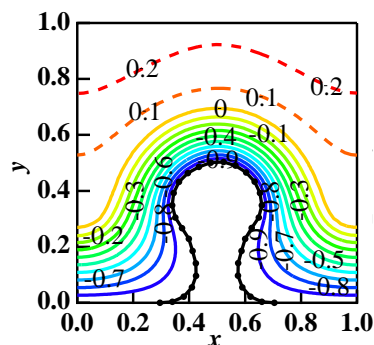


Fig. 1: Meshless computation-based shape optimization.

References

- [1] H. Kinoshita, Y. Suzuki, and K. Morimoto, Proc. 9th JSME-KSME Thermal Fluids Eng. Conf. (TFEC9), Oct. 2017 (accepted).
- [2] K. Morimoto, Y. Goto and Y. Suzuki, Proc. 9th JSME-KSME Thermal Fluids Eng. Conf. (TFEC9), Oct. 2017 (accepted).

Structural dynamics of an aldehyde-deformylating oxygenase studied by molecular dynamics simulations

Yuma SUEMATSU and Munehito ARAI

*Department of Life Sciences, Graduate School of Arts and Sciences,
The University of Tokyo, Komaba, Meguro, Tokyo 153-8902*

Cyanobacteria are known to synthesize alkanes/alkenes corresponding to diesel oils. Because these hydrocarbons are produced from carbon dioxide by photosynthesis, such “bio-energies” are expected to be substitutes for petroleum-based hydrocarbons [1]. In 2010, Schirmer *et al.* revealed that cyanobacteria use two enzymes for two-step production of hydrocarbons from fatty acyl-(acyl carrier protein (ACP)) [2]. In the first step, an acyl-ACP reductase (AAR) reduces acyl-ACP into aldehydes. Then, in the second step, an aldehyde-deformylating oxygenase (ADO) converts aldehydes into alkanes/alkenes. However, ADO has extremely low activity, and its catalytic mechanism has been poorly understood. In general, proteins exert their functions through dynamic motions, and thus, elucidation of structural dynamics of ADO is necessary for understanding the mechanism of the ADO action and improving its catalytic activity.

Here, we performed molecular dynamics (MD) simulations of the ADO protein from *Nostoc punctiforme* PCC 73102. Because ADO

is known to bind two metal ions, we performed MD simulations both in the presence and absence of metal ions. In addition, we did simulations in the presence and absence of an alkane molecule, resulting in four types of MD simulations. The crystal structure of the protein was used as an initial structure of simulations.

We found by simulations that the N-terminal region of ADO forms helical structures and interacts with the regions for the substrate entry. Moreover, the simulations suggest that the dynamics of N- and C-terminal regions control the substrate entry. We propose that low activity of ADO is attributed to slow entry of a substrate and slow exit of a product, and changing the dynamics of ADO by mutations at the N-terminal region may improve the catalytic activity of ADO.

References

- [1] H. Kudo, R. Nawa, Y. Hayashi, and M. Arai: *Biotechnology for Biofuels*, **9** (2016) 234.
- [2] A. Schirmer, M.A. Rude X. Li, E. Popova, and S.B. del Cardayre: *Science*, **329** (2010) 559-562.

Designing Kitaev spin liquids in metal-organic frameworks

Masahiko G. YAMADA, Hiroyuki Fujita, and Masaki OSHIKAWA

Institute for Solid State Physics, University of Tokyo

Kashiwa-no-ha, Kashiwa, Chiba 277-8581

We have studied the possibility to design Kitaev models in real materials. The ground state of the Kitaev model on the honeycomb lattice is a particular type of spin liquid (called Kitaev spin liquid). Conventional candidate materials, iridates and α - RuCl_3 , have substantial non-Kitaev direct exchange interactions and show magnetic ordering at lower temperature. We propose metal-organic frameworks (MOFs) with Ru^{3+} (or Os^{3+}) forming the honeycomb lattice as new candidates for an ideal realization of the Kitaev model, where the problematic direct exchange interaction can be suppressed. In order to show the suppression of the non-Kitaev interactions, we used a first-principles electronic structure calculation code called OPENMX [1] for the molecular structure of the organic ligands in the proposed MOFs. Although the calculation was a simple one for the molecular orbitals, we used the ISSP supercomputer to speed up the material explorations. From this calculation, we proved the degeneracy of the highest occupied molecular orbitals of the organic ligands in this class of materials, which implies a strong suppression of non-Kitaev interactions. We have estimated the parameters of the spin interactions in MOFs with oxalate-based (or tetraaminopyrazine-based) ligands, and have shown that they are promising candidates to realize Kitaev spin liquids. The great flexibility of MOFs allows generalization to other three-dimensional lattices or heterogeneous structures, for potential realization of

various new spin liquids, such as a gapless Weyl spin liquid and a gapped Z2 spin liquid. The details of our work are reported in Ref. [2].

References

- [1] T. Ozaki: Phys. Rev. B **67**, (2003) 155108.
- [2] M. G. Yamada, H. Fujita, and M. Oshikawa: arXiv:1605.04471 [cond-mat.str-el] (2016).

Microscopic analysis of the Hall effect in superconductors using the augmented quasiclassical equations with the Lorentz force

Takafumi KITA

Department of Physics, Hokkaido University

Sapporo 060-0810, Japan

After the sign change of the Hall conductivity have been observed in some high- T_c superconductors, intensive studies have been performed on *the flux-flow Hall effect* in type-II superconductors theoretically and experimentally. Despite these efforts, a microscopic understanding of the anomalous flux-flow Hall effect is still missing. This may be because the Lorentz force is missing from the standard Eilenberger equations and Ginzburg–Landau equation. In fact, the standard equations cannot describe the Hall effect in superconductors.

Recently, the Lorentz force has been incorporated successfully in a gauge-invariant manner within the real-time Keldysh formalism [1]. The augmented quasiclassical equations in the Keldysh formalism have been used to study charging in the Meissner state with Fermi-surface and gap anisotropies [2], and also to calculate flux-flow Hall conductivity numerically for the s -wave pairing on an isotropic Fermi surface [3]. However, the temperature dependence of the Hall conductivity have not been calculated in Ref. [3].

The flux-flow Hall effect denotes a dissipative nonequilibrium phenomena accompanying motions of vortices and the resulting electric field. It is much more difficult to investigate than the equilibrium Hall effect in superconductors or the Hall effect in metals and semiconductors due to the presences of the spatial inhomogeneity and vortex motion. Hence, it is not surprising to know that a fully microscopic

study on the flux-flow Hall effect was started only quite recently by Arahata and Kato [3] for an isolated vortex in an s -wave superconductor.

On the other hand, we derived augmented quasiclassical equations of superconductivity with the Lorentz force in the Matsubara formalism so that the charge redistribution due to supercurrent can be calculated quantitatively [4]. It is still desirable when studying the charging to transform the equations into the Matsubara formalism, in which equilibrium properties and linear responses can be calculated much more easily.

We study the flux-flow Hall effect in a superconductor with an isolated vortex based on the augmented quasiclassical equations of the superconductivity with the Lorentz force [1]. In particular, we calculate the temperature dependence of the Hall angle for electric field induced by a motion of an isolated vortex by transforming the energy variable of the augmented quasiclassical equations in the Keldysh formalism into the Matsubara energy on the imaginary axis. The Hall angle is defined as $\tan \theta_H \equiv \langle E_H \rangle / \langle E_O \rangle$, where $\langle \dots \rangle$ denotes the spatial average, E_O is the longitudinal electric field and E_H is the Hall electric field. It is shown that linear responses can be calculated much more easily compared to the approach based on the augmented quasiclassical equations in the Keldysh formalism.

We consider the linear response $\check{g} = \check{g}^{\text{eq}} + \delta\check{g}$

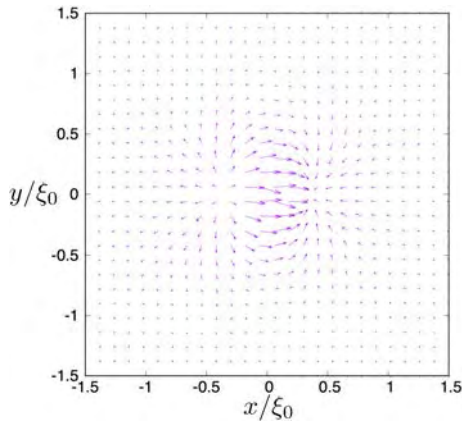


Figure 1: Longitudinal electric field \mathbf{E}_O over $-1.5\xi_0 \leq x, y \leq 1.5\xi_0$ at $T/T_c = 0.4$.

to a spatially uniform but time-dependent perturbation $\delta \mathbf{A}^{\text{ex}} e^{-i\omega t} = \delta \mathbf{E}^{\text{ex}} e^{-i\omega t} / i\omega$ with frequency ω [5]. The limit $\omega \rightarrow 0$ will be taken eventually. As shown in Refs. [2, 4], we expand Green's functions in the quasiclassical parameter $\delta \equiv 1/k_F \xi_0$ (ξ_0 : the coherence length). With these preliminaries, we solve the augmented quasiclassical equations of superconductivity with the Lorentz force, the gap equation, and Maxwell equations simultaneously in a self-consistent way. We obtain the longitudinal and Hall electric field induced by the vortex motion numerically by standard Runge–Kutta methods.

Figures 1 and 2 plot the longitudinal and Hall electric field induced by the vortex motion in the core region at $T/T_c = 0.4$, respectively. They clearly show the existence of the ohmic and Hall resistivity in the flux-flow state. Figure 3 plots the Hall angle as a function of temperature. We observe the decreasing the Hall angle as the temperature is increased from $T = 0$.

We have also developed a new approach to calculate the linear responses in the flux-flow state by transforming the energy variable of the augmented quasiclassical equations in the Keldysh formalism into the Matsubara energy on the imaginary axis. Using it, we confirmed that there exists the ohmic and Hall resistiv-

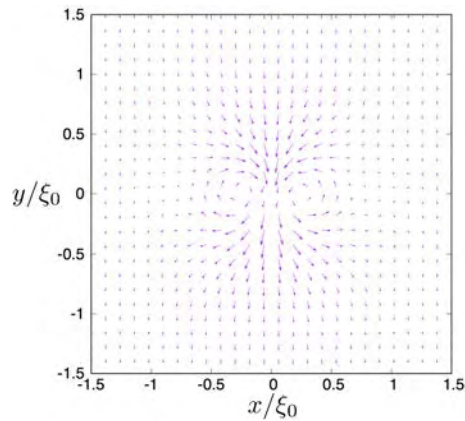


Figure 2: Hall electric field \mathbf{E}_H over $-1.5\xi_0 \leq x, y \leq 1.5\xi_0$ at $T/T_c = 0.4$.

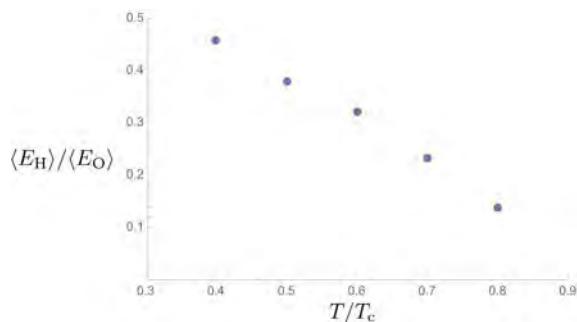


Figure 3: Hall angle $\tan \theta_H$ as a function of temperature.

ities caused by the moving isolated vortex in an s -wave superconductor, and obtained the Hall angle as a function of temperature. Thus, we have established a method to study this complicated topic fully microscopically in a tractable manner.

References

- [1] T. Kita, Phys. Rev. B **64**, 054503 (2001).
- [2] T. Kita, Phys. Rev. B **79**, 024521 (2009).
- [3] E. Arahata and Y. Kato, J. Low. Temp. Phys. **175**, 346 (2014).
- [4] H. Ueki, W. Kohno, and T. Kita, J. Phys. Soc. Jpn. **85**, 064702 (2016).
- [5] T. Kita, J. Phys. Soc. Jpn. **73**, 21 (2004).

Computer-aided synthesis of zeolites

Tatsuya Okubo

*Department of Chemical System Engineering, The University of Tokyo
7-3-1 Hongo, Bunkyo-ku, Tokyo 113-8656*

Zeolites, a class of crystalline microporous materials composed of T (Si, Al, B, Ga, and others) and O, have been widely used as sorbents and catalysts due to their uniform pore sizes, catalytic activities, and hydrothermal stability. We have utilized the computational resources to describe zeolites and organic structure-directing agents (OSDAs) incorporated in their structures during the synthesis of zeolites. OSDAs are generally bulky and water-soluble organic molecules that interact with negatively charged inorganic species. OSDAs can guide the crystallization of specific zeolite framework since their molecular structures tailor the void spaces having particular sizes and structures. We have developed a scheme to design OSDAs that can fit the cavities in zeolite framework utilizing the combination of molecular modeling and meta-heuristic algorithms. Our first example of this approach designed unconventional OSDAs. With the use of this OSDAs, we synthesized highly nanoporous silica with very rare pore diameter (c.a. 2 nm) as silica and high porosity[1]. This method was useful not only for the synthesis of novel materials but also for the interpretation of experimental results at molecular level. We found that an OSDA possessing carbon chain with particular length crystallizes hierarchically and sequentially intergrown zeolite[2]. The molecular modeling revealed that this unique morphology is likely to be derived from the unusual interaction between the OSDA and zeolite framework[3].

Our computational investigations involved DFT calculation on Quantum ESPRESSO and

CP2K, and classical lattice minimization using a program named GULP[4]. We compiled Quantum ESPRESSO and CP2K to efficiently utilize all cores implemented in the system. On the other hand, the computations using GULP generally entail many jobs executed serially, which are inefficient if they are submitted one-by-one. In order to maximize the efficiency of the calculation, we have tried to use GXP[5], Rake, and the other tools to distribute serial jobs over many cores. The approach was successful to efficiently utilize all computational resources given on a batch job by allocating cores to jobs dynamically.

References

- [1] K. Muraoka, W. Chaikittisilp, Y. Yanaba, T. Yoshikawa, T. Okubo, *Chemical Communications*, 2015, 51, 10718.
- [2] W. Chaikittisilp, Y. Suzuki, R. R. Mukti, T. Suzuki, K. Sugita, K. Itabashi, A. Shimojima, T. Okubo, *Angewandte Chemie International Edition*, 2013, 52 (12), 3355.
- [3] S. H. Keoh, W. Chaikittisilp, K. Muraoka, R. R. Mukti, A. Shimojima, P. Kumar, M. Tsapatsis, T. Okubo, *Chemistry of Materials*, 2016, 28, 8997.
- [4] J. D. Gale, *Journal of the Chemical Society, Faraday Transactions*, 1997, 93(4), 629.
- [5] K. Taura, et al. *Future Generation Computer Systems*, 2013, 29(2), 662.

Local structure and phase transition in supercooled cyclohexane

Tomoko MIZUGUCHI¹, Soichi TATSUMI², and Susumu FUJIWARA²

¹*Institute for the Promotion of University Strategy, Kyoto Institute of Technology,
Matsugasaki, Sakyo-ku, Kyoto 606-8585*

²*Faculty of Materials Science and Engineering, Kyoto Institute of Technology,
Matsugasaki, Sakyo-ku, Kyoto 606-8585*

A recent experimental result revealed that a first-order phase transition occurs at 154 K in supercooled cyclohexane confined in silica nanopores [1]. This transition is different from that observed in a bulk system in which the liquid-plastic phase transition occurs at 280 K and the plastic-crystal phase transition occurs at 186 K. It is thus suggested to be a liquid-liquid phase transition. To understand the nature of this transition, we carried out all-atom molecular dynamics simulations of supercooled cyclohexane on the ISSP supercomputer system. In this year, we examined the local structures of bulk cyclohexane [2].

All the simulations were conducted with NAMD 2.10 [3] in the isothermal-isobaric (*NPT*) ensemble at 1 atm and various temperatures. The electrostatic interaction was handled by the smooth particle-mesh Ewald method. The CHARMM force field developed by Vorobyov *et al.* [4] was adopted for cyclohexane. Periodic boundary conditions were applied to the unit cell which contains 1331 cyclohexane molecules.

We first prepared liquid cyclohexane at 320 K, and quenched the system to 60 K with a cooling rate of 10^{11} K/s. The system remained liquid below its melting temperature due to such fast cooling. In experiments, a confined system is used to prevent crystallization. In our simulations, however, a supercooled state

can be attained even in a bulk system, thus we examined the local structures of bulk in this work. The system was then heated with a heating rate of 10^{11} K/s, and configurations were collected in the heating process. Starting from the dumped configurations, we carried out 1-ns equilibration runs and subsequent 1-ns production runs at a variety of temperatures.

The local structures are analyzed in terms of Voronoi polyhedra by using a Voropp library [5]. We use the Voronoi index $\langle n_3, n_4, n_5, n_6 \rangle$ to identify the type of each polyhedron, where n_i is the number of faces with i vertices. The $\langle 0, 1, 10, 2 \rangle$ type of polyhedra is the most populous at 90 K (glass) and its fraction decreases from 16.5% at 90 K to 4.2% at 290 K (liquid). It is an icosahedron-like cluster and frequently observed in metallic glasses. The full icosahedra $\langle 0, 0, 12, 0 \rangle$ are also observed, but the fraction is smaller than that of $\langle 0, 1, 10, 2 \rangle$. A distorted icosahedron is preferred as a local structure in the glassy state rather than a full icosahedron. This observation is consistent with the studies of metallic glasses.

We plot the fractions of four types of Voronoi polyhedra against temperatures in Figure 1. It clearly shows that the icosahedral structures $\langle 0, 1, 10, 2 \rangle$ and $\langle 0, 0, 12, 0 \rangle$ grow in a supercooled liquid, on the other hand,

crystalline(fcc)-like structures $\langle 0, 3, 6, 4 \rangle$ and $\langle 0, 3, 6, 5 \rangle$ do not grow when temperature decreases. The fraction of $\langle 0, 1, 10, 2 \rangle$ steadily increases with decreasing temperatures, but abruptly stops growing at 170 K. This fact implies that some structural change related to the icosahedral order occurs at this temperature. We cannot conclude clearly that the system is in a supercooled liquid state at this temperature. This issue will be addressed in our future work including a relationship with the liquid-liquid phase transition.

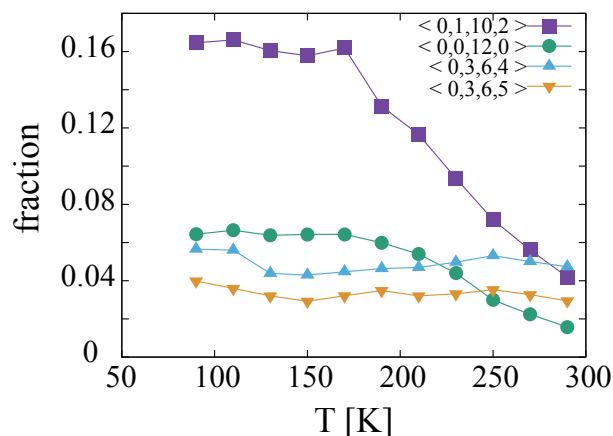


Figure 1: Fractions of four types of Voronoi polyhedra as a function of temperature: distorted icosahedra $\langle 0, 1, 10, 2 \rangle$, full icosahedra $\langle 0, 0, 12, 0 \rangle$, and fcc-like structures $\langle 0, 3, 6, 4 \rangle$ and $\langle 0, 3, 6, 5 \rangle$.

References

- [1] S. Tatsumi, T. Uehara, and M. Oguni: *Netsu Sokutei* **42** (2015) 142.
- [2] T. Mizuguchi, S. Tatsumi, and S. Fujiwara: *Proceedings of JSST 2016 - International Conference on Simulation Technology* (2016) 41.
- [3] J. C. Phillips, R. Braun, W. Wang, J. Gumbart, E. Tajkhorshid, E. Villa, C. Chipot, R. D. Skeeo, L. Kalé, K. Schul-ten: *J. Comput. Chem.* **26** (2005) 1781.
- [4] I. Vorobyov, V. M. Anisimov, S. Greene, R. M. Venable, A. Moser, R. W. Pastor, A. D. MacKerell, Jr.: *J. Chem. Theory Comput.* **3** (2007) 1120.
- [5] C. H. Rycroft: *Chaos* **19** (2009) 041111.

Magnetic excitation and spin transport in frustrated quantum spin chain

Hiroaki ONISHI

*Advanced Science Research Center, Japan Atomic Energy Agency,
Tokai, Ibaraki 319-1195*

The spin nematic state is currently attracting much attention as a novel quantum state. We have studied spin excitation spectra of the spin nematic state in a spin- $\frac{1}{2}$ J_1 - J_2 chain with $J_1 < 0$ and $J_2 > 0$ in a magnetic field [1]. Here, we investigate excitation spectra in the quadrupole channel.

To clarify the properties of the spin nematic state from the dynamical aspect, we analyze the dynamical quadrupole structure factor at zero temperature, given by

$$Q^{--}(q, \omega) = -\text{Im} \frac{1}{\pi} \langle 0 | Q_q^{--\dagger} \frac{1}{\omega + E_0 - H + i\eta} Q_q^{--} | 0 \rangle,$$

where Q_q^{--} is the Fourier transform of $Q_i^{--} = S_i^- S_{i+1}^-$, by exploiting the dynamical DMRG [2]. Note that we calculate the spectral weight at q and ω after one DMRG run with fixed q and ω , so that we need to perform many runs to obtain a full spectrum in a wide range of the q - ω space. The computations are accelerated by parallel simulations utilizing the system B of the ISSP supercomputer.

In Fig. 1, we show results of $Q^{--}(q, \omega)$ in the spin nematic regime. We find a dispersive mode. We clearly observe gapless excitations with high intensity at $q = \pi$ regardless of the value of magnetization, signaling quasi-long-range antiferro-quadrupole correlations. This indicates that a magnon pair is excited with zero energy, so that bound magnons would contribute to transport. To clarify transport properties, calculations of spin and thermal

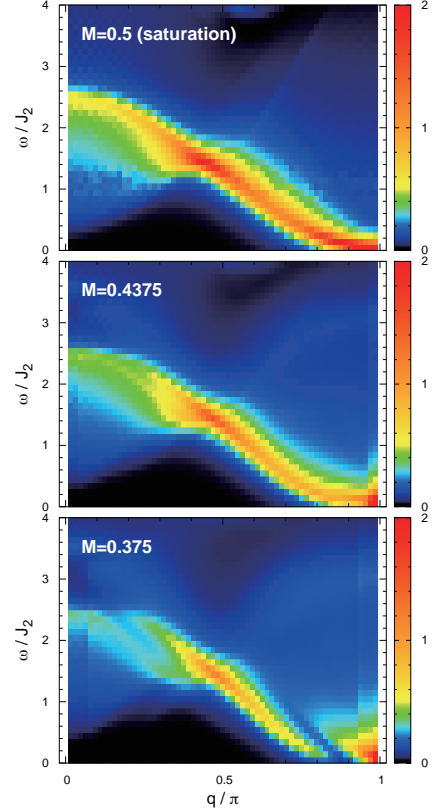


Figure 1: $Q^{--}(q, \omega)$ at several values of magnetization for $J_1 = -1$ and $J_2 = 1$.

conductivities by exact diagonalization are on going.

References

- [1] H. Onishi, J. Phys. Soc. Jpn. **84**, 083702 (2015); J. Phys.: Conf. Ser. **592**, 012109 (2015).
- [2] E. Jeckelmann, Phys. Rev. B **66**, 045114 (2002).

Large-scale simulations of semiconductor nanocrystals

Takamichi TERAO

*Department of Electrical, Electronic and Computer Engineering,
Gifu University, Yanagido 1-1, Gifu 501-1193*

Recently, glassy dynamics in interacting electron systems with geometrical frustration have attracted much attention. It has been pointed out that these frustrated electron systems may show a non-equilibrium relaxation behavior similar to that found in Coulomb glass systems where both many-body electron–electron interactions and randomness of the system are present. The relaxational dynamics of the Coulomb glass model were investigated, and a transition from stationary to non-stationary dynamics at the equilibrium glass transition temperature of the system was observed. At low temperatures, the system exhibits glassy dynamics, and the two-time autocorrelation function shows aging owing to the lack of time translation invariance. Despite these studies, the behavior of electronic systems with geometrical frustration is still not fully understood.

In this study, the hopping electron model on the Kagome lattice was investigated by Monte Carlo simulations. The spatial configuration of electrons on the Kagome lattice when the total energy of the system at a low temperature has been investigated. Because it is difficult to determine the exact ground state by examination of the many possible low-lying states, we employed annealing techniques to obtain an approximate solution. Figure 1 shows a typical snapshot of the electron configuration on the Kagome lattice [1]. Starting with a sufficiently high temperature, the system is cooled gradually until the temperature of the system reaches a sufficiently low target

temperature. Filled circles and open circles denote the sites occupied by an electron and vacant sites, respectively. The dashed rectangles in the figure are only for visual aid and denote blocks of occupied neighboring sites that comprise rod-like domains with different orientations.

The dynamics of the electrons in this model were also studied. For this purpose, the mean-square displacement (MSD) of the electrons on the Kagome lattice has been calculated with different temperatures. At a lower temperature, the MSD show deviations from diffusive behavior.

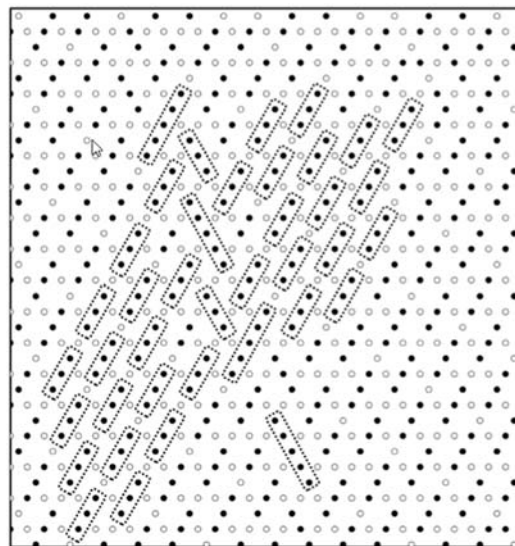


Fig. 1: Snapshot of electrons on Kagome lattice

References

- [1] T. Terao: *Eur. Phys. J. B* **89** (2016) 209.

Calculation of the optical properties of ordered structures of soft materials

Jun-ichi FUKUDA

*Department of Physics, Kyushu University, Motoooka 744, Nishi-ku, Fukuoka 819-0395
(formerly at AIST, 1-1-1 Higashi, Tsukuba 305-8565)*

My main focus in this project was the optical properties of exotic ordered structures exhibited by one of the intensively studied soft materials, a chiral liquid crystal. Particular focus is on the structures found when the liquid crystal is confined between two parallel substrates. I showed previously [1] that a highly chiral liquid crystal under such circumstances exhibit various types of defect structures depending on temperature and the spacing between the substrates. These structures include a hexagonal lattice of half-Skyrmions, and its typical lattice spacing is a few hundred nanometers.

My interest was how these structures can be observed by optical measures. This study was motivated by my experimental collaborators trying to observe such structures of a chiral liquid crystal by conventional optical microscope with high numerical aperture. As the typical periodicity of the structures, a few hundred nanometers, is close to the resolution limit of optical means, experimental observations are highly challenging. So is theoretical interpretation of optical images to be obtained by experiments, because geometrical

optics commonly used to explain the principles of optical microscopy is entirely useless. One has to solve the full Maxwell equations for propagating light, and careful consideration is necessary as to under what kind of setup the Maxwell equations must be solved.

It requires a huge amount of numerical resources to calculate the whole optical system using the finite difference time domain (FDTD) method routinely employed for the calculations of optical properties of such structures. Therefore, I carried out calculations of the responses of the system for different wavevectors of incident light, and tried to obtain optical images by combining the results of different calculations. My calculations relied on plane-wave expansions along the directions parallel to the surfaces of the confining substrates, and finite-difference discretization along the normal direction. The latter is carefully formulated so that the energy conservation (that is, the reflectivity and the transmittivity sum up to 1) is rigorously fulfilled up to rounding errors. To reduce the computational cost of solving a large set of linear equations obtained by the discretization

of the Maxwell equations, I made use of the tridiagonal nature of the matrix, which is realized by the finite-difference discretization. The structure of the liquid crystal was determined numerically by minimizing its free energy in terms of a second-rank orientational order parameter [1], and the profile of the dielectric tensor of the liquid crystal appearing in the Maxwell equations is assumed to be a linear function of the orientational order parameter.

The calculated microscope images for a Skyrmion lattice agree almost perfectly with

the experimental ones, and I believe that my numerical attempts successfully corroborate the experimental findings. Unfortunately, these results have not yet been published, and therefore I cannot describe the details in this report that will be open to public. Hopefully I will be able to present the details next time.

References

- [1] J. Fukuda and S. Žumer, *Nature Commun.* **2**, 246 (2011); *Phys. Rev. Lett.* **106**, 097801 (2011); *Phys. Rev. Lett.* **104**, 017801 (2010).

Light transport for medical imaging

Manabu Machida

*Institute for Medical Photonics Research, Hamamatsu University School of Medicine
1-20-1 Handayama, Higashi-ku, Hamamatsu, Shizuoka 431-3192*

We have studied light propagation in random media and sought its application to medical imaging, i.e., optical tomography. The specific intensity of near-infrared light in a random medium such as biological tissue is governed by the radiative transport equation, which is a linear Boltzmann equation. The equation is a first-order differential equation involving an integral term and has six variables, i.e., time t , positions x, y, z , and angular variables θ, φ . Therefore, numerical calculation of the radiative transport equation for a human body requires massive parallel computer simulations. This year, we focused on preparing such parallel computation.

The radiative transport equation is given as follows.

$$\left\{ \begin{array}{l} \left(\frac{1}{c} \frac{\partial}{\partial t} + s \cdot \nabla + \mu_a + \mu_s \right) I(x, s, t) \\ \quad = \mu_s \int_{S^2} p(x, s, s') I(x, s', t) ds', \\ \quad x \in \Omega, \quad s \in S^2, \quad t \in (0, T), \\ I(x, s, t) = g(x, s, t), \\ \quad (x, s) \in \Gamma_-, \quad t \in (0, T), \\ I(x, s, 0) = a(x, s), \quad x \in \Omega, \quad s \in S^2, \end{array} \right.$$

where c is the speed of light in the medium and $\mu_a(x), \mu_s(x)$ are the absorption and scattering coefficients, respectively. Here, Γ_{\pm} is defined as

$$\Gamma_{\pm} = \left\{ (x, s) \in \partial\Omega \times S^2; \pm \nu \cdot s > 0 \right\},$$

where ν is the outer unit vector normal to $\partial\Omega$.

In the time-independent case for the slab geometry, we experimentally verified the use of the radiative transport equation in optical tomography [1]. That is, we calculate tomographic images from experimentally obtained

data by solving the inverse transport problem using the method of rotated reference frames.

Although the method of rotated reference frames assumes simple geometry such as the slab geometry, obviously the shape of a human body is more complicated. Hence we need to use fully numerical schemes such as finite difference, which are computationally time-consuming but more flexible. Moreover, the number of source-detector pairs that can be used at the clinical stage is usually very limited. To acquire enough information to make tomographic images, it is necessary to conduct time-dependent experiments with the incident beam a short pulse. The introduction of the time-dependence significantly increases the computation time. We began by implementing the time-dependent radiative transport equation for light traveling in a human neck by focusing on a two-dimensional plane in the human neck [2]. In this way, we could test our finite-difference numerical scheme in two-dimensional space. It is now the time to use the supercomputer to bring the calculation to three-dimensional space.

References

- [1] M. Machida, G. Y. Panasyuk, Z.-M. Wang, V. A. Markel, and J. C. Schotland: *J. Opt. Soc. Am. A* **33** (2016) 551.
- [2] H. Fujii, S. Okawa, K. Nadamoto, E. Okada, Y. Yamada, Y. Hoshi, and M. Watanabe: *J. Appl. Nonlin. Dynamics* **5** (2016) 117.

Study of numerical methods for quantum phenomena of anisotropic superconductors

Yasunari Tanuma

Graduate School of Engineering Science, Akita University, Akita 010-8502

The quantum effects of superconducting phenomena are a key issue in the field of condensed matter physics. While the BCS pairing state is robust against non-uniform systems, unconventional pairing states with other symmetries are rather fragile. The tunneling spectroscopy is an important experimental tool to identify unconventional superconductors. The formation of Andreev bound states (ABS) at the surface of superconductor is attributed to the anisotropy in the pairing states displaying a zero energy peak (ZEP) in the local density of states. In some cases, such bound states have a topological origin due to the bulk-edge correspondence. Therefore, the ZEP in the local density of states, strongly suggests unconventional pairing symmetries. [1]

Theoretically, the tunneling spectroscopy is formulated as the surface density of states of superconductors. The ZEP in high- T_c cuprate superconductors has been found in a number of paper. On the other hand, a splitting of ZEP due to a broken time reversal symmetry state (BTRSS) is reported in several groups. The origin is that an induced subdominant is -wave component near the surface of d -wave superconductor shifts the ABS from zero energy, and then the ZEP splits in two peaks. The BTRSS is sensitive to the atomic-scale surface roughness of the superconductor, and it is not easy to discriminate the subdominant is -wave or id' components from the tunneling spectroscopy. In this stage, it is unclear how the quantum effect of the spin-orbit interaction affects the BTRSS induced near the surface of d -wave su-

perconductors.

In this report, we present a self-consistent calculation of the pair potentials of d -wave superconductors based on the t - J model with the Rashba spin-orbit interaction. Moreover, we have been studied the surface density of states under the self-consistently determined pair potentials. As shown in Figure 1 our results is that the effect of spin-orbit interaction by changing a doping rate has the various shapes of tunneling spectra.

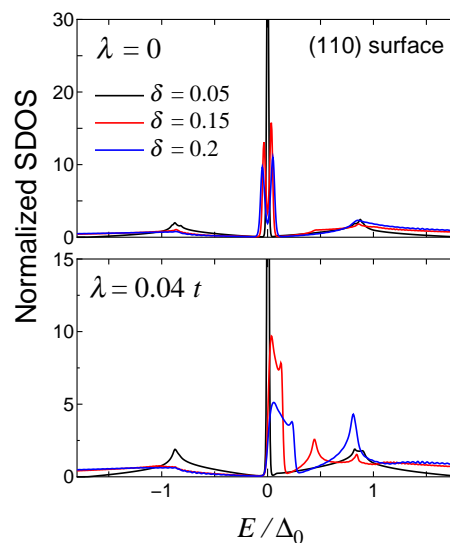


Figure 1: Normalized (110) surface density of states for $J/t = 0.4$. λ is the magnitude of Rashba spin-orbit interaction.

References

- [1] Y. Tanaka, M. Sato, and N. Nagaosa: J. Phys. Soc. Jpn. **81** (2012) 011013.

Effects of a magnetic field on spin-lattice-coupled orders in pyrochlore antiferromagnets

Kazushi AOYAMA

*Department of Earth and Space Science, Graduate School of Science, Osaka University
Machikaneyama-cho, Toyonaka-shi, Osaka 560-0043*

1 Introduction

An antiferromagnet on the pyrochlore lattice which is a three dimensional network of corner-sharing tetrahedra, is a typical example of frustrated magnets. It has been theoretically established that with the nearest-neighbor (NN) antiferromagnetic interaction alone, classical Heisenberg spins on the pyrochlore lattice do not order at any finite temperatures. On the other hand, the corresponding magnets ACr_2O_4 ($A=\text{Zn, Cd, Hg, Mg}$) where the magnetic ion Cr^{3+} with spin-3/2 forms the pyrochlore lattice, undergo a first order Neel transition together with a simultaneous structural transition, which suggests strong spin-lattice coupling (SLC) in this class of antiferromagnets. In this work, we theoretically investigate effects of the SLC originating from site phonons on the spin ordering in the antiferromagnetic classical Heisenberg model on the pyrochlore lattice by means of Monte Carlo (MC) simulations.

Last year, we showed that in the case without magnetic fields, the SLC induces a first-order transition into two different types of collinear magnetic ordered states. The state realized at stronger SLC is cubic symmetric characterized by the magnetic $(\frac{1}{2}, \frac{1}{2}, \frac{1}{2})$ Bragg peaks, while that at weaker SLC is tetragonal symmetric characterized by the $(1, 1, 0)$ ones, each accompanied by the commensurate local lattice distortions [1]. This year, we examined effects of a magnetic field on the spin-lattice-coupled orders.

2 Model and numerical method

The effective spin Hamiltonian in the site-phonon model has been derived elsewhere and is given by $\mathcal{H}_{\text{eff}} = \mathcal{H}_0 + \mathcal{H}_{\text{SL}}$,

$$\begin{aligned}\mathcal{H}_0 &= J \sum_{\langle i,j \rangle_s} \mathbf{S}_i \cdot \mathbf{S}_j - \sum_i \mathbf{H} \cdot \mathbf{S}_i, \\ \mathcal{H}_{\text{SL}} &= -Jb \sum_{\langle i,j \rangle} (\mathbf{S}_i \cdot \mathbf{S}_j)^2 \\ &\quad - \frac{Jb}{2} \sum_i \sum_{j \neq k \in N(i)} \mathbf{e}_{ij} \cdot \mathbf{e}_{ik} (\mathbf{S}_i \cdot \mathbf{S}_j)(\mathbf{S}_i \cdot \mathbf{S}_k),\end{aligned}$$

where J is the antiferromagnetic exchange interaction between NN spins, the dimensionless parameter b measures the strength of the SLC, and \mathbf{e}_{ij} is a unit vector connecting NN sites i and j . In \mathcal{H}_{SL} , the first term favors collinear spin state and the second term includes effective further neighbor interactions. \mathbf{H} denotes a magnetic field.

In our MC simulation, we perform 10^6 Metropolis sweeps under periodic boundary conditions at each temperature, where the first half is discarded for thermalization. Our single spin flip at each site consists of the conventional local update and a successive over-relaxation process in which we try to rotate a spin by the angle π around the local mean field. Observations are done in every 5 MC steps and the statistical average is taken over 8 – 10 independent runs. Since the cubic unit cell includes 16 sites, a total number of spins N is $N = 16L^3$ for a system size L . In the present

model, we have three parameters, the strength of the SLC b , the temperature T/J , and the magnetic field H/J . A systematic numerical investigation in this parameter space has been done using the facilities of the Supercomputer Center, ISSP, the University of Tokyo.

3 Result and Discussion

As is naively expected, in-field properties of the system depend on the zero-field ordering patterns. Figure 1 shows the results for $b = 0.2$ in the weaker SLC regime. As one can see in Fig. 1 (a), there are three regions classified by the field dependence of the magnetization whose low-temperature behavior is shown in Fig. 1 (b). In the region I, the canted $(1, 1, 0)$ -state is realized and the magnetization linearly increases as a function of the magnetic field. The region II corresponds to the 1/2-plateau region in which each tetrahedron takes three-up and one-down collinear spin configuration. The MC snapshot taken at a low temperature in the region II is shown in Fig. 1 (c). The $\uparrow\uparrow\downarrow$ chains run along all the six tetrahedral bonds, and this spin state is cubic-symmetric. As the magnetic field is further increased, spins start canting. The onset of this canted state in higher magnetic fields is denoted by the boundary between the regions II and III. All the transitions from the paramagnetic phase to the magnetic ones I, II, and III, are of first order.

From neutron diffraction experiments, it has been known that the zero-field ordered states in most of the spinel chromium oxides basically involve the $(1, 1, 0)$ magnetic patterns as observed in the weak SLC regime in the present model. Furthermore, the cubic-symmetric collinear spin configuration observed in the region II is the same as the experimentally proposed spin structure in the 1/2-plateau region of ACr_2O_4 ($A=\text{Cd}, \text{Hg}$). These results suggest that the SLC originating from the site phonons may be relevant to the magnetic ordering in these materials.

Finally, we would like to briefly comment on in-field properties in the stronger SLC regime. As in the case of the weaker SLC, we found the 1/2-plateau in the magnetization curve, but the spin ordering at higher fields are complicated, and this matter needs further detailed investigation.

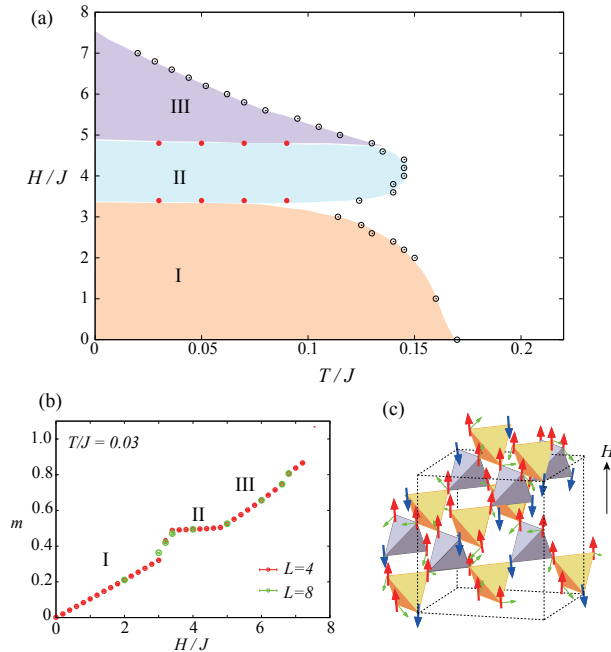


Figure 1: (a) The T - H phase diagram for $b = 0.2$ in the weaker SLC region, and (b) the corresponding magnetization curve at $T/J = 0.03$. (c) Real space spin configurations in the 1/2-plateau region [the region II in (a) and (b)], where a box represents the cubic unit cell.

References

- [1] K. Aoyama and H. Kawamura, Phys. Rev. Lett. **116**, 257201 (2016).

Competition between ferroelectric and antiferroelectric order in anisotropic molecular systems

Kyohei Takae and Hajime Tanaka

*Institute of Industrial Science, University of Tokyo
4-6-1 Komaba, Meguro-ku, Tokyo 153-8505, Japan*

Mesoscopic and glassy dynamics in dielectric materials are of growing interests among soft matter physicists because some complex phenomena in dielectrics such as relaxor behaviour can be understood by the concept of soft matter physics, namely, hierarchical spatio-temporal cooperativity. Here, two or more cooperating/competing phase ordering produces rich physical phenomena. Particularly, we focus our attention on the coupling between polarisation and strain in dielectric materials, and aim to understand their complex behaviour by constructing a simple model exhibiting such mesoscopic dynamics and related phase transitions.

We construct a molecular model exhibiting relaxor-like behaviour and antiferroelectricity. The pair interaction consists of dipolar interaction and Lennard-Jones interaction but slightly modified to realise anisotropic molecular systems. Note that our model corresponds to Stockmayer model if molecular anisotropy vanishes, which is known to exhibit paraelectric–ferroelectric phase transition in crystalline phase. We perform molecular dynamics simulation to study how ferroelectric and antiferroelectric order can be controlled by changing material composition and molecular anisotropy.

Firstly, by introducing non-polar particles as impurities, we examine how ferroelectric order is disturbed by them [1]. By increasing the impurity concentration, we found the de-

struction of global ferroelectric order. Nevertheless, mesoscopic ferroelectric order still emerge in regions surrounded by the impurities. This result implies the appearance of polar nanoregion is determined by the distribution of impurities in our model. Large polarisation and strain response to external electric field is also observed due to the collective response of mesoscopically ordered regions, indicating a strong polarisation-strain coupling.

Secondly, we vary molecular anisotropy and examine how antiferroelectric order is stabilised [2]. We determine the phase diagram by comparing the chemical potential of liquid phase, paraelectric crystalline phase, ferroelectric crystalline phase, and antiferroelectric crystalline phase. The chemical potential of the liquid phase is calculated by the Widom particle insertion methods, and that of crystals is obtained by Einstein crystal method. We found the antiferroelectric phase is stabilised for large anisotropy, which results from the coupling between polarisation and strain in our system. The phase transition also induce large lattice deformation, implying the possibility to control polarisation order by external strain.

References

- [1] K. Takae and A. Onuki: *J. Phys.: Condens. Matter* **29** (2017) 165401.
- [2] K. Takae and H. Tanaka, in preparation.

Nonequilibrium phase transition in the large scale dense hard sphere molecular dynamics simulation

Masaharu ISOBE

Nagoya Institute of Technology

Gokiso-cho, Showa-ku, Nagoya, 466-8555

The hard disk/sphere systems have been investigated as one of the simplest molecular models in the field of both equilibrium and non-equilibrium statistical physics. In this project, we investigated non-equilibrium phase transition in the hard disk/sphere model system with modern algorithms, especially for Event-Chain Monte Carlo (ECMC) [1] and Event-Driven Molecular Dynamics (EDMD) [2], where we propose the “Hybrid Scheme”, namely, ECMC for equilibration and EDMD for calculation of dynamical properties [3, 4].

Facilitation in athermal molecular systems — Efficient algorithm figures out a mystery in supercompressed glassy materials—: One of the grand challenges of statistical physics is to understand whether the essential properties of glass forming materials is fundamentally thermodynamic or dynamic in origin. A perspective that favors a dynamic origin is called Dynamic Facilitation (DF) theory [5, 6, 7]. The concept of “facilitation” is used in general to indicate the ability to activate people in a meeting to exchange ideas and information with a common purpose in business and education. The “facilitation” is also observed in the microscopic molecular systems. DF theory was known to explain a wide range of empirically observed dynamical features of thermal supercooled liquids and glasses. In our present paper, the results of an international collaboration on three continents (Japan, U.S. and U.K.) devoted to investigating the applicability of DF theory to athermal systems,

i.e., systems of hard particles where the relevant control parameter is pressure rather than temperature, under “supercompressed” conditions. By employing novel efficient algorithms [1, 2, 3], it was possible to find true equilibrium states and generate the phase diagram of a binary mixture of hard spheres. This allowed to study in detail the equilibrium dynamics of high density systems, showing that slow relaxation at these conditions are consistent with the predictions of DF theory generalized to systems controlled by pressure rather than temperature. In such athermal molecular systems under “super-compressed” conditions — where what is facilitated is the ability of the constituent particles to structurally relax — giving rise to correlated and cooperative dynamics, in a manner predicted by theory [8]. These results should pave the way for understanding thermal and athermal glassy materials from a unified point of view.

References

- [1] E. P. Bernard, W. Krauth, and D. B. Wilson: Phys. Rev. E **80** (2009) 056704.
- [2] M. Isobe: Int. J. Mod. Phys. C **10** (1999) 1281.
- [3] M. Isobe: Mol. Sim. **42** (2016) 1317.
- [4] M. Isobe: “Advances in the Computational Sciences — Proceedings of the Symposium in Honor of Dr Berni Alder’s

90th Birthday”, edited by Eric Shweger, Brenda M. Rubenstein, and Stephen B. Libby, World Scientific, **Chapter 6** (2017) 83.

- [5] D. Chandler and J. P. Garrahan: *Annu. Rev. Phys. Chem.* **61** (2010) 191.
- [6] L. O. Hedges, R. L. Jack, J. P. Garrahan and D. Chandler: *Science* **323** (2009) 1309.
- [7] A. S. Keys, L. O. Hedges, J. P. Garrahan, S. C. Glotzer, and D. Chandler, *Phys. Rev. X*, **1** (2011) 021013.
- [8] M. Isobe, A. S. Keys, D. Chandler, and J. P. Garrahan: *Phys. Rev. Lett.* **117** (2016) 145701.

Evaluation of quantum error correction codes' performance against realistic error models

Takanori SUGIYAMA

Graduate School of Engineering Science, Osaka University

Machikaneyama-chou, Toyonaka, Osaka 560-8531

Summary: We have studied a quantum error correction code under realistic error models. We focused on a specific code called a 1D repetition code. We have performed Monte Carlo simulations for evaluating the fault-tolerance of the code against errors with quantum coherence. The numerical results clarified that quantum coherence in errors can weaken the fault-tolerance of 1D repetition code.

Coherence of a bare quantum system is easily broken by environmental noise, and the use of methods for protecting the coherence from the noise is inevitable for implementing large-scale quantum computer. A quantum error correction code (QECC) is one of such methods for protecting logical information of quantum systems (logical qubits), which consist of multiple quantum systems (physical qubits), from noise [1]. By increasing the number of physical qubits, a QECC can make the effect of noise on the logical qubit exponentially small if strength of the noise is less than a threshold.

There are a lot of proposals of QECCs, and currently a 2D planer surface code [2] is considered as a promising candidate [3, 4]. A 2D planer surface code arranges physical qubits in a checkerboard pattern on a 2D plane. As an intermediate step to the realization, experimental groups of UCSB/Google [5] and TU Delft [6] implemented a 1D component of the code, which is called a quantum 1D repetition code. An experimental group of IBM implemented a 2D component of the

code [7]. Although the numbers of physical qubits in these experiments are $O(1)$ and not enough for building large-scale quantum computer, the experimental results imply that an implementation of a quantum device using a 2D planer surface code with $O(100)$ physical qubits would be possible in the near future.

In order to check whether the device would work as desired under an effect of environmental noise, we need a theoretical method for evaluating the performance. There are two theoretical approaches to evaluate a performance of QECCs. The standard approach [8] assumes a depolarizing noise model. This approach makes it easier to analyze the performance, but the model assumed is not realistic. The other approach [9], which uses the diamond norm, does not assume specific noise models. However, this approach sacrifices the tightness of the evaluation and greatly underestimates the performance.

We proposed such a new theoretical method for evaluating QECCs' performance. Our method is applicable to both of classical and quantum noises and is tighter than the approach using the diamond norm. We applied our method to a quantum 1D repetition code, which is an important subcode of a 2D planer surface code, and we have numerically evaluated the performance against quantum noise.

We have applied the theoretical results to a classical memory with a quantum 1D repetition code, which does not tolerate an arbitrary noise but is still an important building

block of a 2D planer surface code, and hence has been implemented in recent experiments [5, 6]. We have performed Monte Carlo simulations for calculating the values of the upper bound for the following settings: The numbers of physical qubits, N , are from 5 (3 data-qubits and 2 ancilla-qubits) to 101 (51 data-qubits and 50 ancilla-qubits). The number of error detection cycles is $N - 1$. In order to analyze the effect of quantumness in noise, we considered a noise model that is a probabilistic mixture of a bit-flip noise model with error rate p and a unitary noise with a mixing probability c (the case of $c = 0$ corresponds to the pure bit-flip noise model). We have phenomenologically allocated the noise on each of the data-qubits and ancilla-qubits. We have chosen the minimum-weight perfect matching algorithm for the decoding and used the Blossom V matching library [10] for the numerical implementation. We performed 4×10^6 repetitions for the Monte Carlo sampling.

Our numerical results have clarified that the performances against quantum noise greatly differs from those against classical noise. In real experiments, c is not zero because there exist the energy relaxation and over/under-rotation during unitary operations on physical qubits. The standard approach is not applicable to realistic settings of experiments. We have provided a new theoretical tool, or a new classical simulator, applicable to QECC-equipped quantum devices with $O(100)$ physical qubits, which would appear in the near future, under realistic assumptions on noise.

Our results can contribute not only to the evaluation of the performance, but also to further improvement of quantum devices. For implementing large-scale quantum computer, it is required to suppress the noise as smaller than the threshold as possible, because we cannot obtain the advantage of the error decreasing via increasing N around the threshold. In order to suppress the noise, which are already tiny in current experiments, we need

an appropriate guideline for further improving the design of devices, chips, and pulses. The standard approach is not appropriate for the purpose, because the realistic noise is out of the scope as mentioned above. Our results would provide an appropriate guideline for the purpose, and the detailed analysis on specific physical systems such as superconducting circuits is an open problem to be tackled.

Acknowledgements: The computation in this work has been done using the facilities of the Supercomputer Center, the Institute for Solid State Physics, the University of Tokyo. This work was supported by JSPS Research Fellowships for Young Scientists (PD:H27-276) and the Grant-in-Aid for Young Scientists (B) (No.24700273).

References

- [1] D. A. Lidar and T. A. Brun (ed.), *Quantum Error Correction* (Cambridge University Press, 2013)
- [2] S. B. Bravyi and A. Y. Kitaev, arXiv:9811052 [quant-ph].
- [3] J. M. Martinis, npj Quantum Information **1**, 15005 (2015).
- [4] J. M. Gambetta, J. M. Chow, and M. Steffen, arXiv:1510.04375 [quant-ph].
- [5] J. Kelly et al., Nature **519**, 66 (2015).
- [6] D. Riste et al., Nature Commun. **6**, 6983 (2015).
- [7] A. D. Córcoles et al., Nature Commun. **6**, 6979 (2015).
- [8] E. Dennis et al., J. Math. Phys. **43**, 4452 (2002).
- [9] P. Aliferis, Chap. 5 in *Quantum Error Correction* (Cambridge University Press, 2013)
- [10] V. Kolmogorov, Math. Prog. Comp. **1**, 43 (2009)

Analysis of Topological Systems with Real Space Structures

Toshikaze KARIYADO

*International Center for Materials Nanoarchitectonics (MANA), NIMS
Namiki, Tsukuba, Ibaraki 305-0044*

This year, we have mainly focused on the electronic structure of antiperovskite Ba_3SnO . A_3EO (A=Ca,Sr,Ba and E=Sn,Pb) is predicted to be a topological crystalline insulator, but the first-principles calculation indicates the gap at the Fermi energy is tiny because of the cubic symmetry of the crystal [1]. More specifically, around the k-points of gap minima, the electronic state is described as Dirac fermions. For the stability of the possible topological crystalline insulator phase, it is better to have large gap. Then, in order to find out a way to have a larger topological gap in this series of materials, we investigate (i) the effect of the lattice distortion experimentally found [2], and (ii) possible heterostructures where the A sites are substituted layer-by-layer, both of which break the cubic symmetry, by means of the first-principles calculation.

For the first-principles calculation, we have employed the parallelized version of QuantumEspresso package [3]. In the calculations for the distortion effect, the number of atoms in a unit cell is still not so large, and then, the parallelization is really efficient by using the k-point parallelization. On the other hand, for the heterostructure calculation, especially when the period of layer-by-layer alternation is large, we rather divide each work for a k-point into pieces, and distribute them. This is rather different from the k-point parallelization, but anyway, enables us to calculate the electronic structure with relatively large real

space structures.

Figure 1 shows the band structure for Ba_3SnO with the distorted crystal structure. As is expected, the gap at the Dirac nodes becomes visible in this energy scale. (Originally, the Dirac nodes are exactly gapless, or have tiny gap of the order of meV.) However, the deviation of the crystal structure from the original cubic structure itself is not significant, the gap size is still small comparing with the typical energy scale of the band structure. The heterostructure induces the sizable gap depending on the position of the Dirac nodes in the Brillouin zone [4].

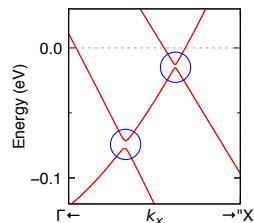


Figure 1: Band structure for Ba_3SnO with distorted structure.

References

- [1] T. Kariyado and M. Ogata: J. Phys. Soc. Jpn. **80** (2011) 083704; T. H. Hsieh, J. Liu, and L. Fu: Phys. Rev. B **90** (2014) 081112.
- [2] J. Nuss *et al.*: Acta Cryst. B **71** (2017) 300.
- [3] P. Giannozzi *et al.*: J. Phys.: Condens. Matter **21** (2009) 395502.
- [4] T. Kariyado, in preparation.

Electronic states of bioluminescence related molecules

Miyabi HIYAMA

*Institute for Solid State Physics, University of Tokyo
Kashiwa-no-ha, Kashiwa, Chiba 277-8581*

In firefly bioluminescence, the emission occurs due to the luciferin-luciferase reaction. Figure 1 shows the reaction process for firefly luciferin-luciferase reaction. In this process, the emitter, Oxyluciferin, is produced by the oxidation reaction of the substrate, Luciferin, via two intermediate molecules which are Luciferyl adenylate (Luciferyl-AMP) and 4-membered dioxetanone (Dioxetanone). According to the previous studies, we found that the protonated/deprotonated chemical species of Oxyluciferin and Luciferin present in aqueous solutions and that the ratio of these concentrations depends on the pH values of solution [1]-[2]. Thus, the molecular structures for intermediate molecules of the luciferin-luciferase reaction could also depend on the pH values of solutions.

In this year, we calculated the electronic potential energies and free energy profiles for Luciferin, Oxyluciferin, luciferyl-AMP, and Dioxetanone, and their deprotonated chemical species [3] to elucidate this emission process across the pH range of 7-9. All calculations were performed using the GAUSSIAN09 [4] program on system B of Super Computer Center in ISSP.

From these relative free energies, it was found that the oxidation pathway changes from Luciferin \rightarrow deprotonated Luciferyl-AMP \rightarrow deprotonated Dioxetanone \rightarrow Oxyluciferin to deprotonated Luciferin \rightarrow deprotonated Luciferyl-AMP \rightarrow Dioxetanone \rightarrow Oxyluciferin with increasing pH value. This indi-

cates that deprotonation on the hydroxy group of benzothiazole ring occurs during the formation of Dioxetanone at pH 7-8, whereas Luciferin in the reactant has a deprotonated hydroxy group form at pH 9.

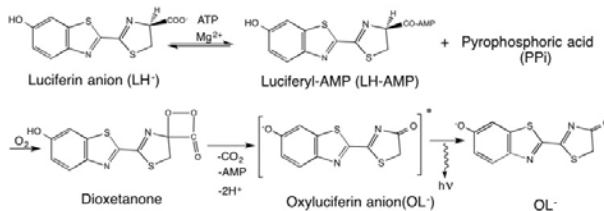


Figure 1: luciferin-luciferase reaction in firefly bioluminescence

References

- [1] Hiyama et al.: Photochem. Photobiol. **91** (2015) 819.; **91** (2015) 74.; **90** (2014) 820.; **90** (2014) 35.; **89**(2013) 571.; **88** (2012) 889.
- [2] Hiyama et al.: Chem. Phys. Lett. **577** (2013) 121.
- [3] M. Hiyama, H. Akiyama, and N. Koga : Luminescence: The Journal of Biological and Chemical Luminescence (2017) *in press*.
- [4] Gaussian 09, Revision D.01, M. J. Frisch et al.

Topological analysis of membrane systems using persistent homology

Fumiko Ogushi

AIMR, Tohoku Unive.

Katahira 2-1-1, Aoba-ku, Sendai, 980-8577

Biological membrane involves wide variety of lipid molecules and forms complicated structures with various concave-convex with large-scale changes in cell-cycle progressions, like membrane fusion, fission, and vesicular transportation, Golgi formations, and so on. In a cell, lipid molecules distribute heterogeneously affecting membranes structures. Moreover, compositions and distributions of lipids are not stationary. Flexibility of lipid redistribution is one of the most important phenomena to overcome the limitation of model membrane to real biological membrane.

This year, we investigated structural features of multi lipid membranes using persistent homology. The multi lipid membrane is made up with water molecules and two different types of lipid molecules, 20:4 PC (DAPC) and diacylglycerol (DAG), which have different Gaussian curvatures. Three structures of membranes, Lamella, Inverse Hexagonal, and Sponge-like structures, are examined by molecular dynamics simulation. Such a complex structures in three dimension are hard to distinguish. Thus, we use persistent homology to analyze membrane morphologies. Persistent homology is an algebraic tool for computing topological features of data. It can systematically characterize geometric objects and capture the topological properties such as rings and cavities, and provide the metrics of these topological properties. In recent years, persistent homology and its graphical representation, persistent diagram, can be computed effi-

ciently [1, 2, 3]. Some types of condensed systems are well distinguished its local structures using persistent homology and PDs [4, 5].

We calculated persistent homology for DAPC, DAG, and water molecules. Comparing with persistent diagrams of equilibrium structures, we succeeded to capture topological features of different membrane systems and localization of DAGs in Sponge-like membranes. Moreover, persistent diagrams show that DAGs in Sponge-like membrane do not form any characteristic formations.

References

- [1] Perseus [online] Available at www.math.rutgers.edu/vidit/perseus.html
- [2] PHAT [online] Available at <https://code.google.com/p/phat>
- [3] CGAL [online] Available at <https://cgal.org>
- [4] T. Nakamura, Y. Hiraoka, A. Hirata, E. G. Escolar, and Y. Nishiura, *Nanotechnology*, 26 (2015) 304001.
- [5] Y. Hiraoka, T. Nakamura, A. Hirata, E. G. Escolar, K. Matsue, and Y. Nishiura, *PNAS*, 113, 25, (2016) 7035

Numerical Study of One Dimensional Frustrated Quantum Spin Systems

Kazuo HIDA

*Division of Material Science, Graduate School of Science and Engineering
Saitama, Saitama 338-8570*

1 Ground-State Phase Diagram of $S = 1$ Diamond Chains[1]

The ground-state phase diagram of a spin-1 diamond chain is investigated. The Hamiltonian is given by,

$$\mathcal{H} = \sum_{l=1}^L \left[\mathbf{S}_l \tau_l^{(1)} + \mathbf{S}_l \tau_l^{(2)} + \tau_l^{(1)} \mathbf{S}_{l+1} + \tau_l^{(2)} \mathbf{S}_{l+1} + \lambda \tau_l^{(1)} \tau_l^{(2)} \right], \quad (1)$$

where \mathbf{S}_l and $\tau_l^{(\alpha)}$ ($\alpha = 1, 2$) are spin operators with magnitude 1. Owing to a series of conservation laws $\forall l [\mathbf{T}_l^2, \mathcal{H}] = 0$, where $\mathbf{T}_l = \tau_l^{(1)} + \tau_l^{(2)}$, any eigenstate of this system can be expressed using the eigenstates of finite odd-length chains or infinite chains with spins 1 and 2.

The ground state undergoes quantum phase transitions with varying λ as shown in Fig. 1. In addition to the various paramagnetic DC n phases, which consists of clusters with n consecutive nonvanishing T_l s, the Haldane phase and the ferrimagnetic phases with 1/3 and 1/6 of the saturated magnetization are found. Among them, the ferrimagnetic phase with 1/6 magnetization is accompanied by the spontaneous breakdown of translational symmetry. The ground state energy of the DC n phase is calculated by the Lanczos numerical diagonalization and finite-size DMRG methods. That of the DC ∞ phase is estimated by the iDMRG method.

Exact upper and lower bounds for the phase boundaries between these phases are also obtained.

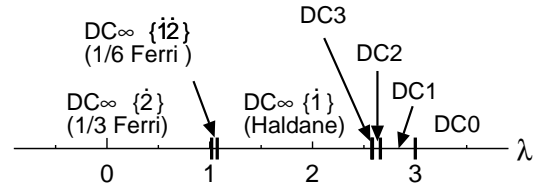


Figure 1: Ground state phase diagram of the $S = 1$ diamond chain..

(collaborator : Ken'ichi Takano)

2 Partial Ferrimagnetism in $S = 1/2$ Heisenberg Ladders with Ferromagnetic-Antiferromagnetic Legs and Antiferromagnetic Rungs[3]

The $S = 1/2$ Heisenberg ladders described by the Hamiltonian

$$\mathcal{H} = -J_1 \sum_{i=1}^L \mathbf{S}_{i,1} \cdot \mathbf{S}_{i+1,1} + J_2 \sum_{i=1}^L \mathbf{S}_{i,2} \cdot \mathbf{S}_{i+1,2} + R \sum_{i=1}^L \mathbf{S}_{i,1} \cdot \mathbf{S}_{i,2} \quad (2)$$

are investigated, where $\mathbf{S}_{i,a}$ is the spin-1/2 operator. For $J_1 = J_2$, the rung-dimer state is the exact ground state down to a finite critical value of R as shown by Tsukano and Takahashi[4]. We consider the case $-J_1 < 0$,

$J_2 > 0$ and $R > 0$ in general. The ground-state phase diagram is determined by the Lanczos numerical diagonalization method for $L = 12$ as shown in Fig.2. In the Lieb-Mattis ferrimagnetic phase, $M = L/2 = 6$. In the partial ferrimagnetic phase, $0 < M < L/2$. It is found that the partial ferrimagnetic phase extends over a wide parameter range.

The ground-state phase diagram is studied also analytically based on the mapping onto the nonlinear σ model[5] and the perturbation expansion from the strong-rung limit. The results support the overall phase diagram obtained numerically as shown in Fig. 2.

The finite-temperature susceptibility is also calculated by the canonical thermal pure quantum state method.[6] The χT^2 - $T^{1/2}$ plot in Fig. 3 suggests that the susceptibility behaves as $\chi \sim T^{-2}$ in the partial ferrimagnetic phase as well as in the Lieb-Mattis ferrimagnetic phase. This behavior is the same as that of the ferromagnetic Heisenberg chain studied by Takahashi and Yamada.[7]

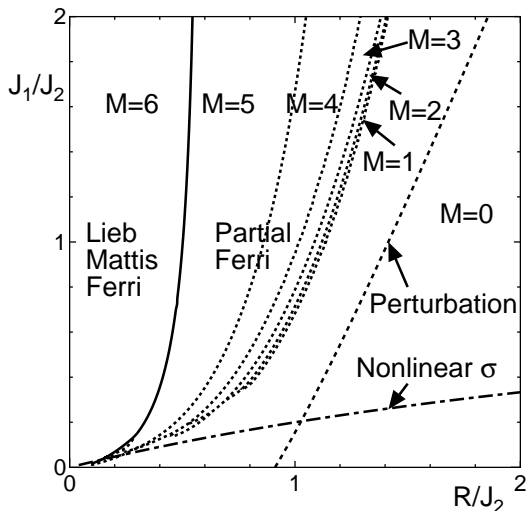


Figure 2: Ground state phase diagram of the $S = 1/2$ Heisenberg ladder (2) with $L = 12$. The spontaneous magnetization is denoted by M . The dashed and dash-dotted lines are the nonmagnetic-partial ferrimagnetic phase boundaries calculated by the perturbation expansion from the strong-rung limit and mapping onto the nonlinear σ model, respectively.

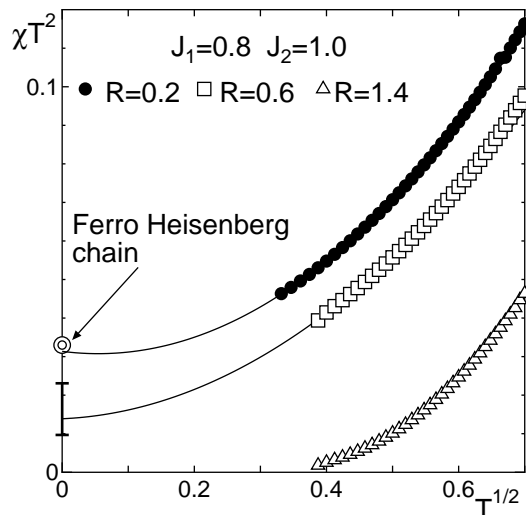


Figure 3: Plot of χT^2 against $T^{1/2}$. The size extrapolation is carried out by the Shanks transform from $L = 8, 10$ and 12 .

(collaborator: Kazutaka Sekiguchi)

This work is supported by JSPS KAKENHI Grant Numbers JP25400389 and JP26400411.

References

- [1] K. Hida and K. Takano, J. Phys. Soc. Jpn. **86**, 033707 (2017).
- [2] K. Takano, K. Kubo, and H. Sakamoto, J. Phys.: Condens. Matter **8**, 6405 (1996).
- [3] K. Sekiguchi, Master Thesis, Saitama University (2017) [in Japanese].
- [4] M. Tsukano and M. Takahashi, J. Phys. Soc. Jpn. **66**, 1153 (1996).
- [5] S. Furuya and T. Giamarchi, Phys. Rev. B. **89**, 205131 (2014)
- [6] S. Sugiura and A. Shimizu, Phys. Rev. Lett. **111**, 010401 (2013)
- [7] M. Takahashi and M. Yamada, J. Phys. Soc. Jpn. **54**, 2802 (1985).